

# KOBELCO TECHNOLOGY REVIEW

No. **33** Feb. 2015

**Feature- I : Natural Resources and Energy**

**Feature- II : MONODZUKURI (Art of Design and Manufacturing)**

## Contents

### Feature- I Natural Resources and Energy

Resources Trend and Use of Direct Reduced Iron in Steelmaking Process ..... 1  
Dr. Hidetoshi TANAKA

Beneficiation Plants and Pelletizing Plants for Utilizing Low Grade Iron Ore ..... 8  
Tsutomu NOMURA, Norihito YAMAMOTO, Takeshi FUJII, Yuta TAKIGUCHI

Application of Coke Oven Gas to MIDREX® Process ..... 16  
Noriaki MIZUTANI, Takashi KISHIMOTO, Norihide MAEDA

Evaluation of Spontaneous Combustion in Stockpile of Sub-bituminous Coal ..... 21  
Dr. Haeyang PAK, Toshiya TADA, Naoki KIKUCHI, Takuo SHIGEHISA, Toru HIGUCHI, Dr. Seiichi YAMAMOTO

Mine-mouth Power Generation System Based on Upgraded Brown Coal (UBC®) ..... 28  
Takeo KASHIWAGI, Hiromichi ISHINO, Takashi TAKAGI, Ken HIROSE

Energy Saving Air-Separation Plant Based on Exergy Analysis ..... 34  
Masaaki TANIGUCHI, Hitoshi ASAOKA, Toshiyuki AYUHARA

Fabrication and Properties of Forged Rings made of Modified 9Cr-1Mo-V Steel  
for High-temperature and High-pressure Reactor ..... 39  
Tomoya SHINOZAKI, Tetsuya KOMURA, Nobuyuki FUJITSUNA, Hiroki NAKASHIMA, Masato YAMADA, Tomoaki NAKANISHI

### Feature- II MONODZUKURI (Art of Design and Manufacturing)

Technologies for Process Design of Titanium Alloy Forging for Aircraft Parts ..... 44  
Takashi CHODA, Dr. Hideto OYAMA, Shogo MURAKAMI

Efficient Inspection for Gas Pipes by Infrared Thermography ..... 50  
Hideki ENDO, Takuya KUSAKA

Machining Technology for Large Impellers of Centrifugal Compressors ..... 56  
Toru KAINO

Automatic Welding System for Crawler Crane Top and Bottom Booms ..... 61  
Akira OKAMOTO, Masatoshi HIDA, Tsutomu OONE, Takemasa YAMASAKI, Tatsuro ASANO, Toshifumi KOBAYASHI

Global e-learning System for Technical Support Engineers ..... 70  
Youichirou Sou, Masashi YAMAKOSHI, Yoshihiro MURAKAMI

Evaluation System for Thin-Film Oxide Semiconductor Using  $\mu$ -PCD  
- Effectivity of Measuring Technique - ..... 74  
Yuki NONOMURA, Keizo YAMASHITA, Futoshi OJIMA, Dr. Tomoya KISHI, Kazumasa TOKUDA, Dr. Toshihiro KUGIMIYA

Editor-in-chief :  
Yasuaki SUGIZAKI

Associate Editors :  
Tomokazu NAKAGAWA

Editorial Committee :  
Tadashi AIURA  
Nobuyuki FUJITSUNA  
Tsunehiro FUKUNAKA  
Kenichi INOUE  
Yasushi MAEDA  
Tsuyoshi MIMURA  
Norihito NAKAJIMA  
Hiroyuki SHIMIZU  
Syoji YOSHIMURA

Published by

**Secretariat & Publicity Dept.**  
**Kobe Steel, Ltd.**

2-4, Wakinohama-Kaigandori 2-chome,  
Chuo-ku, Kobe, HYOGO 651-8585,  
JAPAN  
<http://www.kobelco.co.jp>

Editorial Office: **Shinko Research**  
**Co., Ltd.**

5-5, Takatsukadai 1-chome,  
Nishi-ku, Kobe, HYOGO 651-2271, JAPAN  
Fax: +81-78-992-9790  
E-mail: [rd-office@kobelco.com](mailto:rd-office@kobelco.com)

© Kobe Steel, Ltd. 2015

# Resources Trend and Use of Direct Reduced Iron in Steelmaking Process

Dr. Hidetoshi TANAKA \*1

\*1 Technology & process Engineering Dept., Iron Unit Div., Engineering Business

Expectations are rising for new ironmaking processes that can utilize a wide variety of materials and fuels and also are environmentally friendly. The direct reduction (DR) process is one such ironmaking process that can substitute for blast-furnace (BF) ironmaking. This new process can utilize inexpensive shale gas, which enables its plants to be built at various locations. The DR process may be adapted for coal-based processing, which will contribute to the stable supply of direct reduced iron (DRI). This paper outlines the DR technologies developed by Kobe Steel and includes a survey on the contribution of DRI as a substitute for scrap used in electric arc furnaces (EAFs) and as a burden material in BFs.

## Introduction

It was believed that the blast furnace (BF) ironmaking process would continue to predominate for some time in the future. However, the process seems to be reaching a turning point due to various problems: e.g., i) the soaring prices of iron ore and coking coal, resulting from the rapid growth of crude steel production in China, ii) the service life issues of coke ovens, and iii) environmental issues such as CO<sub>2</sub> reduction.

On the other hand, shale gas has grabbed much attention. In the U.S., it is not only influencing energy security, but affecting a number of industries, including iron and steel.

This paper focuses on steelmaking processes that utilize direct reduced iron (hereinafter referred to as "DRI"), taking up the aspects of environmental protection and resource depletion. It reviews the present status of the direct reduction (hereinafter referred to as "DR") technology at Kobe Steel and examines the role played by DRI in achieving a paradigm shift in the iron and steel industry.

## 1. Resources trend surrounding iron and steel industry

As shown in Fig. 1, world crude steel production exceeded 1.5 billion tonnes in 2011 owing to the increasing production of crude steel in China, and this value is steadily increasing.<sup>1)</sup> Almost 70% of the crude steel was produced by blast furnace / basic oxygen furnace (BF/BOF) process.

In the meantime, as shown in Fig. 2, the world steel stock exceeded 23 billion tonnes as a result

of the crude steel production in the past and, accordingly, the amount of scrap generated is increasing steadily year by year.<sup>2)</sup> In other words, a so-called "urban mine" has emerged, providing the source of iron for, and promoting the use of, electric-arc-furnace (EAF) processes.

This rapid increase in crude steel production has also resulted in significant increases, as shown in Fig. 3, in the prices of iron ore and coking coal, the principal raw materials of iron and steel.<sup>3)</sup> There are some background factors: e.g., i) the current BF process relies heavily on high-grade ore mined in Brazil and Australia and on special coking coal with small reserves, and ii) several suppliers of the raw

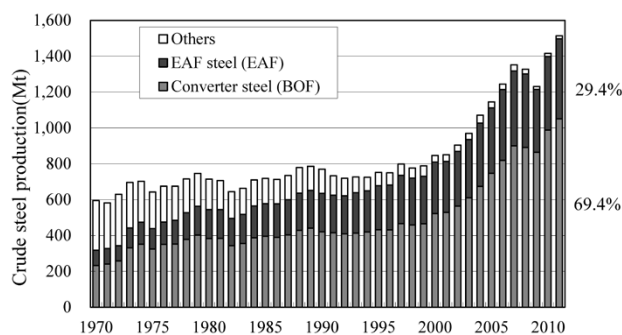


Fig. 1 Changes in world crude steel production<sup>1)</sup>

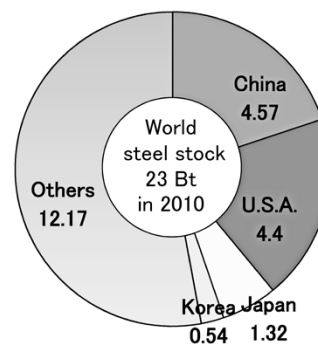


Fig. 2 World steel stock in 2010<sup>2)</sup>

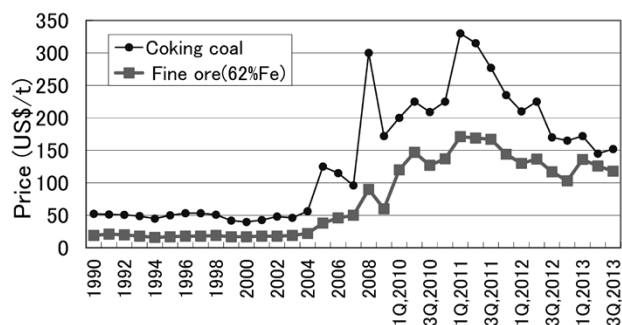


Fig. 3 Price changes in iron ore and coking coal<sup>3)</sup>

materials have merged and become oligopolistic.

On the other hand, thanks to the beginning of commercial production of shale gas in North America, the price of natural gas dropped from 11.5 \$/mmBTU in 2008 to 3.7 \$/mmBTU in 2012.<sup>4)</sup> Accordingly, the price of electricity for industrial use is expected to see a further decrease from its 2011 price of 7 ¢ /kwh.

## 2. Status of world DRI production

Direct reduction is a process for reducing iron ore in the solid state. It requires much less capital investment than the BF process and requires no coke. Therefore, DR plants have been built mainly in oil and natural gas producing countries to supply raw iron for EAF processes. Particularly in the Middle East, where only a limited amount of scrap is generated, DRI is used as the principal raw material to produce steel in EAFs.

Fig. 4 shows the transition of world DRI production. The DRI production has increased by a factor of almost 100, from approximately 0.8 million tonnes in the 1970s to approximately 74 million tonnes in 2012. Currently, DRI accounts for 16% of the raw material charged into EAFs. Recently, the demand for DRI has also been increasing in developed countries, and the amount of DRI carried by sea reached 14.7 million tonnes in 2012.<sup>5)</sup>

Table 1<sup>6)</sup> summarizes the typical characteristics of DRI. DRI has many pores left after the oxygen is removed by reduction reaction and can easily be

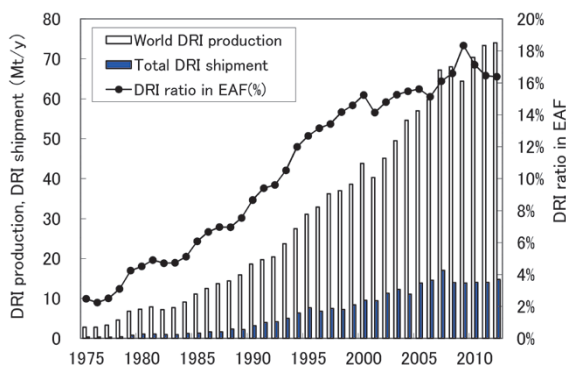


Fig. 4 Changes in world DRI production and DRI shipments by year<sup>5)</sup>

Table1 Characteristics of DRI and HBI<sup>6)</sup>

	DRI	HBI
T.Fe(%)	90~94	←
M.Fe(%)	83~89	←
Metallization(%)	92~95	←
Carbon(%)	1.0~3.5	←
Gangue (%)	2.8~6.0	←
Bulk Density(t/m <sup>3</sup> )	1.6~1.9	←
Apparent Density(t/m <sup>3</sup> )	3.4~3.6	5.0~5.6

re-oxidized. Therefore, DRI has a risk of generating heat and igniting, making its maritime transport difficult. For this reason, DRI was originally consumed solely within ironworks. It was against this background that production technology was developed for hot briquetted iron (hereinafter referred to as "HBI"); the technology involves the hot compacting of DRI to increase its apparent density and thus prevent re-oxidation. This technology has facilitated marine transport and enabled the raw iron to be supplied to the global market.

The change in the production volume of HBI by processes is shown in Fig. 5.<sup>7)</sup> Approximately 80% of HBI is currently produced by the MIDREX<sup>®</sup> note 1) process. As will be described later, the MIDREX process, thanks to its unique reductant gas composition, can discharge DRI at a higher temperature than the HYL process, which mainly relies on hydrogen reduction. Thus the MIDREX process is more suitable for producing HBI.

DR processes roughly fall into two classes depending on the reductant used: namely, natural gas based and coal based. Fig. 6<sup>5)</sup> shows the world production volume of DRI in 2012 and the ratio of DRI produced by each process. The MIDREX process and HYL process, both using natural gas as the reductant, account for approximately 75% of the total production. The remainder is produced by other processes using coal. Midrex Technologies,

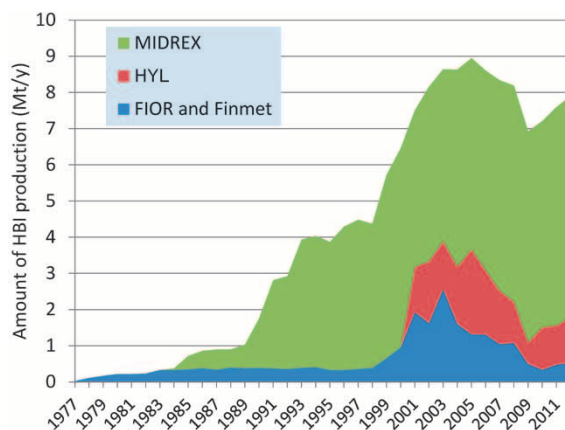


Fig. 5 Yearly HBI production by process<sup>7)</sup>

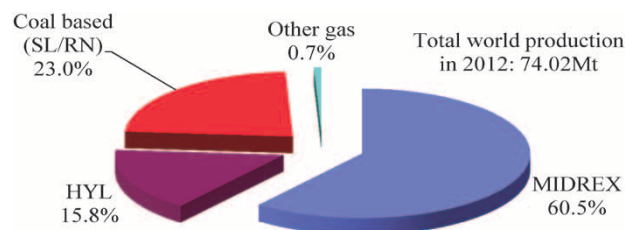


Fig. 6 World DRI production processes in 2012<sup>5)</sup>

note 1) "MIDREX" is a registered trademark of Kobe Steel.

Inc., the leading company in DR processing, is a wholly-owned subsidiary of Kobe Steel.

### 3. Direct Reduction Technology

#### 3.1 Kobe Steel's natural-gas-based DR process

Fig. 7 depicts the flow of the MIDREX process.<sup>8)</sup> Either pellets or ore lumps are charged into a shaft furnace from the furnace top, reduced inside the furnace and discharged from the bottom as DRI. Conventionally, the DRI was discharged after cooling; however, it is now being discharged hot and then transferred to the steelmaking process downstream so as to improve the energy consumption rate and productivity of the EAFs.

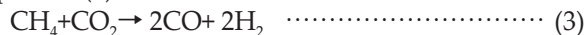
The reduction reaction of the iron oxide occurring inside the shaft furnace is expressed by (1) and (2):



Equation (1) represents the reduction reaction by hydrogen and is highly endothermic, while Equation (2) represents the reduction reaction by CO gas and, conversely, is exothermic. Thus the temperature distribution in the furnace varies depending on the ratio of the reduction reactions (1) and (2) occurring in it. It should be noted that the DR process that uses natural gas as reductant exploits the contribution of hydrogen to the reduction, as expressed by Equation (1), and is reported to emit significantly less CO<sub>2</sub> compared with the BF process with coal reductant.<sup>8)</sup>

The main feature of the MIDREX process lies in

the composition of its reductant gas. In this process, the CO<sub>2</sub> in the exhaust gas of the reduction reaction, emitted from the furnace top, is effectively utilized as a reforming agent of natural gas, as expressed by Equation (3).



As a result, the concentration ratio of H<sub>2</sub>/CO in the reductant gas becomes 1.5, which is much richer in CO gas than that of the HYL process with H<sub>2</sub>/CO of 3 to 5. This distinguishes the MIDREX process from others by its feature of easily being able to maintain a higher temperature inside the furnace.

The MIDREX plants have been operated mainly in oil producing regions with abundant natural gas. There were 63 plants in operation as of 2012.<sup>5)</sup> Fig. 8 shows the rated production capacities of the MIDREX plants built so far. Currently, work is in progress to develop the SUPER MEGAMOD, a further scale-up of the shaft furnace with a projected

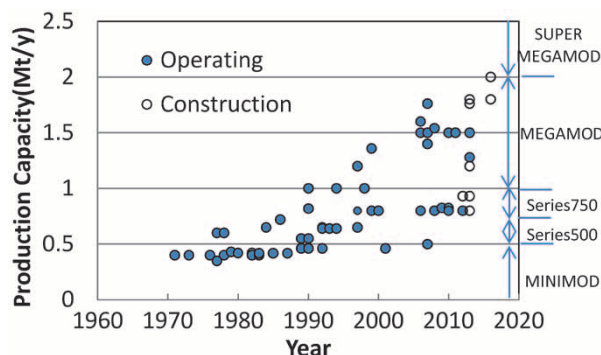


Fig. 8 Rated capacities of MIDREX plant by year

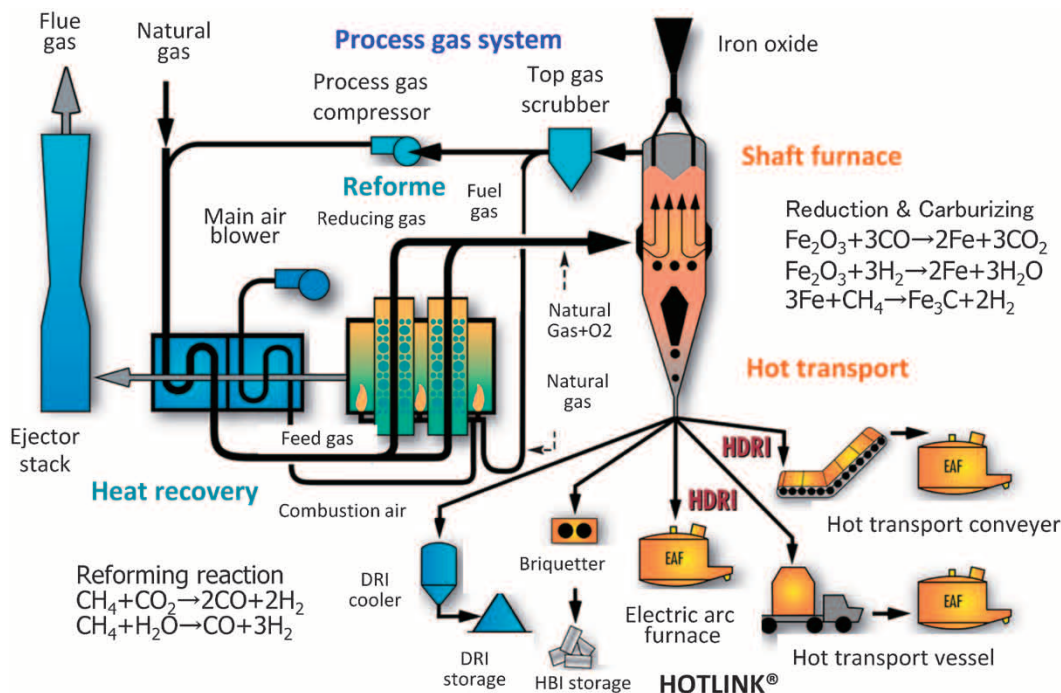


Fig. 7 MIDREX process flow sheet<sup>8)</sup>



capacity of 2 million tonnes per year. A DR plant with 2 million tonne capacity, is to be launched in Texas in the U.S. in 2016. The plant capacities are becoming larger year by year.<sup>9)</sup>

**Fig. 9** compares the processes in their 2011 capacities and production volumes.<sup>10)</sup> As is evident from this chart, the MIDREX process has achieved a production volume that is close to its capacity, which indicates that it has a more stable operation than other processes. This is one of the reasons for its world share of 60%.

The MIDREX process used to be operated at limited locations. To alleviate this restriction, attempts have been made to diversify fuels as shown in **Table 2**.<sup>11)</sup> This includes the use of reductants such as the off-gas from the COREX process and synthesis gas produced by a coal gasifier. In particular, a DR plant with a capacity of 1.8 million t/y is gathering attention. The order for this plant was placed by Jindal Steel & Power Limited, an Indian steel manufacturer, at the end of 2009. This plant is worthy of attention because it utilizes synthesis gas produced by a coal gasifier as its reductant and enables the use of Indian coal with high ash content for the production of DRI.

Coke oven gas (hereinafter "COG") can also be used for the production of DRI, since it contains chemical energy in the form of highly concentrated H<sub>2</sub> and CH<sub>4</sub>. A new partial-oxidation system as shown in **Fig.10** may be introduced to convert COG into synthesis gas suitable for the MIDREX process and to produce DRI in a shaft furnace. The DRI thus produced can be used in BFs and in BOFs, which

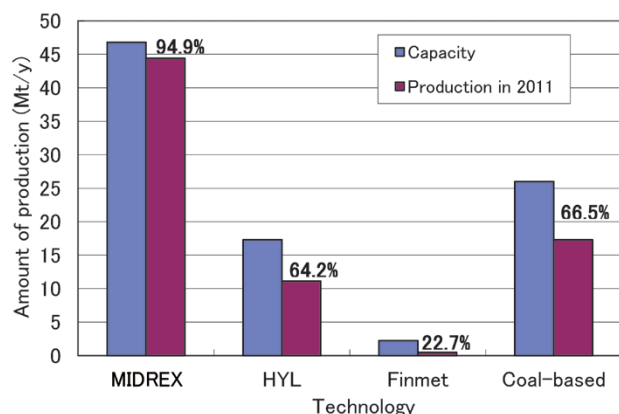


**Fig. 9** World DRI capacity and production per technology in 2011<sup>10)</sup>

**Table 2** MIDREX process energy source flexibility<sup>11)</sup>

Energy source	Reducing gas H <sub>2</sub> /CO	MIDREX plant reference	Start-up
COREX/MIDREX plant	0.3-0.4	Arcelor Mittal South	1999
COREX offgas	0.5-0.6	JSW Projects Limited	Construction
MIDREX NG Plant	1.5-1.7	Numerous (60 modules operation)	Since 1969
MXCOL Plant	2.0	JSPL Angul	Construction

not only reduces CO<sub>2</sub> emissions, but also increases productivity by 30%, according to a report.<sup>12)</sup>

### 3.2 Kobe Steel's Coal-based DR process

The rotary kiln process has been used for a long time as a DR process based on coal. This process, however, has the disadvantages of being relatively small in scale, suffering from long downtime due to the formation of kiln rings, and consuming a large amount of coal. This has limited the plant locations, to India, for example.<sup>13)</sup>

As another DR process using coal, the reduction of carbon composite agglomerates began to attract attention in the 1990s. It was found that, when iron oxide and carbon are closely placed in agglomerates, the reduction reaction occurs at lower temperatures and at higher rates.<sup>14)</sup> These carbon composite agglomerates, however, are fragile. To compensate for the reduction in physical strength, a new process, FASTMET<sup>®</sup> (note 2), was developed; it involves a rotary hearth furnace (hereinafter "RHF") that allows the reduction reaction to occur statically. This process is promising as a DR process allowing the use of inexpensive coal, and it is being put to practical use to treat steel mill dust, as shown in **Table 3**.<sup>15)</sup>

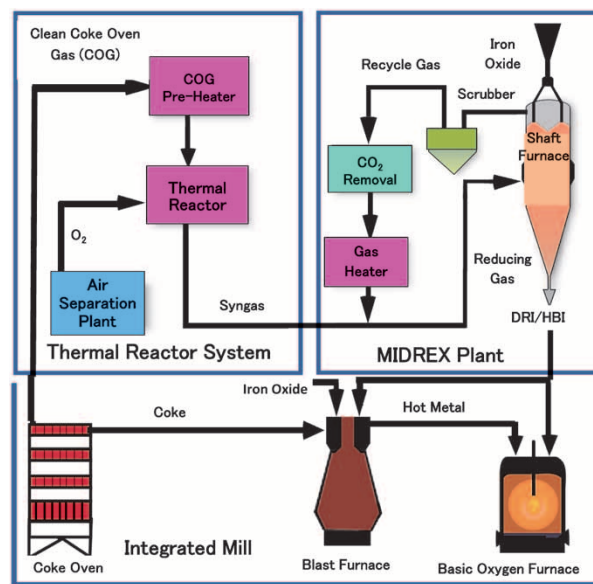


**Fig.10** Using COG for MIDREX process<sup>12)</sup>

**Table 3** FASTMET commercial plants<sup>15)</sup>

Company	Location	Dust (t/y)	Start up
NSSMC	Hirohata No.1	190,000	April. 2000
	Hirohata No.2	190,000	Feb. 2005
	Hirohata No.3	190,000	Dec. 2008
	Hirohata No.4	220,000	Oct. 2011
JFE	Nishinohon	190,000	Apr. 2009
KSL	Kakogawa	14,000	April 2001

note 2) "FASTMET" is a registered trademark of Kobe Steel.

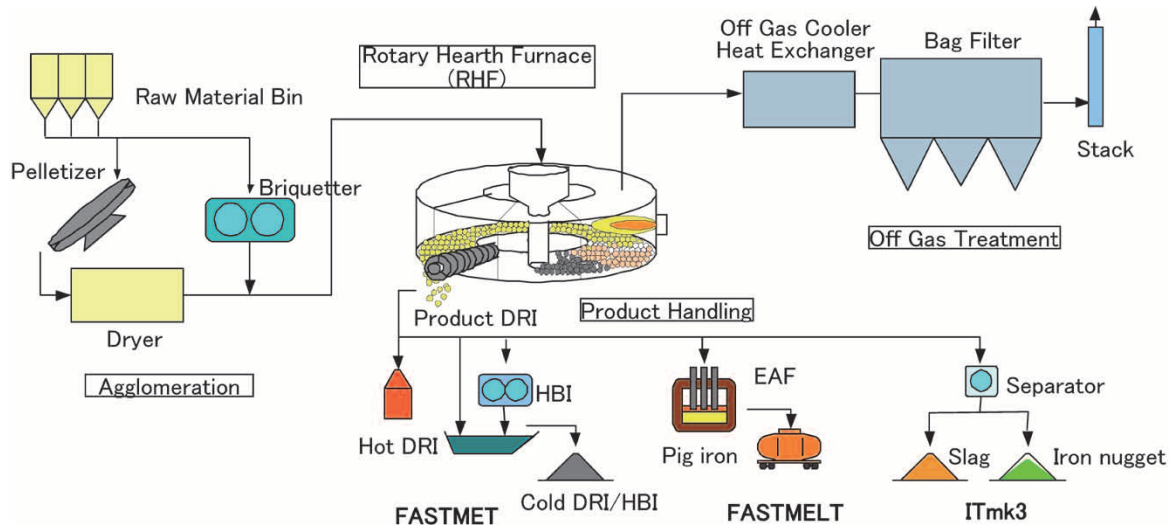


Fig.11 Flow sheet of Kobe's coal-based direct reduction process

This technology has led to the development of a next-generation ironmaking process, ITmk3<sup>®</sup> (note 3) ([ai ti:] mark three). This process is attractive, since it can produce iron nuggets, the equivalent of pig iron, in one step in a rotary hearth furnace. A first commercial plant with an annual capacity of 500 thousand tonnes was inaugurated in Minnesota, U.S., in January 2010.<sup>16)</sup> Fig.11 depicts the flow of Kobe Steel's coal-based DR process using an RHF.

#### 4. Future perspective

##### 4.1 Expansion of ironmaking process using iron scrap

Fig.12 combines and shows the forecasted world steel demand and the forecasted scrap generation.<sup>17), 18)</sup> These forecasts are made on the basis of construction, civil engineering and transportation, the sectors that account for 70% of the total amount. The gap between these two forecasts (black column) indicates the insufficient quantity of iron, which cannot be compensated for

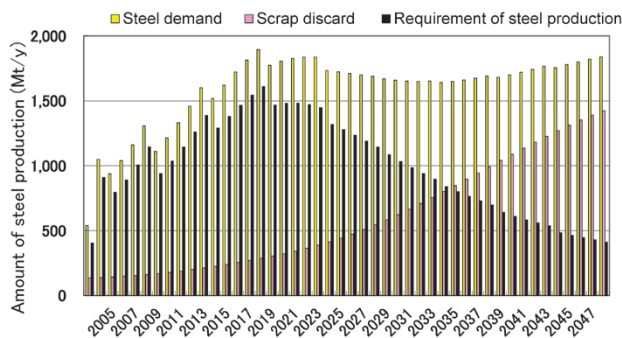


Fig.12 Necessary amount of steel production forecasted from steel demand and scrap discard<sup>19)</sup>

note 3) "ITmk3" is a registered trademark of Kobe Steel.

by scrap alone. In order to fill this gap, iron must be newly made from iron ore. As for the future, this deficiency of iron is forecasted to increase, reaching 1.6 billion tonnes around 2020, and to decrease thereafter<sup>19)</sup>. This is a forecast and the actual time may vary, but it will happen sooner or later. In other words, the increasing scrap generation implies that ironmaking processes using iron scrap as their principal raw material will possibly play an important role.

Scrap iron usually contains tramp elements such as Cu and Sn. An increase in their content adversely affects the processing quality in the downstream processes including continuous casting and rolling. This is the reason why EAFs, using scrap as their principal raw material, have been applied primarily to steel grades for construction with relaxed quality requirements. These tramp elements are difficult to remove by treating hot metal and/or molten steel. Thus, in order to control their content, clean scrap must be selected for the raw material, or the scrap must be diluted by clean raw iron such as DRI or pig iron. In the U.S., clean raw iron is added in the amount of 65 to 70% to dilute the scrap melted in EAFs. This process can even produce high-grade steel that compares with the steel produced by BOFs.<sup>20)</sup> Another advantage is that the carbon in the clean raw iron resolves the issue of nitrogen, a problem intrinsic to EAFs.<sup>21)</sup>

Fig.13 shows the energy consumption and CO<sub>2</sub> emissions of EAF processes that use scrap and DRI. Comparison was made with the BF/BOF process.<sup>8)</sup> The energy consumption and CO<sub>2</sub> emissions become minimal when 100% scrap is used, which reduces CO<sub>2</sub> emission to a quarter. If scrap and DRI are combined, a common practice in the US, a significant CO<sub>2</sub> reduction is expected in comparison with the BF/BOF process because natural gas is used to

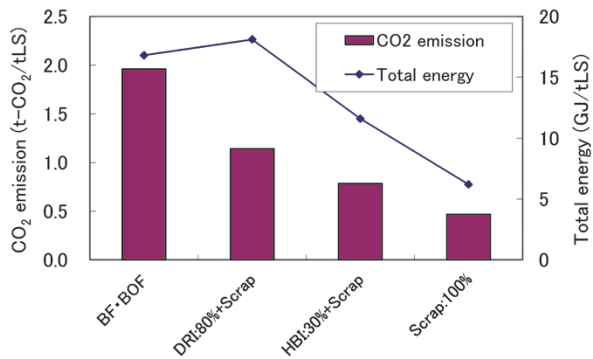


Fig.13 Energy consumption and carbon emissions for steelmaking routes <sup>8)</sup>

produce the DRI charged.

In the US, the volume of crude steel produced by EAFs has been exceeding that produced by the BF/BOF process since 2002. There, EAF integrated mini-mills are prevailing. These EAF integrated mini-mills use scrap and DRI as a source for their iron and produce thin sheets. In 2011, approximately 60% of the crude steel was produced by the EAF process.<sup>1)</sup> Therefore, a stable supply of DRI for diluting degraded scrap is important for the sustainable growth of EAF processes in the future.

#### 4.2 Expansion of DRI production in North America

Recently, the gas-based DR process has been scaled up (to greater than 2 million t/y/unit). In North America, where the emergence of shale gas has made electric power and natural gas readily available at lower cost, a number of projects are being actively pursued to implement upstream ironmaking based on this process (Table 4).<sup>22)</sup> The reason for the introduction of the process is said to be that, when compared with the BF process of

Table 4 Status of gas-based DRI projects in North America <sup>22)</sup>

Company	Location	Capacity (kt)	Status	Start-up
Nucor	Louisiana	2,500	Confirmed	2013
Nucor	Louisiana	2,500	Permitted- not approved	2015+
Voestalpine	Texas	2,000	Confirmed- needs permitting	2016
Bluescope	Ohio	1,000	Under consideration	2016+
Essar Steel	Minnesota	2,500	Permitted- not approved	2016+
Severstal NA	Mississippi & Trinidad	n/a	1.5 tpy project rejected	
US Steel	Minnesota	n/a	Under consideration	2016+
<b>Total</b>		<b>10,500</b>		

the same scale, the DR process emits 1/3 amount of carbon and the DRI facilities require only half the investment.<sup>23)</sup>

As described above, as a result of increased scrap generation and the reduced price for natural gas in the U.S., the DR process is being revisited as an ironmaking process with less environmental burden. The amount of DRI production in North America is expected to grow sharply in the future.

#### 4.3 Use of DRI as energy container

The past records indicate that charging DRI into a BF is expected to bring about positive effects such as increased production, a decreased reductant ratio, a decrease in agglomerates and reduction of CO<sub>2</sub>.<sup>24)</sup> A laboratory study has shown that the upper limit of DRI that can be charged into a BF may be as high as 100%.<sup>25)</sup> In actual operation at the AK Steel Corporation, the amount of DRI recorded as charged into their BF reached a monthly average of 227 kg/t<sup>26)</sup>, indicating that up to approximately 20% can be charged without causing any problem.

Fig.14 compares the current ironmaking with future small-scale, independent on-site ironmaking. This independent on-site ironmaking offers a new business model in which the energy of the reduction reaction, which accounts for three-fourths of the

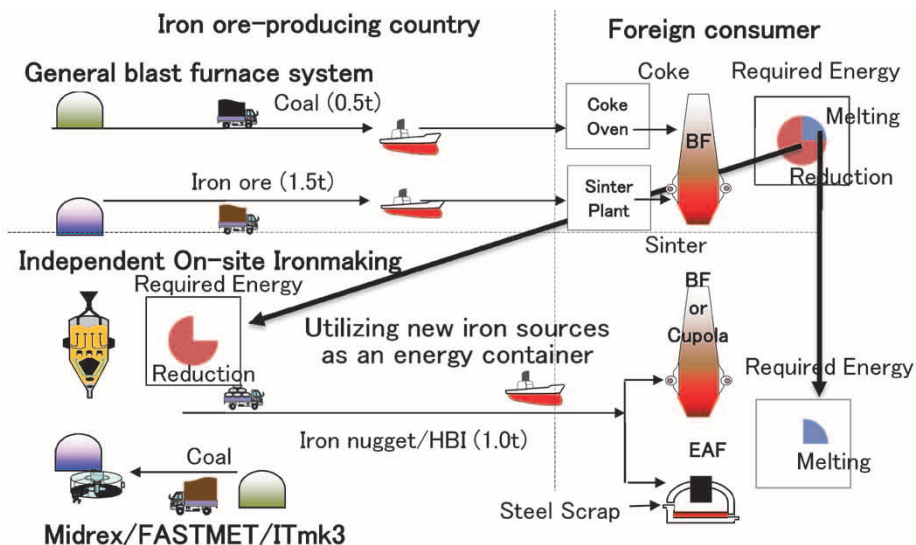


Fig.14 General blast furnace system and future independent on-site ironmaking model



energy used for ironmaking, is shifted to a third country to exploit DRI as an energy container, while halving the transported amount of the raw materials required for ironmaking. One example is the MIDREX plant with 2 million t/y capacity that a European company, voestalpine AG, announced to build in Texas, U.S.<sup>9)</sup> In this project, iron ore pellets produced in Brazil will be transferred to Texas to be reduced by inexpensive shale gas, and the product HBI will be shipped to Austria to be used by ironworks there. This project thus will reduce CO<sub>2</sub> emissions. Kobe Steel's MIDREX process, which can produce HBI with ease, is more advantageous in exploiting DRI as an energy container.

There are future concerns including CO<sub>2</sub> reduction, the service life of coke ovens, the environmental issues of sintering plants and the elasticity of BF production. Against this background, the use of inexpensively produced DRI in integrated ironworks may be promoted further, depending on the price trends of iron ore and coking coal governing the cost of pig iron made by BFs.

## Conclusions

The U.S. iron and steel industry, the precursor of the Japanese iron and steel industry, passed the period of its maturity in the 1950s and saw the decline of BFs in the 2000s. In place of these BFs, Nucor-type mini-mills using scrap have emerged. Equipped with state-of-the-art technologies including the continuous casting of thin slabs, they are continuing their highly efficient production on a small scale. As evident from the history of the iron and steel industry in the U.S., the time is approaching when the industry will rely on scrap as its raw iron, which will be generated in large quantities.

On the other hand, the lower price of natural gas resulting from the commercial production of shale gas in North America is promoting the gas-based DR process. In addition, the development of the coal-based DR process that exploits the ubiquitous energy of coal has relaxed the restrictions on the locations of DR plants, which, in the past, could be built only in natural gas producing countries. This is expected to facilitate a stable supply of clean raw iron.

On the other hand, the lower price of natural gas resulting from the commercial production of shale gas in North America is promoting the gas-based DR process. In addition, the development of a coal-based DR process that exploits the ubiquitous energy of coal has relaxed the restrictions on the locations of DR plants, which, in the past, could be built only in natural gas producing countries. This

is expected to facilitate a stable supply of clean raw iron. As a result, DRI can be combined with scrap, adding versatility in the production of high-grade steel by EAFs, and can also be used for BF etc. as an energy container, an effective way of suppressing CO<sub>2</sub> emissions. Kobe Steel will strive to contribute to problem solving in the iron and steel industry through its own DR process.

## References

- 1) World Steel Association. Steel Statistical Yearbook 2012.
- 2) Steel Recycling Research Corporation. Research Report No.16. June 21, 2012, p.2.
- 3) The Tex Report No.10995. December 4, 2012, p.8.
- 4) R. L. Hunter. Scrap Supplements and Alternative ironmaking VI. Oct. 28-30, 2012.
- 5) MIDREX Technology Inc. 2012 WORLD DIRECT REDUCTION STATISTICS.
- 6) M. ATSUSHI et al. Kobe Steel Engineering Reports. 2010, Vol.60, No.1, p.5.
- 7) H. P. Gaines et al. Direct form Midrex 2013. 2nd. Quarter, p.7.
- 8) J. Kopfle et al. Millenium Steel 2007, p.19.
- 9) Japan metal daily. March 19, 2013.
- 10) MIDREX Technology Inc. 2011 WORLD DIRECT REDUCTION STATISTICS.
- 11) H. P. Gaines. Direct Form Midrex 2012, 2nd. Quarter, p.10.
- 12) S. C. Montague. Steel Success Strategies XXVII. New York. June 18, 2012.
- 13) H. Tanaka. 196th and 197th Nishiyama Memorial Technical Lecture. September 2008, p.163.
- 14) Y. Kashiwaya et al. ISIJ Inter. 2006. Vol.46, No.11, p.1610.
- 15) H. Tanaka. 205th and 206th Nishiyama Memorial Technical Lecture. June 2011, p.111.
- 16) S. KIKUCHI et al. Kobe Steel Engineering Reports. 2010, Vol.60, No.1, p.9.
- 17) H. Hatayama et al. Environ. Sci. Technol. 2010, Vol.44, No.16, p.6457.
- 18) H. Hatayama et al. CAMP-ISIJ 2010. Vol.23, p.615.
- 19) T. Harada et al. METEC InSteelCon ECIC 2011, Session 10.
- 20) Metal Bulletin Monday 6 Feb. 2012, p.20.
- 21) R. Lule et al. Direct form Midrex 2009, 3rd/4th. Quarter. p.3.
- 22) B. Levich. World DRI and Pellet Congress 2013. p.101.
- 23) The Tex Report No.10545. February 1, 2011, p.8.
- 24) H. Tanaka et al. TETSU-TO-HAGANE. 2006, Vol.92, No.12, p.330.
- 25) Y. Ujisawa et al. CAMP-ISIJ. 2009, Vol.22, p.282.
- 26) Iron and Steel Maker. Aug. 2001.

---

Note) The names of companies and products cited herein may be trademarks or the registered trademarks of their respective owners.



# Beneficiation Plants and Pelletizing Plants for Utilizing Low Grade Iron Ore

Tsutomu NOMURA \*1, Norihito YAMAMOTO \*2, Takeshi FUJII \*2, Yuta TAKIGUCHI \*3

\*1 Technology & Process Engineering Dept., Iron Unit Div., Engineering Business

\*2 Plant Engineering Dept., Iron Unit Div., Engineering Business

\*3 Ironmaking Dept., Kakogawa Works, Iron & Steel Business

*Recently, the grade of iron ore deposits has deteriorated and further development of low grade deposits is desired. Presently, the most effective and often followed route taken to utilize such deposits is the provision of beneficiation plants for upgrading iron ore and pelletizing plants for agglomerating. Kobe Steel has much experience in constructing both beneficiation and pelletizing plants and has its own pelletizing process (KOBELCO pelletizing system). This paper contains general information on beneficiation and pelletizing plants, including future expectations for them, and introduces the latest activities in connection with the KOBELCO pelletizing system, with a view to the future.*

## Introduction

The production of iron and steel has significantly expanded in recent years, particularly in newly developing countries such as China and India. This has resulted in a large increase in the demand for iron ore. The quality of iron ore deposits, however, has deteriorated worldwide as a result of long-term mining, and the existing mines are having increasing difficulty in producing ore with a high grade of iron by simple screening. Currently, blast furnaces are mainly used for ironmaking. They would suffer from greatly reduced productivity and a high energy consumption rate, if low-grade ore were charged as-is. The same applies to direct reduction furnaces. Thus, there is a strong desire to improve the iron grade at the stage of raw material preparation. One of the most common approaches is a method of upgrading ore by a beneficiation process using a physical separation technique, and a number of existing mines have introduced such beneficiation processes to upgrade their ore. Furthermore, low-grade mines, which were formerly not profitable, are being intensively developed by incorporating beneficiation plants right from the beginning.

In a beneficiation process, ore is finely ground to separate impurities. Therefore, the product ore inevitably becomes finer. Fines generated during the screening of high-grade ore can be agglomerated in a sintering plant; however, the finer fines resulting from the beneficiation process cannot usually be processed in a sintering plant and must be agglomerated in a pelletizing plant. Therefore, a greater number of pelletizing plants are expected to

be built in the future.

Kobe Steel's pelletizing process, called the KOBELCO Pelletizing System, has various advantages and incorporates many improvements made on the basis of R&D and operating experiences at the company's own facility. Kobe Steel has constructed and delivered a number of such plants across the world. The specifics of these plants are also explained in this paper.

## 1. Iron ore – supply and demand outline

### 1.1 Types of iron ore

Iron ores can be classified in different ways. The most important has to do with the iron content. In many cases, ore with a total iron content of 60% to 63%, or greater, is regarded as high grade, and ore with a lower iron content is regarded as low grade. Ores are also classified as follows, according to their size and the processing method.

- Lump: Ore lumps have diameters of approximately 10mm to 40mm and are charged as-is into a blast furnace or into a direct reduction furnace.
- Fine: Ore fines have diameters of approximately 0.15mm to 10mm and are agglomerated by a sintering plant before being charged into a blast furnace.
- Pellet feed: Pellet feeds have diameters smaller than approximately 0.15mm and are agglomerated by a pelletizing plant before being charged into a blast furnace or into a direct reduction furnace.
- Concentrate: Concentrate is ore upgraded by a beneficiation process.
- Sintered ore: Sintered ore is ore agglomerated by a sintering plant.
- Pellet: Pellet is ore agglomerated by a pelletizing plant.

### 1.2 Outline of iron ore production

The production of iron and steel in China has increased dramatically. In response to the increasing demand, China has greatly expanded its domestic

production of iron ore. However, this expansion is still insufficient, and the country is importing an increasing amount of iron ore. On the other hand, China's domestic production seems to be reaching its peak, due to a deterioration in mine quality.<sup>1)</sup> India used to be a prominent exporter of high-grade iron ore, but started to tax the export of iron ore in 2007 to prioritize its own domestic demand, and it will become difficult for India to export iron ore in the future.<sup>2)</sup> Contrary to these forecasts of increasing demand, there are predictions that steel scrap will be increasingly generated as a result of past steel production, and this will lead to an increase in the amount of steel produced using scrap and a decrease in the amount using raw iron. Overall, considering the balance of both of the above trends and also the increase in the demand for steel associated with world economic growth, the demand for iron ore is predicted to remain relatively strong.<sup>3)</sup>

### 1.3 Structure of iron ore supply

The suppliers of iron ore have undergone strategic restructuring since 2000. Three majors, namely, Vale (Brazil), Rio Tinto, and BHP Billiton (the latter two companies having two head offices, in the UK and Australia), now account for approximately 65% of the iron ore traded across the world. In addition, semi-majors such as Fortescue Metals Group Ltd, AU, and Anglo American, UK, and many other smaller businesses are producing iron ore; however, they will have limited strategic impact on the pricing and development of iron ore mines and the above three majors have a strong influence on the world market.

## 2. Outline of Beneficiation plant

### 2.1 Screening

Run-of-Mine (ROM) excavated from an ore deposit is loaded on a heavy-duty truck by a shovel or wheel loader and is transferred to a crushing process. The primary crushing is usually carried out by a gyratory crusher. This is followed by secondary crushing by a cone crusher or jaw crusher. The ore is then separated into lumps and fines. In the case of high-grade mines, the ore is shipped at this stage as the product.

### 2.2 Beneficiation process

In the case of low-grade mines or where the product iron grade needs further improvement, the secondary crushing is replaced by a beneficiation

process. As shown in Fig. 1, the beneficiation process mainly comprises the sub-processes of grinding, separating and dewatering.

#### 2.2.1 Grinding

Grinding is a sub-process of finely grinding ore in advance, such that the ground output can be physically separated into iron ore and impurities in the downstream sub-process. In many cases, an autogenous mill (AG mill) or a semi-autogenous mill (SAG mill) is used for the primary grinding, and a ball mill is used as the secondary for further grinding. An AG mill uses larger rocks of ore, while an SAG mill uses both larger rocks of ore and steel balls for the grinding. The ore to be ground is charged into a shell containing the larger rocks (and steel balls); it is cylindrical in shape and has a relatively large diameter and short length. As the shell rotates, its contents are raised high, then dropped, and the ore inside the shell is ground by the impact of the fall. A ball mill is equipment that solely uses steel balls to grind ore, and its shell body has a smaller diameter and longer length compared with an AG mill or with an SAG mill.

#### 2.2.2 Separation

The ground material is separated into useful ore and impurities in a separation process. Two types of separators: i.e., a separator based on the difference in

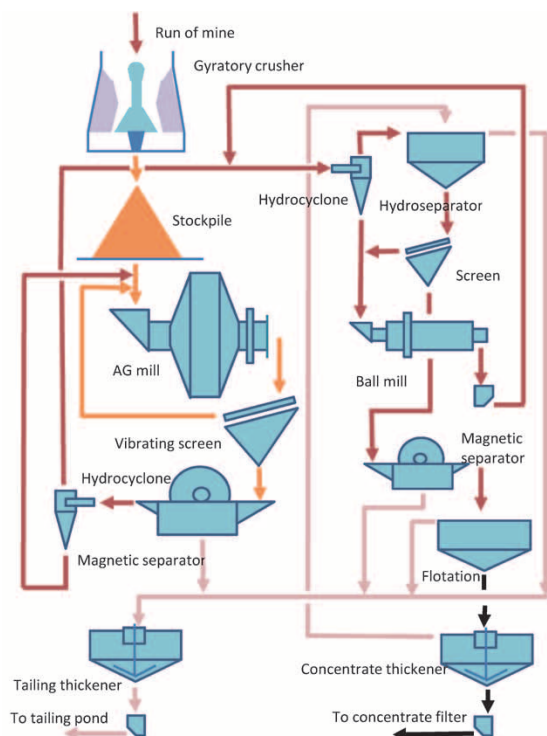


Fig. 1 Example of process flow in beneficiation plant

physical properties (e.g., gravity separator, magnetic separator or flotation separator) and a separator based on size (e.g., screen and screw classifier) are usually provided together.

### 1) Gravity separation

The true specific gravity of iron ore is approximately  $5\text{t/m}^3$  and is quite different from the specific gravities of major impurities such as silica and alumina (approximately  $2.7\text{t/m}^3$ ). Gravity separation is a method of separating iron ore from impurities on the basis of the difference in their specific gravities. Gravity separators include jig separators, which utilize the difference in the fall velocity in water of objects with different specific gravities, and spiral separators and cyclone separators, which utilize centrifugal force. These separators are the least expensive of the various apparatuses used for the separation process. Some beneficiation processes rely solely on gravity separation, and many others incorporate gravity separation as a pretreatment step for flotation separation and magnetic separation. Gravity separation is used for relatively coarse ore (diameters of approximately 0.1mm to 1.5mm.)

### 2) Magnetic separation

Magnetic separation is a technique for separating iron ore from impurities on the basis of the difference in their magnetic properties. This type of separation is widely used for the beneficiation of magnetite ore. A drum with a permanent magnet is rotated in slurry and the result is that magnetite ore, which is magnetic, becomes attached to the surface of the drum and is separated from the slurry, while non-magnetic impurities remain in the slurry, thus accomplishing the separation. The separation of hematite ore, which is weakly magnetic, employs an apparatus with an electromagnet that can generate a stronger magnetic force. Recently, such an apparatus is also being used commercially to collect hematite ore from the tailings. Magnetic force separation is applied to relatively fine ore with diameters of approximately 0.05mm to 1mm.

### 3) Flotation separation

Flotation separation is a technique utilizing the difference in the hydrophilicity of ore surfaces. This technique is used for raw materials with small diameters of approximately 0.01mm to 0.1mm and is often applied to the final stage of grade improvement, or to the removal of impurities such as sulfur and phosphorus. The iron ore and major impurities have a similar hydrophilicity; but adding a chemical (collector agent) that is adsorbed selectively to either iron ore or impurities makes the surface with the adsorbed agent hydrophobic. Air bubbles are then charged from the bottom to be

trapped by the hydrophobic surfaces, after which, they float up due to the decrease in density caused by the trapped air. This phenomenon is used to accomplish flotation separation.

### 2.2.3 Dewatering

The above separations are usually performed in wet conditions for ease of handling and to prevent dust generation. Hence, the separated concentrate is in the form of slurry and requires dewatering. This dewatering is done by filtering the concentrated slurry. Vacuum filters are widely used; however, it is difficult to decrease the water content of the cake after filtration to 9% or lower, and the residual water content increases when the ore is finer, or when the system is installed at a high altitude. A gradually increasing number of systems have recently been employing pressure filters, adapting pneumatic pressure or hydraulic pressure to reduce the moisture content to a level of 8%.

## 2.3 Transportation

Usually, the transportation from a mine to a shipping port is done by rail. Fine ore, on the other hand, can be transported through pipelines in the form of slurry. A typical example of this is found in projects at Samarco in Brazil. Samarco uses two pipelines, each having a total length of 396km, to transport 24 million tonnes per year of iron ore. One of the two was inaugurated in 1977 and still is used. Even though it calls for a booster pump to provide the pressure required for the long distance transportation, the running cost is lower compared with transportation by rail. Therefore, slurry transportation is effective for beneficiation plants as long as a sufficient amount of water is available.

## 3. Outline of agglomeration plant

Among iron ore products, fines and pellet feed are so fine that they cannot be charged as-is into a blast furnace or into a direct reduction furnace. The processes for agglomerating them into chargeable material are sintering and pelletizing; the main raw material for the former is fines and for the latter, pellet feed.

### 3.1 Outline of sintering plant

**Fig. 2** depicts the process flow of a sintering plant. Raw materials including iron ore fines, limestone and coke breeze (in addition, burnt lime and dolomite as required) are mixed and placed

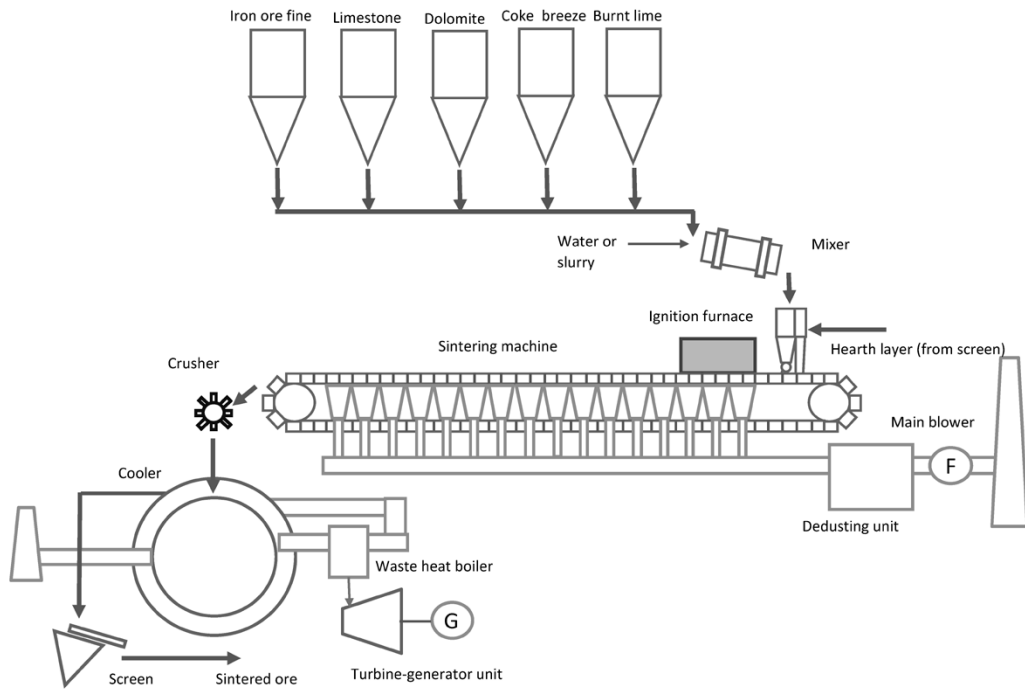


Fig. 2 Typical flow of sintering plant

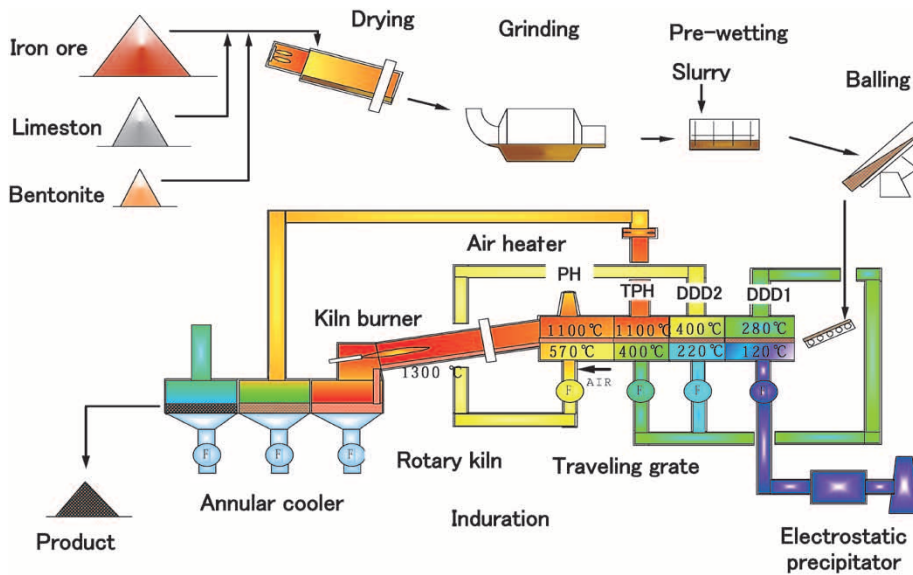


Fig. 3 Typical flow of KOBELCO pelletizing system

uniformly on moving cars that have a grate structure. The coke breeze is ignited in an ignition furnace and the mixture is agglomerated by the heat of the combustion of coke breeze. The agglomerated materials are cooled in a cooler that is either circular or linear and are delivered as products. In many cases, the sensible heat of the exhaust air from the cooler is recovered by a waste-heat boiler.

The sintered ore thus produced is un-uniform in shape and generates dust during transportation. Because of this, sintering plants are usually built in steelworks. Typically, these plants have capacities of 5 Mt/y to 6 Mt/y, while larger plants with capacities of 8 Mt/y to 8.5 Mt/y are also in service. Sintering

plants can recycle relatively coarse dusts generated in steelworks. On the other hand, they consume a large amount of coke breeze, and their exhaust gas contains a certain amount of sulfur oxides. For this reason, an increasing number of sintering plants are equipped with exhaust gas desulfurization systems.

### 3.2 Outline of pelletizing plant

Fig. 3 illustrates the flow of a pelletizing plant (KOBELCO pelletizing system).<sup>4)</sup> Finely ground raw material is mixed with binder and is granulated into balls (green balls) with a diameter of approximately 12mm. These balls are dried, preheated, fired and



cooled to become product pellets.

The product pellets are spherical with high strength and thus generate little dust during transportation. The plants are usually built in the vicinity of a mine, or near the ore shipping port; however, as in the case of Kobe Steel's Kakogawa works, a pelletizing plant is often built in steelworks. The granulation is done by a balling disc or by a balling drum. The firing is performed in a grate-kiln-cooler system, as adapted by the KOBELCO pelletizing system, or in a Straight grate system<sup>5)</sup> similar to the one used for a sintering plant.

Until 2000, there had been only two lines of plants with a capacity of 6 Mt/y; however, the enlargement of the plant progressed rapidly thereafter, and nine lines are currently in service with capacities exceeding 6 Mt/y. In addition, three more production lines are to be built in few years. The maximum capacity among these lines is to be 8.3 Mt/y (under construction), which compares with the capacity of a sintering plant. On the other hand, a number of small facilities (0.6 Mt/y to 1.2 Mt/y) have been built and are in service in the vicinity of mines in India and China.

#### 4. Development of state-of-the-art technology for Kobe Steel's pelletizing plant

The specifics and features of the Kobe Steel's pelletizing plant were introduced previously.<sup>4)</sup> This paper focuses on the technologies developed since then.

##### 4.1 Selective non-catalytic reduction

Countries throughout the world, including developing nations, require that everything possible be done to reduce the environmental impact. With this in mind, a new method has been developed for reducing nitrogen oxide (NO<sub>x</sub>). The new technique belongs to the category of selective non-catalytic reduction (SNCR) and comprises the spraying of ammonia in a relatively high temperature (900 to 1,200°C) zone for a relatively long period of time to have it react with nitrogen oxide in the zone. A newly devised spraying method has enabled the features of high efficiency and a significantly reduced amount of leakage ammonia, as shown in Fig. 4. This method is applied to the preheating (PH) zone of the traveling grate, which enables the reduction of the amount of nitrogen oxide without much additional capital investment. A typical flow of this process is shown in Fig. 5.

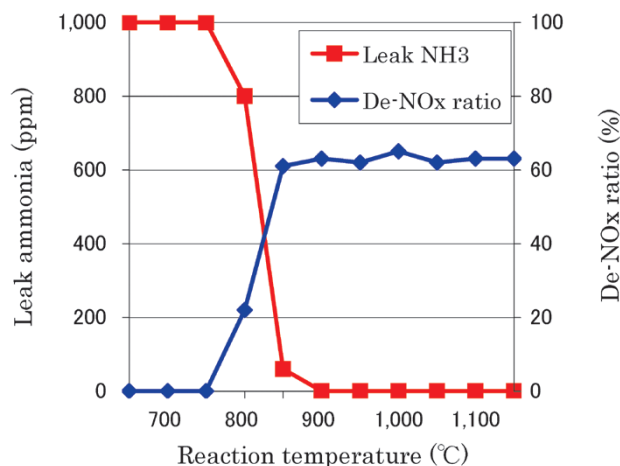


Fig. 4 Typical example of effects of SNCR system

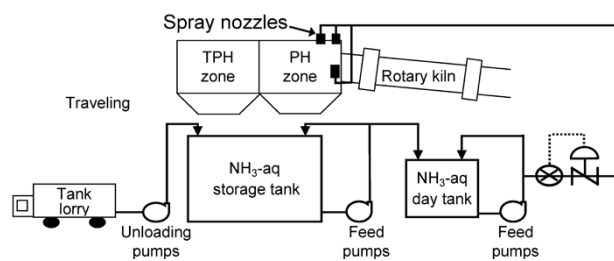


Fig. 5 Typical application of SNCR system on pelletizing plant

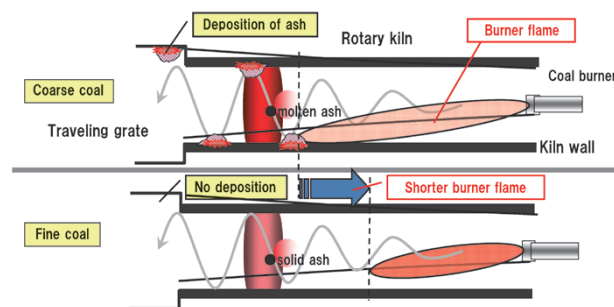


Fig. 6 General image showing relationship between kiln burner and coal ash deposition

##### 4.2 Increased applicability of coals for kiln

The KOBELCO pelletizing system uses a kiln for firing, enabling the replacement of its main fuel, expensive oil and gas, with inexpensive coal. Inexpensive coal, however, contains a certain amount of ash, which can be deposited on and adhere to the interior of the kiln; this may disturb gas passage in the kiln. Several measures have been devised to prevent such troubles. Of all these measures, shortening the flame of the kiln burner and using more finely ground coal have been found to be particularly effective. This has also been confirmed by actual operation. Fig. 6<sup>6)</sup> shows a general image of the kiln burner and the deposition of coal ash. In a case where the flame reaches the

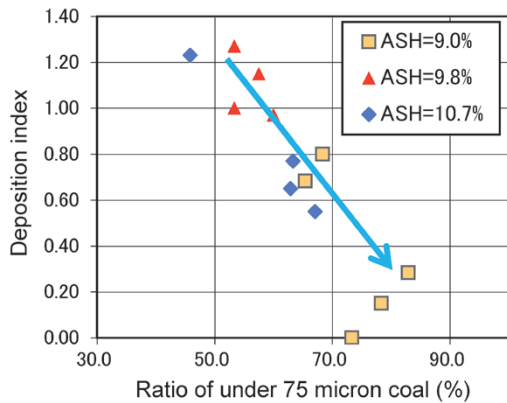


Fig. 7 Relationship between coal fineness and ash deposition

interior wall of the kiln, coal ash reaches the wall in a molten state, being deposited on and adhering to the wall surface. When the flame is shorter, the ash is cooled before it reaches the interior wall and is solidified, which prevents it from adhering to the wall. Fig. 7 is the result of an operational test showing the relationship between the fineness of the coal and the deposition of coal ash at the kiln inlet.<sup>6)</sup> The finer the coal is ground, the smaller the deposition index (relative amount of deposition).

## 5. Future trends in pelletizing plants and Kobe Steel's actions

### 5.1 Future trends in the agglomeration process

As has been described, the deterioration of mines has increased the introduction of beneficiation processes. Involving grinding, these processes produce concentrate that consists of extremely fine grains. The grains are so small that their use in a sintering plant is limited and they will be increasingly used in pelletizing plants. Meanwhile, it has been recognized that, with the improvement in the high-temperature properties of pellets, high iron grade pellets can be charged into a blast furnace at a high mixing ratio so as to effectively decrease the amount of slag, reductant and CO<sub>2</sub> emissions.<sup>7)</sup> Therefore, it is envisaged that part of the sintered ore charged into a blast furnace will be replaced by pellets. This trend will be accelerated because the environmental impact of pellet production is much smaller than that of sintering processes that consume large amount of coke breeze.

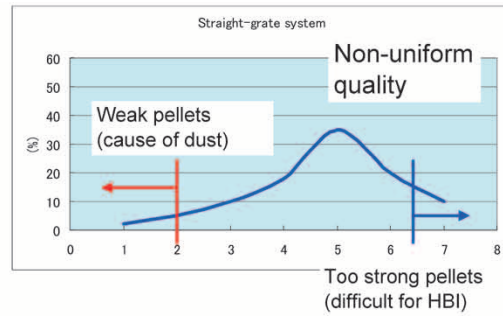
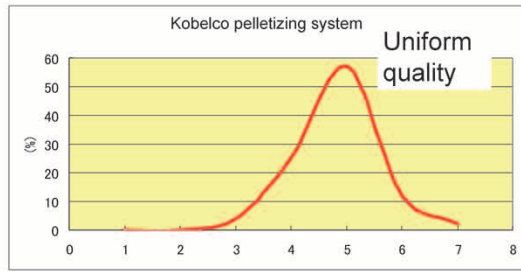
It should also be noted that there will be a further increase in the consumption of pellets by the direct reduction process. Pellets usually contain a high grade of iron and generate little dust. With these favorable features, pellets are predominantly used as a raw material for direct reduction. The direct

reduction process is expected to greatly expand in the future, because the demand for inexpensive raw iron that exploits shale gas is increasing, and so is the demand for direct reduced iron (DRI) and hot briquetted iron (HBI) as clean raw iron for steelmaking processes based on scrap. Hence, the demand for pellets is also expected to increase significantly.

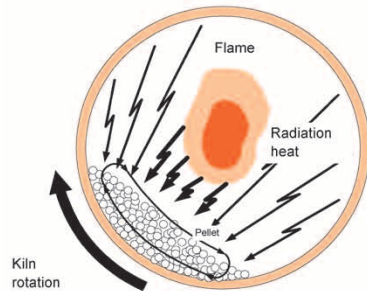
### 5.2 Future trends in large-scale plants

Where there is a large deposit of iron ore, a large-scale pelletizing plant is planned because of its investment efficiency. The construction site is selected near a shipping port to facilitate construction and operation. With the recent increase in the scale of pelletizing plants, each pelletizing plant is required to have a production capacity of 6 Mt/y or greater. It must run with a low consumption rate and produce high quality pellets to keep its product competitive. In particular, there is a stringent requirement for its products to generate as little dust as possible because they are shipped all over the world.

In 2010, Kobe Steel constructed a pelletizing plant with a production capacity of 6 Mt/y in Bahrain, and with this experience, the company will now be able to build a plant with a capacity of 8 Mt/y. Compared with Straight grate systems, the KOBELCO pelletizing system uses less process gas and operates with a thinner bed of green ball, thus consuming less electric power for its process fan. This system also realizes low fuel consumption, one of the lowest in the world, thanks to its optimized heat recovery process. Moreover, the kiln used for the firing process enables the pellets to be fired while tumbling. This tumbling action makes the pellets stronger with less strength variation, as shown in Fig. 8,<sup>8)</sup> which effectively prevents the pellets from breaking during long-distance transportation. In a Straight grate system, heating is applied only from above the static layer of pellets, which causes a large difference in strength between the top layer and bottom layer. The pellets in the bottom layer, which are weaker, tend to break during transportation. Increasing the average strength of the pellets may improve this issue; however, this may lead to the inclusion of pellets with excessively high strength. When producing HBI in a direct reduction process, these excessively strong pellets make briquetting difficult. Thus Kobe Steel's process, capable of producing homogeneous pellets, is more suitable for HBI production.



due to tumbling action of pellet



due to static bed firing

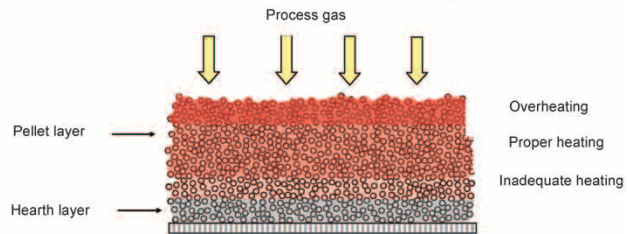


Fig. 8 Comparison of product pellets

### 5.3 Future trends in medium-scale plants

Investing in medium-scale plants is less efficient than investing in large-scale plants. Therefore, medium-scale ones are usually built on the sites of steelworks so as to realize advantages that compensate for the investment inefficiency. A production capacity of 3 to 4 Mt/y is required. Such a built-in plant has the following advantages over stand-alone plants:

- It can utilize a small-scale feed of iron ore as a part of the raw material.
- It can produce pellets of a quality optimally designed for the steelworks of the owner company.
- It can use byproduct gases of the steelworks as a fuel for pelletizing, which enables the low-cost production of pellets.
- It can be both maintained and managed by the same personnel.
- It can recycle dust generated in other facilities as raw material for pelletizing.

Kobe Steel owns a pelletizing plant in the company's integrated steelworks with blast furnaces and has accumulated a wealth of knowledge and experience from it. For example, the company effectively recycles and utilizes converter furnace dust as the raw material of pellets. Such fine dust can work as a binder, and the converter furnace dust has actually been confirmed to reduce the amount of binder used as a secondary effect. The coal utilization technology described above has enabled the use of inexpensive steaming coal to be used for

the pelletizing process, which has decreased the fuel cost.

### 5.4 Future trends in small-scale plants

A number of mines with relatively small deposits are found in India and China, but they had never been the objects of development due to the low return on investment. With the recent continued high price of iron ore, however, it is anticipated that there will be more and more development of these mines.

In the case of small mines, pelletizing plants are most likely to be built with beneficiation plants in the vicinity of the mines. Such integration of plants makes it possible to do without facilities for storing concentrate. In addition, collective construction can suppress construction costs. Kobe Steel has a lineup of small-scale standard plants with a capacity of 2.5 Mt/y and aims at expanding their sales in the future.

### Conclusions

Regarding the future production of iron, steel and iron ore, a steadily increasing number of projects will be launched that involve beneficiation processes to upgrade ore and to produce pellets. Kobe Steel has its own pelletizing technology and has built eleven pelletizing plants in six countries so far. The company is highly reputed for the quality of its product pellets and for its know-how in using coal as the main fuel. In addition, the company has built a large-scale beneficiation plant for iron ore. Kobe

Steel will continue to strive to expand the sales of these plants and to contribute to the development of iron ore and steel industries.

## References

- 1) Magnus Ericsson. JOGMEC Metal Resources Report. 2010. 3, p.99.
- 2) TEX Report. Iron Ore Manual, 2012, p.76.
- 3) S. Kozawa. JOGMEC Metal Resources Report. 2012. 5, p.47.
- 4) S. Yamaguchi et al. R&D Kobe Steel Engineering Report. 2010, Vol.60, No.1, p.15.
- 5) S. Yamaguchi et al. R&D Kobe Steel Engineering Report. 2010, Vol.60, No.1, p.15.
- 6) Y. Takiguchi et al. COREM 3rd symposium on iron ore pelletizing. 2013, Oct.
- 7) <http://www.lkab.com>
- 8) S. Yamaguchi et al. R&D Kobe Steel Engineering Report. 2010, Vol.60, No.1, p.17.

---

Note) The names of companies and products cited herein may be trademarks or the registered trademarks of their respective owners.



# Application of Coke Oven Gas to MIDREX<sup>®</sup> Process

Noriaki MIZUTANI \*1, Takashi KISHIMOTO \*1, Norihide MAEDA \*1

\*1 Technology & process Engineering Dept., Iron Unit Div., Engineering Business

*The MIDREX<sup>®</sup> process runs without coke, emits less CO<sub>2</sub> and thus is gathering attention as an alternative process for blast furnace ironmaking. To expand business opportunities, a study has been conducted on the use of coke oven gas (COG) so as to diversify the MIDREX process. The study has resolved most of the technical issues for commercialization, as reported in this paper.*

## Introduction

Midrex Technologies, Inc. (hereinafter referred to as "Midrex Inc."), a wholly-owned US subsidiary of Kobe Steel, possesses the MIDREX<sup>®</sup> process using natural gas as a source gas for reducing iron ore. The MIDREX process runs without coke, emits less CO<sub>2</sub> and thus is considered to be an alternative to the blast furnace ironmaking process.

With the shale gas revolution in recent years, the MIDREX process is gathering attention as a process for producing direct reduced iron (DRI) using natural gas. To further promote the business opportunities, Kobe Steel has been carrying out studies on the diversification of the reductant gas used for the MIDREX process. The company has resolved most of the technical issues in commercializing a MIDREX process that uses coke oven gas (hereinafter referred to as "COG") as its reductant gas. This paper gives an outline of the study.

## 1. MIDREX process

The flow of the MIDREX process is shown in Fig. 1. Natural gas is reformed by a reformer and is

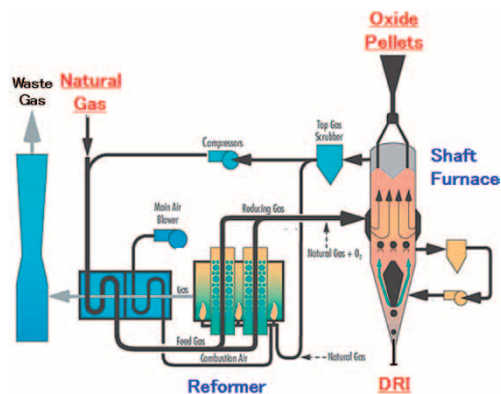
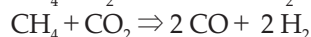
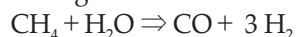
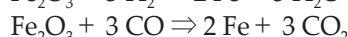
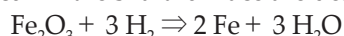


Fig. 1 Flow of MIDREX process

fed into a shaft furnace as reductant gas containing CO and H<sub>2</sub>. The reforming reactions of natural gas, the reactions taking place in this reformer, consist of the following steam reforming reaction and CO<sub>2</sub> reforming reaction:



Meanwhile, the raw material iron oxide (i.e., lump ore or fired pellets) is reduced by CO and H<sub>2</sub> in the shaft furnace, and DRI is discharged from the bottom of the furnace. The reduction reactions that occur in the shaft furnace are described as follows:



## 2. MIDREX plant

In 1967, a pilot plant was built for the MIDREX process. Two years later, in 1969, the first commercial plant was inaugurated in the state of Oregon, U.S. This paved the way for approximately seventy plants currently in operation around the world.<sup>1)</sup> Fig. 2 shows the locations of the MIDREX plants actually built. These plants are producing approximately 60% of the DRI produced in the world. In 2012, they produced 45 million tonnes of DRI out of the world's total DRI production of 74 million tonnes.<sup>2)</sup>

This share of 60% is mainly supported by the dramatic increase in the production capacity per plant, while keeping a high annual operation ratio for each. Around 1983, when Kobe Steel purchased Midrex Inc., the maximum annual capacity per plant was 0.6 million tonnes. The technological innovations since then have more than tripled the annual capacity, to 2 million tonnes per year.

## 3. Diversification of reductant gas for MIDREX process

The MIDREX plants account for approximately 60% of the world's DRI production. They are limited to natural gas producing regions such as the Middle East and Northern South America, because they use natural gas as the source for their reductant gas (Fig. 2).

Against this background, Kobe Steel has been carrying out studies on the diversification of the reductant gas to promote the business opportunities

note) MIDREX is a registered trademark of Kobe Steel.

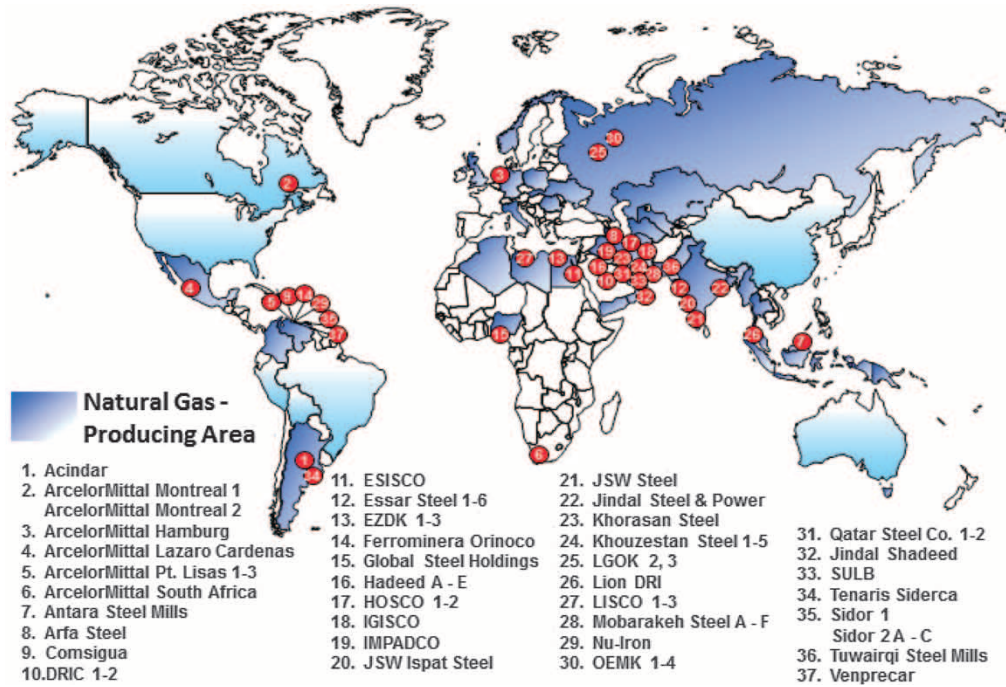


Fig. 2 MIDREX plants actually built

of the MIDREX plants. One commercial example is the use of the off-gas from the COREX process. **Fig. 3** shows the flow of a process combining the COREX process and MIDREX process. The COREX is a process in which ore lumps and/or pellets are reduced in a shaft furnace until their metallization reaches approximately 90%, and the remainder is reduced and melted by a gasifier melter. In 1999, a plant integrating the COREX process and MIDREX process started commercial production at ArcelorMittal South Africa.

Meanwhile, Midrex Inc. has developed a process using reductant gas from coal gasification (**Fig. 4**). A first plant is being built for Jindal Steel and Power Limited (JSPL) in India and is planned to start commercial production in 2014.

In addition, a study was conducted on the application of coke oven gas (COG) as the source for the reductant gas of a MIDREX plant. This study revealed that the then-current technology allowed only a small amount of COG to be used because COG contains tar and unsaturated heavy hydrocarbon. However small the amount may be, COG can still be used to partially substitute for the natural gas. For this reason, a project is ongoing for JSW Steel in India, in which a MIDREX plant currently in operation will be modified so that COG can be utilized. The plant is planned to start commercial production at the end of 2014.

An index for reductant gas,  $H_2/CO$  ratio, is greatly affected by the type of the reductant gas source: i.e., natural gas, COREX off-gas and coal gasification gas (**Table 1**). The COREX off-gas with

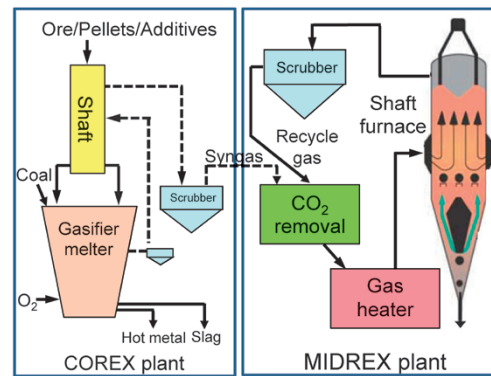


Fig. 3 Combination of COREX plant and MIDREX plant

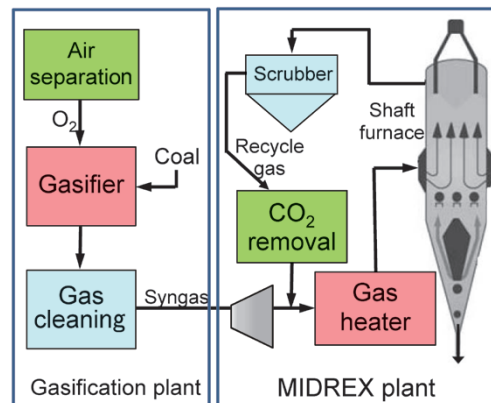


Fig. 4 Combination of coal gasification plant and MIDREX plant

Table 1  $H_2/CO$  ratio due to reformed gas source differences (example)

	Natural gas base	COREX offgas	Coal gasification gas
$H_2/CO$	1.5~1.7	0.3~0.4	2.0

a low H<sub>2</sub>/CO ratio contains a larger amount of CO, which gives rise to CO reduction reaction in the shaft furnace. Unlike endothermic H<sub>2</sub> reduction reaction, the exothermic CO reduction reaction, if its amount is increased, raises the temperature and facilitates the partial melting and clustering of the pellets in the furnace. For this reason, the plant at ArcelorMittal South Africa, using COREX off-gas, must run with the gas temperature at the entrance of the shaft furnace set 100°C to 150°C lower than a regular natural-gas based process.

#### 4. Toward use of COG for MIDREX process

In order to effectively exploit COG as the source of reductant gas, the development of technologies to reform COG has been pursued for many years in various countries. Examples include the development of reforming catalyst by a catalyst manufacturer and non-catalytic partial oxidation by steaming.<sup>3)-7)</sup> Hardly any catalyst, however, has been commercialized, due to the decline of catalytic activity caused by sulfur content as low as several hundred ppm and also due to the issues of carbon precipitation caused by unsaturated heavy hydrocarbon. Non-catalytic partial oxidation, on the other hand, requires large reactor vessels for commercialization, which tends to make the mixing of steam and COG gas inhomogeneous.<sup>8)</sup> For that reason, this method also has rarely been implemented at a commercial level.

As described above, Kobe Steel in the meantime has applied a small amount of COG to the MIDREX process for JSW Steel in India. As a next step, the company has started collaborating with Midrex Inc. to utilize a larger amount of COG as a source for reductant gas. The target geographical regions include some parts of India and China where natural gas is unavailable but there is a surplus of COG.

**Table 2** shows the composition of the COG studied for the above described project in India. As shown in this table, the COG contains at least 60%

Table 2 Gas composition of COG

	Vol%
H <sub>2</sub>	55
CO	7
CO <sub>2</sub>	3
H <sub>2</sub> O	4
CH <sub>4</sub>	25
C <sub>n</sub> H <sub>m</sub>	5
Tar	1
H <sub>2</sub> S	300ppm

of reductant such as H<sub>2</sub> and CO, however, it also contains 25% of CH<sub>4</sub> and 5% of C<sub>n</sub>H<sub>m</sub>, which makes it difficult to substitute for general reformed gas (containing 1% to 4% of residual CH<sub>4</sub> and almost 0% of residual C<sub>n</sub>H<sub>m</sub>.)

Tar, contained in the amount of 1%, consists mainly of monocyclic aromatic hydrocarbon (e.g., benzene and toluene) and polycyclic aromatic hydrocarbon (e.g., naphthalene). Including trace constituents, the tar is reported to contain dozens of compounds. This makes the decomposition, or the oxidation reaction, of tar extremely complex, rendering it difficult to decompose all the tar content.

It was against this background that Kobe Steel searched for various newly developed technologies and came to the conclusion that a method using an oxygen burner, the method being developed by Praxair Inc., appeared to be the most promising. Kobe Steel then started joint development involving Praxair Inc.

#### 5. Reforming of COG using oxygen burner

**Fig. 5** schematically illustrates an oxygen burner from Praxair Inc. This burner is designed such that the linear velocity of the combustion gas at the burner exit becomes as high as 900m/s. This causes the COG, fed from the side at the burner exit, to be caught by the strong propulsive force of the combustion gas, which facilitates the mixing of the combustion gas and COG.<sup>9)</sup> Meanwhile, the combustion gas at the burner exit has a temperature exceeding 2,000°C, as well as a high concentration of water vapor. This promotes the efficient decomposition of the tar in COG. In addition, the residual oxygen contained in the combustion gas causes partial oxidation of the CH<sub>4</sub> and H<sub>2</sub> contained in the COG at a high temperature (equation (1) below). This enables the production of a greater amount of reformed gas consisting of CO and H<sub>2</sub>.

It should be noted, however, that when the combustion gas and COG are insufficiently mixed and the oxygen concentration becomes distributed, the combustion reactions (equations (2) to (6)) are promoted in the oxygen rich region, causing increased amounts of water and carbon dioxide to be

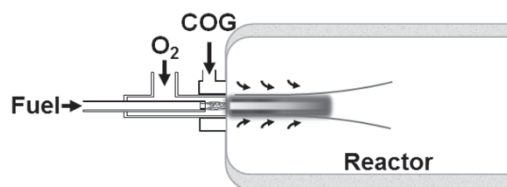
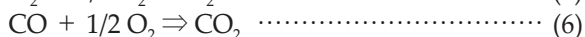
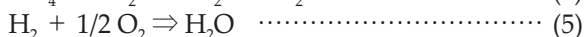
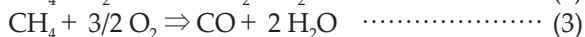


Fig. 5 Conceptual diagram of Praxair's oxygen burner



generated.

Thus, the most important technical issue for a commercial plant with a large-sized burner is to promote the mixing of combustion gas and COG.



Therefore, a lab-scale test was conducted using an oxygen burner from Praxair Inc. The results confirmed that the tar is decomposed while the CH<sub>4</sub> in the COG is reformed, producing usable reformed gas.

Next, an attempt was made to scale-up the laboratory processing capacity of several Nm<sup>3</sup>/h of COG, while confirming whether or not the same reforming effect is reproducible on a larger scale. A pilot test, with a processing capacity of several tens Nm<sup>3</sup>/h of COG, was performed at Praxair Inc. Tests conducted under various combustion gas temperatures confirmed that the tar contained in the COG (in the test, benzene was used as a substitute) can be decomposed under certain conditions. More specifically, the states of reformed gas were checked under various oxygen/fuel ratios, while the amount of soot, which can build up and cause problems in the latter process, was also checked.

When benzene (C<sub>6</sub>H<sub>6</sub>) is decomposed under a gas temperature that is not high enough and/or with a low concentration of water vapor, the decomposition proceeds only to C<sub>2</sub> or C<sub>3</sub> species. The general understanding is that these C<sub>2</sub>/C<sub>3</sub> species electrically attract each other to form fine particles, and these fine particles repeatedly collide and coalesce to form soot.

This implies that the generation of soot may possibly be suppressed if the conditions of high temperature and high concentration of water vapor are met. However, on the other hand, an attempt to raise the gas temperature may result in the production of a decreased amount of reformed gas and the consumption of an increased amount of oxygen, which decreases the cost effectiveness. Therefore, the key to accomplishing the primary objective of using COG as a source of reformed gas is to find the conditions that will prevent the generation of soot, while avoiding an excessive rise in temperature.

Kobe Steel has explored various measures through the pilot test and, as a result, confirmed that the generation of soot can be prevented under conditions almost equal to those of the laboratory test. In other words, the pilot test has achieved

mixed state approximately equivalent to that achieved on the laboratory scale.

## 6. Demonstration test of oxygen burner

Judging from the maximum capability of the Praxair's oxygen burner, a commercial plant adopting the oxygen burner will have a COG processing capacity of several tens of thousands Nm<sup>3</sup>/h per oxygen burner. The apparatus used for the pilot test, on the other hand, is about 1/500 to 1/200 the size of the apparatus for the commercial plant. The risk of scaling-up the pilot test, by a factor of several hundreds, to a commercial level was considered to be too high. Therefore, a demonstration plant on a scale of approximately 1/20 of that of the commercial plant was introduced to the Research and Development Technology Center, Midrex Inc. (Fig. 6.)

One persistent problem encountered during this demonstration test was the generation of a large amount of soot, an issue that had been suppressed in the pilot test. The cause was found to be the fact that the demonstration plant is larger than the pilot plant by a factor of several tens, which resulted in an insufficient mixing of the combustion gas with COG. Measures were then devised to facilitate mixing without increasing the temperature of the gas at the exit. The following implementations were confirmed to be effective in improving the mixing state, and no soot was found to be generated under operating conditions almost equal to those of the pilot test.

- i) Optimizing the supply point of COG and the nozzle size of the supply point
- ii) Optimizing the linear velocity of the combustion gas

In this demonstration test, toluene was used as a replacement for tar. This was done because toluene is available in quantities of several tonnes, exhibits the slowest oxidative degradation among the substances contained in tar, and is easiest to handle from the aspect of safety.

It was judged that, if toluene, with the slowest



Fig. 6 Demonstration plant (left) and reactor (right)



rate of oxidative degradation, is almost completely decomposed, the other components of tar would all have been decomposed. It should be noted that the tar contained in the actual COG is approximately 1%, as shown in Table 2, while the demonstration test ascertained that no soot was generated in conditions containing up to 1.9% of toluene.

## 7. General flow of commercial plant

Fig. 7 shows the outline flow of a commercial plant designed on the basis of the reformed gas composition obtained by the demonstration test. As shown in this figure, the MIDREX process based on reformed COG has been confirmed. The marketing of this system has been implemented in India, China and other countries. The "THERMAL REACTOR SYSTEM®" in the figure represents a COG reforming system including the reactor. Kobe Steel has registered it as a trade mark in the U.S. and other countries.

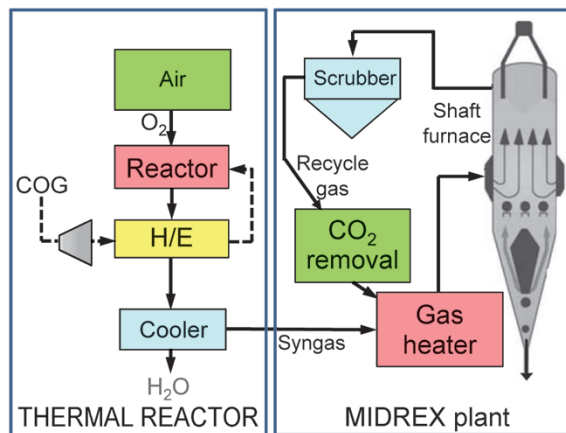


Fig. 7 Supposed general flow in commercial plant

## Conclusions

A MIDREX process based on reformed COG has been established as a result of problem solving through collaboration with Midrex Inc. and Praxair Inc. This collaborative project involved laboratory testing, a pilot test and demonstration test.

Recently, the demand for DRI to be used as a substitute for scrap as a clean iron source is expanding even in the advanced countries. An increasing amount of steel is being produced in electric arc furnaces worldwide.<sup>10</sup> Kobe Steel will continue to strive for the diversification of reductant gas and thus contribute to the iron and steel production of the world.

## References

- 1) M. Atsushi et al. Kobe Steel Engineering Reports. 2010, Vol. 60, No.1, p.5-11.
- 2) Midrex. 2012 World Direct Reduction Statistics.
- 3) T. Takarada. Post-project evaluation report, NEDO (2010). Development of non-catalytic coal carbonization gas reforming technology.
- 4) K. Fujimoto et al. Shinnittetsu Giho. 2011, No.391, p.201-205.
- 5) Japanese published unexamined patent application. H6-279769.
- 6) Japanese published unexamined patent application. 2001-220584.
- 7) Japanese published unexamined patent application. 2011-11959.
- 8) K. Norinaga et al. JFE 21st Century Foundation, Technical Report (2007). [www.jfe-21st-cf.or.jp/jpn/hokoku\\_pdf\\_2007/06.pdf](http://www.jfe-21st-cf.or.jp/jpn/hokoku_pdf_2007/06.pdf) (accessed 2013-11-25).
- 9) S. Halder. Praxair Inc. Reports, Papers, Case Studies & Presentations Home Page Paper 2011 AI STech Hot Oxygen for Coal Combustion Halder.pdf. <http://www.praxair.com/resource-library/reports-paperscase-studies-and-presentations> (accessed 2013-11-25).
- 10) Y. Yamada. NKK Techno Service Co., Ltd, Research Report on New Iron Source (1996).

Note) The names of companies and products cited herein may be trademarks or the registered trademarks of their respective owners.

# Evaluation of Spontaneous Combustion in Stockpile of Sub-bituminous Coal

Dr. Haeyang PAK \*<sup>1</sup>, Toshiya TADA \*<sup>2</sup>, Naoki KIKUCHI \*<sup>3</sup>, Takuo SHIGEHISA \*<sup>3</sup>, Toru HIGUCHI \*<sup>3</sup>,  
Dr. Seiichi YAMAMOTO \*<sup>4</sup>

\*<sup>1</sup> Mechanical Engineering Research Laboratory, Technical Development Group

\*<sup>2</sup> Mechanical Engineering Research Laboratory, Technical Development Group (currently Kobelco Eco-Solutions Co., Ltd.)

\*<sup>3</sup> Coal & Energy Technology Dept., Technical Development Group

\*<sup>4</sup> Coal & Energy Technology Dept., Technical Development Group (currently New Energy and Industrial Technology Development Organization)

*Spontaneous combustion in coal stockpiles is one of the problems encountered when utilizing coals such as sub-bituminous coal and lignite that contain highly volatile matter. A method has been developed for simulating the spontaneous combustion in coal stockpiles. This method involves unsteady analysis taking into account the flow behavior of air flowing through the pile, low-temperature oxidation behavior of coal in the pile, evaporation, absorption and desorption behaviors of moisture in the coal. The simulation enables the evaluation of the temperature change in a coal stockpile without any large-scale temperature measurement. The simulation results show that the heat tends to be generated at the foot of each stockpile where the breathability is high. It has also been confirmed that the stockpile of sub-bituminous coal exhibits a faster temperature rise because the coal has an oxidation reactivity higher than that of bituminous coal.*

## Introduction

Coal is the resource that accounts for approximately 24% of the primary energy consumed in Japan, which imports most of this resource from other countries. According to Trade Statistics of Japan, the amount of coal imported reached 185.15 million tonnes in 2012.<sup>1)</sup> Approximately 60 percent of this amount is occupied by steaming coal used for fueling commercial and industrial boilers. In many cases, high-grade bituminous coal is used for this purpose. A coal with a higher degree of coalification has a higher carbon content. The Japanese Industrial Standard (JIS M1002) classifies coals according to their calorific values on the moisture-ash-free basis: i.e., bituminous coal with a calorific value of 33,910kJ/kg or higher, sub-bituminous coal with a calorific value from 30,560kJ/kg to 33,910kJ/kg (exclusive of 33,910kJ/kg), and lignite (brown coal) with a calorific value from 24,280kJ/kg to 30,560kJ/kg (exclusive of 30,560kJ/kg).

Coal-fired power generation plants are equipped with facilities for storing coal imported from other countries. These storage facilities are roughly classified into two types; i.e., outdoor coal storage and indoor coal storage. In outdoor coal storage such as that involving a stockpile (hereinafter "pile"), stackers and reclaimers are used for piling and

delivering the coal; therefore, this type of storage is used in many cases by steelworks and thermal power generation plants on large sites. On the other hand, indoor coal storage, using silos, for example, is increasingly being adopted these days by plants with limited space and/or those with concern for the neighborhood environment.<sup>2)</sup> A coal yard generally has a storage capacity equivalent to the amount of coal consumed in one to two months, depending on the scale of the steelworks or thermal power generation plant.

When storing coal for an extended period of time, attention must be paid to the possibility of spontaneous combustion. The temperature inside a pile immediately after the piling is approximately 30°C to 40°C, but it rises gradually due to the heat generated by low-temperature oxidation of the coal. The temperature of a pile is determined by the balance of the heat of coal oxidation, the latent heat of water evaporation and the heat dissipated from the pile by air flow. It is considered that the temperature continues to rise at a spot where heat generation dominates, which eventually leads to spontaneous combustion.<sup>3)</sup>

In many cases, the spontaneous combustion characteristics of coal are evaluated by measuring the change of temperature caused by the self-heating of a sample in an adiabatic system.<sup>4)</sup> It has been known that coal with strong oxidizing properties, such as a high O/C ratio (the ratio of oxygen to carbon contained in coal) and large specific surface area, is more prone to spontaneous combustion (internal factors). When considering the spontaneous combustion characteristics of coal in storage, the effect of external factors, such as the particle size distribution and the filling state of the coal, the amount of sprinkled/precipitated water and ambient temperature, must also be taken into account. As an evaluation method taking into consideration both the internal and external factors, long-term experiments extending over several months have been conducted to measure the temperature of test piles, each consisting of several thousand tonnes of coal.<sup>5), 6)</sup> This method is useful for evaluating the spontaneous combustion characteristics of a new type of coal that has not been used before, but is

costly.

Recently, the supply sources of coal are becoming more diversified and coals are becoming more degraded. As a result, thermal power generation plants in Japan are using various types of coal. Above all, these plants are increasingly using coals such as sub-bituminous coal, which has a high O/C ratio and is more prone to spontaneous combustion than bituminous coal. These types of coals are expected to see increased use. Therefore, it is important to understand the spontaneous combustion characteristics of new types of coals in advance so as to prevent them from causing fires at coal yards.

It was against this background that Kobe Steel has developed a simulation technology for predicting the heat generation behavior inside a coal pile, taking into account internal factors such as the low-temperature oxidation of coal and external factors such as piling conditions and the outer environment, so as to prevent fires from occurring when storing a new type of coal, including sub-bituminous coal, that has not been used before.

## 1. Simulation model outline

A heat-generation simulation of a coal pile (hereinafter "pile simulation") has been designed to accurately reproduce the heat generation behavior inside piles. The following three behaviors were studied in detail and were modeled:

- i) the behavior of air flowing inside the pile,
- ii) the low-temperature oxidation behavior of coal inside the pile, and
- iii) the evaporation and adsorption/desorption behaviors of moisture in the coal.

These models were incorporated into the software for general-purpose thermal fluid analysis (ANSYS Fluent), which makes it possible to perform unsteady analysis taking into account the heat transfer, flow and reaction in a large-scale pile. As a result, the heat generation characteristics of various coals during storage can now be predicted by simply obtaining their physical properties from small-scale tests. This eliminates the need for measuring the temperatures of large test piles.

### 1.1 Air flow behavior inside piles

In a pile, air flows by the natural convection associated with heat generation. Roughly speaking, the air flow is caused by warmed air rising up inside the pile and escaping outside, while fresh air is being supplied from outside. A pile is an accumulation of coal granules having a size distribution. Thus,

in order to reproduce the air flow, the pressure drop inside the pile must be assessed and the flow conditions of the air must be determined. In addition, a pile consists of coal granules with a wide size distribution, resulting in different degrees of breathability, depending on the location within the pile. For example, the breathability is increased at the foot of a pile, because, when coal is piled by a stacker, coal granules with larger sizes tend to roll and to be segregated at the foot.

In order to evaluate the air flow distribution inside a pile, the granule size distributions were measured at various locations within a pile and the pressure drop for each granule size distribution was determined. **Fig. 1** shows the outline of a 1.5m laboratory pile simulating a stacking process. As shown in this figure, the test includes piling coal by discharging it from a container bag above the piling spot and collecting coal granules from areas spaced at a height interval of 0.5m. The coal granules thus collected were measured to determine their granule size distribution and coefficient of air flow resistance, as described later. The air flow resistance coefficient is used as a measure of breathability. This figure also includes average granule sizes (50% of integrated value) in different areas. Area 1 corresponds to the foot of the pile and shows an average granule size of 29.8mm, indicating that granules larger than others by one digit tend to accumulate there.

Next, an apparatus for measuring pressure drop, as shown in **Fig. 2**, was used to determine the relationship between the flow velocity and pressure drop in each area. This apparatus comprises a column to be packed with granules of coal, an air supply, a flow meter and a manometer for measuring the differential pressure of the packed column. **Fig. 3** depicts the relationships between the flow rate and pressure drop in areas 1 to 3. These areas correspond to the surface layer of the pile. This figure shows that, regardless of the area, a linear relationship as expressed by Equation (1) is established between the flow rate ( $u$ ) and pressure

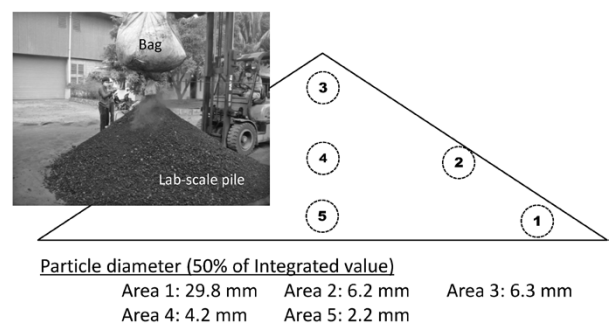


Fig. 1 Piling test

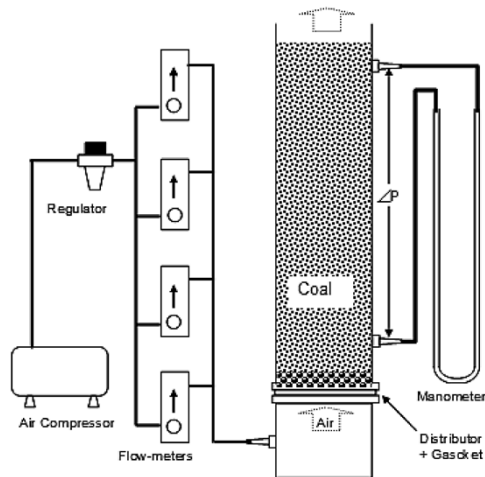


Fig. 2 Schematics of experimental apparatus for pressure drop

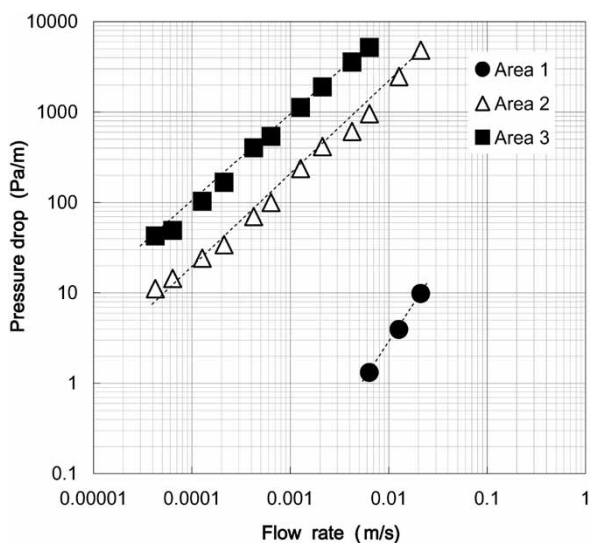


Fig. 3 Relationship between pressure drop and flow rate

drop ( $\Delta P$ ):

$$\Delta P/L = k \cdot u \quad \dots \dots \dots (1)$$

wherein  $L$  is the height of the packed layer, while  $k$  is the slope of Equation (1) and represents the air flow resistance coefficient ( $\text{Pa} \cdot \text{s}/\text{m}^2$ ). In this simulation, each pile is provided with a distribution of air flow resistance coefficient,  $k$ , so that the pressure drop can be determined and the behavior of the air flow inside the pile can be expressed. Considered by area, the air flow resistance coefficient becomes smaller at the foot (Area 1) of the pile, the area where larger granules tend to accumulate. For a conical shaped pile, the air flow resistance coefficient is higher in the areas deeper inside the pile and in the areas closer to the top.

## 1.2 Low-temperature oxidation behavior of coal inside pile

It is generally understood that, when coal is

oxidized at a low temperature, the adsorption of oxygen leads to the production of peroxides first, and these peroxides decompose into  $\text{CO}$ ,  $\text{CO}_2$  and  $\text{H}_2\text{O}$  in the end. It is known that, as the integrated amount of oxygen adsorbed on the coal increases, the number of adsorption sites decreases, lowering the rate of adsorption. This means that, in a pile, the heat generating reaction proceeds by consuming oxygen in the air and, as time passes, the activity of this reaction decreases, slowing down the heat generation.

As described above, the heat is considered to be generated by the progress of a low-temperature oxidation reaction. In this simulation, Equation (2) is used to determine the heat-generation rate  $Q$  ( $\text{kJ}/\text{m}^3/\text{s}$ ) of coal:

$$Q = \Delta H (1 - \varepsilon) \rho \text{OCR} \quad \dots \dots \dots (2)$$

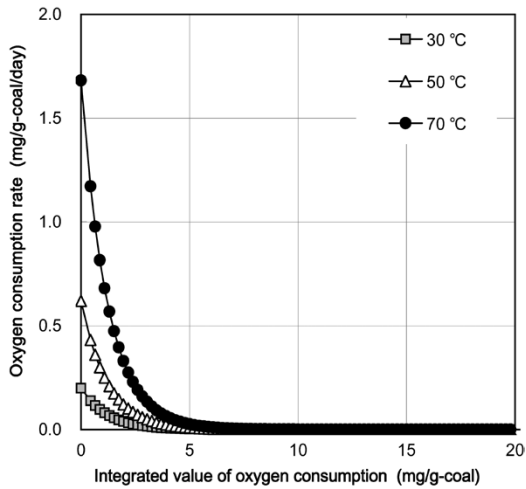
wherein  $\Delta H$  is the heat of oxidation reaction ( $\text{kJ}/\text{kg-O}_2$ ),  $\varepsilon$  is the void ratio inside the pile and  $\rho$  is the solid density ( $\text{kg}/\text{m}^3$ ). An important factor in determining the heat generation rate is the oxygen consumption rate ( $\text{OCR}$ ) expressed in  $\text{mg-O}_2/\text{g-coal}/\text{day}$ . The  $\text{OCR}$  is a value unique to each coal and, as shown by Equation (2), a larger  $\text{OCR}$  indicates that more heat is generated in the pile. Furthermore, the  $\text{OCR}$  depends on the temperature and oxygen concentration. Thus, it is expressed by Equation (3) in this simulation.

$$\text{OCR} = \text{OCR}_0 \text{EXP}\{-\Delta E/R(1/T - 1/T_0)\}[\text{O}_2]^n \quad \dots \dots (3)$$

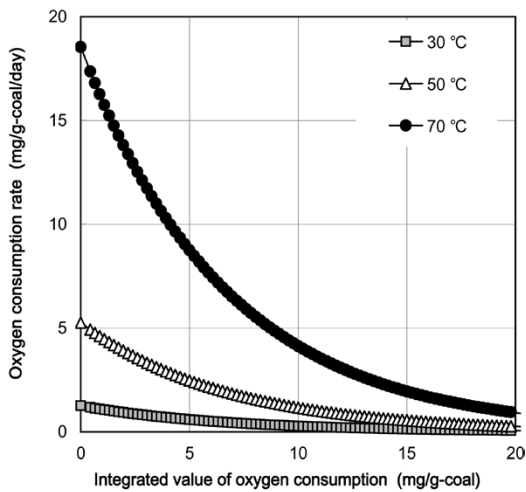
wherein  $\text{OCR}_0$  is a value ( $\text{mg-O}_2/\text{g-coal}/\text{d}$ ) measured at  $303\text{K}$  ( $30^\circ\text{C}$ ) with  $21\%-\text{O}_2$  (standard conditions),  $\Delta E$  is the activation energy ( $\text{kJ}/\text{mol}$ ),  $[\text{O}_2]$  is the oxygen concentration ratio (= "oxygen concentration in the pile" / "oxygen concentration under the standard conditions"),  $n$  is the order of reaction (-), and  $T$  and  $T_0$  are the temperature (K) inside the pile and the temperature (K) under standard conditions, respectively. Here, the  $\text{OCR}_0$  decreases with the increase in the integrated amount of oxygen consumption and is expressed as a function of the integrated amount of consumption.

The determination  $\text{OCR}_0$  involves putting coal and dry air (standard condition) in an airtight container and measuring the temporal change in oxygen concentration. This method was used to measure the relationship between the  $\text{OCR}$  and integrated oxygen consumption for bituminous coal from Australia (Coal A), as well as for sub-bituminous coal from Indonesia (Coal B). The results are shown in Fig. 4. As is evident from this figure, Coal B, sub-bituminous coal, has an  $\text{OCR}$  higher than that of the bituminous coal. The results also confirm that the  $\text{OCR}$  increases exponentially with increasing temperature. It should be noted that both types of coal show decreased reaction activity and





(a) Coal A (Bituminous Coal)



(b) Coal B (Sub-bituminous Coal)

Fig. 4 Oxygen consumption rate

a smaller OCR as the integrated value of oxygen consumption increases.

On the basis of the above, the OCR was measured for individual types of coals and was reflected in the simulation as a function, using Equation (3), of the integrated amount of oxygen consumption, temperature and oxygen concentration.

### 1.3 Evaporation, adsorption and desorption of moisture in coal

The evaporation, adsorption and desorption of moisture in coal are important in determining temperature behaviors inside a pile. This is because the moisture contained in coal evaporates, causing the latent heat of evaporation to cancel out the heat of low-temperature oxidation, which lowers the temperature inside the pile. The moisture contained in coal may be classified into two types: namely, (i) adsorption moisture existing in the pores of the coal, and (ii) adhering moisture caused by rainfall, the

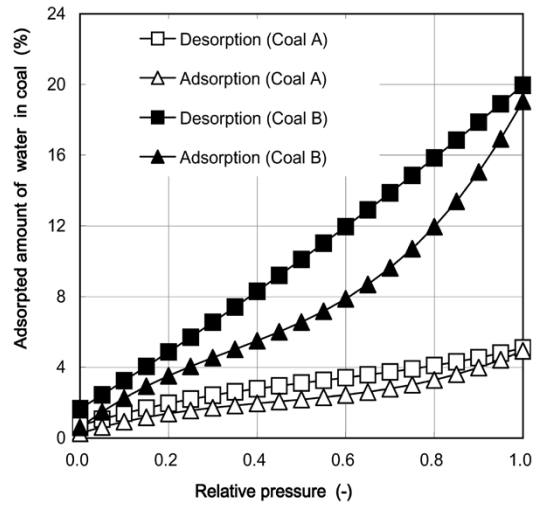


Fig. 5 Water adsorption/desorption isotherms

sprinkling of water, etc. Adsorption moisture is less prone to evaporate than is adhering moisture, and the amount of evaporation is determined from the relationship between the relative humidity and the amount of adsorption moisture.

Fig. 5 shows the adsorption/desorption isotherms of water. These isotherms were obtained by putting coal and water vapor in a container with a variable pressure and by changing the pressure under isothermal conditions. These graphs represent values actually measured for bituminous coal (Coal A) and sub-bituminous coal (Coal B) under the condition of 40°C (313 K). Under a given relative pressure, Coal B exhibits an increased amount of water adsorption, compared with Coal A. This is because the sub-bituminous coal has a larger specific surface area than bituminous coal; the coalification proceeds while changing the carbon structure and the chemical bonds of the coal. For a given humidity condition, only the moisture in the condition above the adsorption/desorption curve can evaporate, and this evaporation continues until this moisture is dissipated. When the relative pressure is constant, the moisture in the coal stays on or above the adsorption/desorption curve; meaning it does not decrease. In a condition where the heat generation is dominant, the temperature of the pile increases, decreasing the relative humidity. As a result, the evaporation continues, decreasing the moisture content of the coal. When the moisture in the coal is completely dried, no factor that can suppress heat generation exists any longer, and, as a result, the temperature in the pile rises faster.

On the basis of the above, the adsorption isotherms of water were measured for each type of coal. The evaporation behaviors of moisture in coal were more realistically modeled and simulated in this way.

## 2. Measuring internal temperatures of test pile

In order to improve and verify the analysis accuracy, two test piles with different heights (15m and 4m) were prepared and their internal temperatures were measured (Fig. 6). The larger pile (15m pile) was cone-shaped and had a base angle of approximately 37°, a height of 15m and a bottom diameter of 40m. Measurements were performed at the 15 points shown in Fig. 6-(a) and the thermometers were spaced at intervals of 2.2m to 2.8m. The smaller pile (4m laboratory pile), on the other hand, was a partial cut-out of a cone-shaped pile and had the shape of a triangular prism with a height of 3.8m, width of 0.8m and bottom length of approximately 5.9m. Both of the triangle-shaped lateral faces were thermally insulated. Measurements were performed at the 21 points shown in Fig. 6-(b) at the center of the 0.8m width and the thermometers were spaced at intervals of approximately 0.5m to 0.7m.

The sub-bituminous coal, Coal B, was formed into the above two test piles and temperature measurements were conducted on each one for about a month. Fig. 7 shows the results of these temperature measurements at typical points in the piles. As shown in Fig. 7(a), in the 15m large pile, the temperature rose remarkably at points #4, 5,

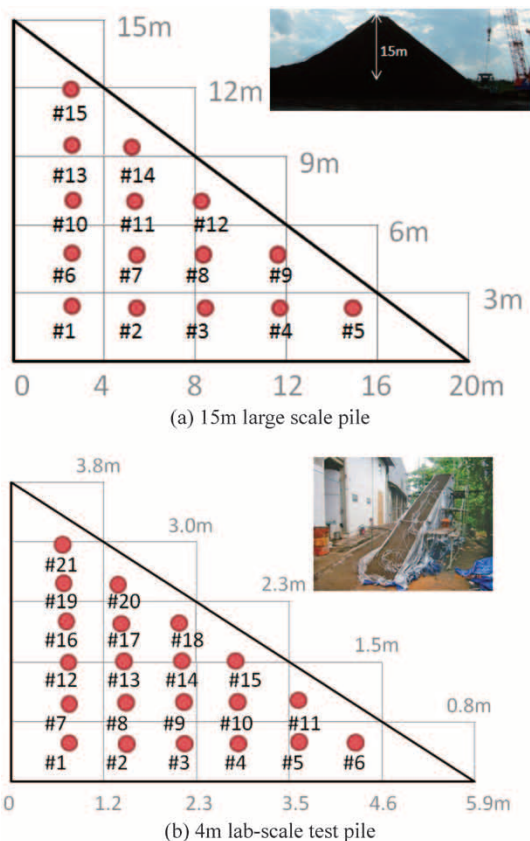
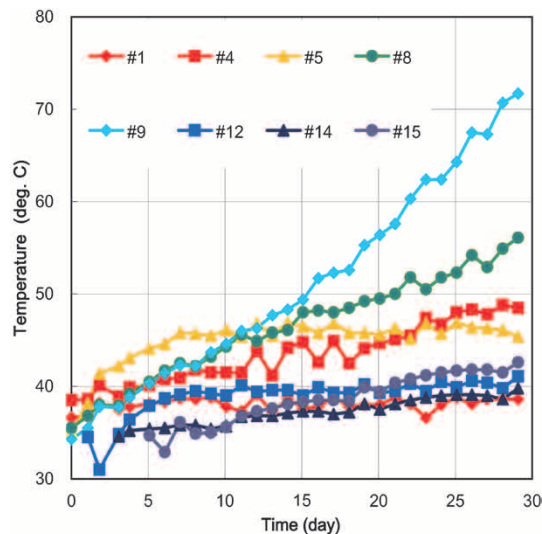
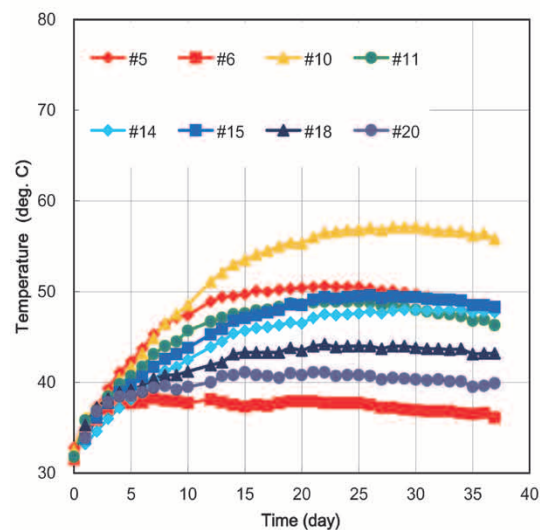


Fig. 6 Measurement points of temperature inside pile



(a) 15m large scale pile for Coal B



(b) 4m lab-scale test pile for Coal B

Fig. 7 Measured results of temporal temperature change inside pile

8 and 9, each located at the foot of the pile. The heat is generated by oxidation, and oxygen must be supplied into the pile for it to occur. The remarkable temperature rise at the above points could thus be attributable to the fact that coal with a larger granule size tends to accumulate at the foot of the pile, as in the case of the 1.5m laboratory pile described in Section 1.1, making the breathability at the foot higher than at other points, enabling the supply of oxygen required for the heat generation. At the #9 position, in particular, the pile temperature rose at a rate of 1.2°C/d. This indicates that the temperature would reach 90°C in 50 days. Once the pile temperature reaches 90°C, the temperature begins to rise abruptly. Thus ignition is presumed to occur at this location.

The 4m laboratory pile, shown in Fig. 7(b), also showed a remarkable temperature rise at points #5, #10, #11, #14 and #15, each at the foot of the

pile as in the case of the larger pile. The maximum temperature reached in the case of the 4m laboratory pile, however, was lower than that reached by the larger pile. This is due to the greater amount of heat dissipated from the lateral faces of the triangular prism.

### 3. Prediction of heat generation based on pile simulation

The newly developed pile simulation was used to reproduce the heat generation behaviors in the two test piles (15m and 4m). **Table 1** shows the physical properties of the sub-bituminous coal from Indonesia (Coal B) used for the test. The physical properties of the bituminous coal from Australia (Coal A) are also shown for comparison. The O/C ratios—an index for spontaneous combustibility—are 0.05 and 0.14 respectively, indicating a higher spontaneous combustibility for Coal B. The major differences between Coal A and Coal B lie in the moisture content, specific heat, heat of oxidation reaction and activation energy. Coal B, containing a greater amount of moisture, is characterized by a higher specific heat and a smaller heat of oxidation reaction.

The initial conditions of the temperature and humidity for this simulation were taken from an average temperature and relative humidity corresponding to those of the atmosphere in Indonesia, where the temperature measurement experiments were carried out (**Table 2**). As for heat transfer behaviors inside a pile, the heat generation by oxidation reaction was estimated on the basis of

thermal conduction, while the heat extraction from the pile by air flow was estimated on the basis of convection heat transfer.

The heat generated by the low-temperature oxidation reaction of coal is transferred inside the pile by thermal conduction in accordance with the effective thermal conductivity  $\lambda$  (W/m/K) defined by Equation (4). Here,  $\varepsilon$  represents the ratio of voids inside the pile,  $\lambda_p$  represents the thermal conductivity of coal and  $\lambda_g$  represents the thermal conductivity of air.

$$\lambda = (1 - \varepsilon) \lambda_p + \varepsilon \lambda_g \dots\dots\dots (4)$$

The heat extraction from the pile, on the other hand, was assumed to be caused by natural convection (10W/m<sup>2</sup>/K), since the velocity of the air flowing inside the pile is low. The dissipation of heat from the bottom of the pile to the ground was considered to take place by thermal conduction (10W/m/K). For the 4m laboratory pile, the amount of heat dissipated to the atmosphere from the triangular lateral face with insulation was assumed to be 0.5W/m<sup>2</sup>/K. When measured, the amount of heat dissipated from the triangular lateral face of the 4m laboratory pile was, in fact, found to be approximately 0.5W/m<sup>2</sup>/K to 0.6W/m<sup>2</sup>/K.

The results of the simulation are shown in **Fig. 8** and **Fig. 9**. The objects of analysis were the 15m large piles of Coal A (**Fig. 8**, left) and Coal B (**Fig. 8**, right), and the 4m laboratory pile of Coal B (**Fig. 9**). The simulated data was compared with measured data, which proved that this pile simulation represents a good reproduction of the hot spots and the temporal change in temperature, regardless of the heights and shapes of the piles. In the case of the 15m large pile, the simulation has confirmed that the temperature rises significantly at the foot of the pile and as far as half-way up, in the same way as in the actually measured data, reaching approximately 70°C to 75°C after 30 days. The simulation has also been confirmed to be a good reproduction of the temperature that was reached, lowered by the dissipation from the triangular lateral face of a pile, e.g., one similar to the 4m laboratory pile, even if it has a different shape.

Comparing the 15m large piles of Coal A and Coal B, the simulation results show that Coal A reaches its maximum temperature of 50°C after 30 days, while Coal B exhibits areas whose temperature exceeds 60°C even after 15 days and reaches the proximity of 75°C after 30 days. This is considered to be due to the high OCR of Coal B, sub-bituminous coal, which gives rise to a low-temperature oxidation reaction. In the case of Coal A, on the other hand, the temperature was found to rise in wider areas than in Coal B. This is considered to be attributable to the

**Table 1** Coal properties

	Coal A, Australian bituminous coal	Coal B, Indonesian sub-bituminous coal
$\rho$ Density [kg/m <sup>3</sup> ]	1,150	1,100
$C_p$ Specific heat [kJ/kg/K]	1.46	2.30
$\lambda_p$ Heat conductivity [W/m/K]	0.25	0.25
$D_p$ Average diameter [mm]	5.0	5.0
$\Delta E$ Activation energy [kJ/mol]	46	58
$\Delta H$ Amount of heat generation [kJ/g-O <sub>2</sub> ]	10.73	6.91
$\varepsilon$ Void ratio [-]	0.19	0.19
W Moisture [%]	11	27
O/C O/C ratio	0.05	0.14

**Table 2** Initial condition of coal pile and atmosphere

	Coal stock pile	Atmosphere
Initial temperature [deg. C]	30	30
Initial relative humidity [%]	88	70



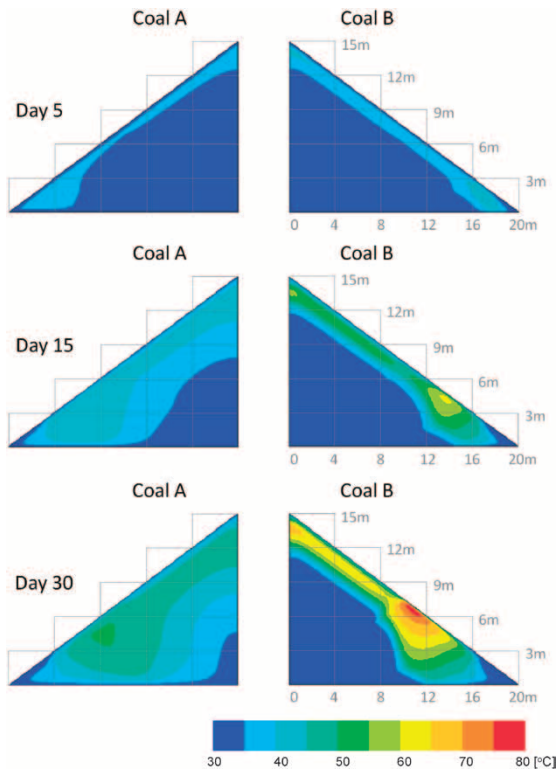


Fig. 8 Analysis results for temporal temperature change in 15m large piles of coal A and coal B

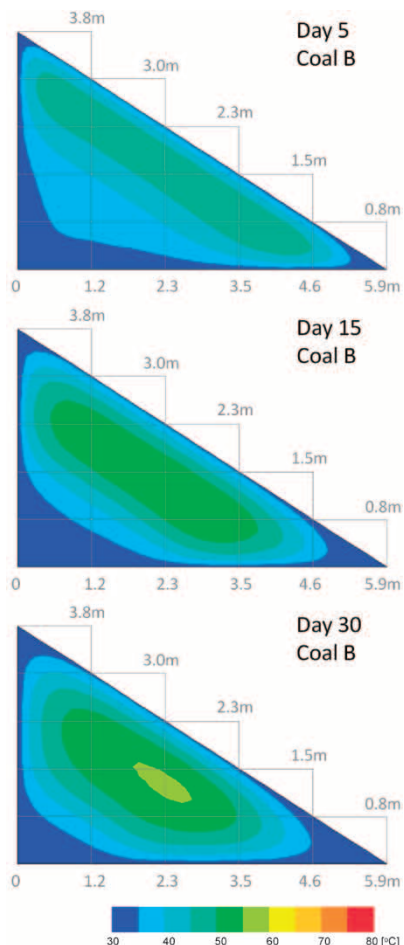


Fig. 9 Analysis results for temporal temperature change in 4m laboratory pile of Coal B

fact that Coal A has a lower specific heat and higher heat of oxidation reaction compared with coal B, which has a high moisture content (Table 1).

As described above, it was confirmed that the heat generation behavior during the storage of a new type of coal that has not been used before can be predicted without conducting trials on large-scale test piles. This can be achieved by laboratory tests to obtain data on the internal factors, including the low-temperature oxidation of the coal and the adsorption and desorption characteristics of water, and on the external factors, including the filling state of the pile and outer environment.

## Conclusions

A heat generation simulation has been developed for piles of coal. In order to accurately reproduce the heat generation behaviors inside the piles, this simulation consists of unsteady analysis that links the heat transfer, flow and reaction, taking into consideration i) the flow behavior of air inside the pile, ii) the low-temperature oxidation behavior of coal inside the pile, and iii) the evaporation, adsorption and desorption behaviors of moisture in the coal. This simulation makes it possible to predict the heat generation behavior when storing a new type of coal that has not been used before.

In other words, the simulation allows predicting the spontaneous combustion of various new types of coal during storage by simply obtaining their physical properties through small-scale testing without conducting large-scale measurements involving several thousand tonnes of coal.

This technique is to be used to predict heat generation behavior during the storage of various new types of coals and to establish databases for appropriate delivery intervals.

## References

- 1) Japan Oil, Gas and Metals National Corporation (JOGMEC). Research report on the development and advancement of coal from overseas. March. 2013.
- 2) H. Yamamoto et al. Journal of the Japan Institute of Energy. 2007, 86 ( 2 ), p.119-129.
- 3) H. Asaga. The thermal and nuclear power. 2006, 57 ( 6 ), p.426-430.
- 4) T. Muratani et al. Conference of coal science (38). 2001, p.279-282.
- 5) T. Ono et al. The thermal and nuclear power 33 ( 3 ). 1982, p.247-261.
- 6) T. Ono et al. The thermal and nuclear power 33 ( 4 ). 1982, p.379-386.

Note) The names of companies and products cited herein may be trademarks or the registered trademarks of their respective owners.



# Mine-mouth Power Generation System Based on Upgraded Brown Coal (UBC®)

Takeo KASHIWAGI \*1, Hiromichi ISHINO \*2, Takashi TAKAGI \*3, Ken HIROSE \*4

\*1 Coal Project Section, Iron Unit Div., Engineering Business

\*2 Coal Project Section, Iron Unit Div., Engineering Business (currently Kobelco Eco-Solutions Co., Ltd.)

\*3 Coal Project Section, Iron Unit Div., Engineering Business (currently Shinko Engineering & Maintenance Co., Ltd.)

\*4 Coal Project Section, Iron Unit Div., Engineering Business (currently International Operations Dept., Iron Unit Div., Engineering Business)

*Currently, the use of lignite (also referred to as "brown coal") is limited to mine-mouth power generation. The high moisture content in lignite causes its power-generating efficiency to be considerably lower than that achieved by bituminous coal. Kobe Steel has developed a process for producing Upgraded Brown Coal (UBC®) by applying a unique slurry dewatering technology. A study has been conducted using the UBC made from Indian lignite to verify its applicability in improving the efficiency of mine-mouth power generation. The results confirmed that UBC-based power generation is superior to the existing lignite-fired power generation.*

## Introduction

Among the various coals, lignite has a less complete level of coalification, as well as much retarded dewatering and decarboxylation, compared with high-grade coals such as bituminous coal. It contains as much as 30% to 65% of moisture and 20% to 25% of oxygen. Thus, when compared with other coals with the same mass, lignite, containing a large amount of moisture, has a substantially smaller proportion of organic matter (to be converted into heat) and a lower calorific value. When dried, lignite becomes prone to spontaneous combustion, making its handling difficult. For these reasons, for over 20 years the production of lignite has plateaued at a level of approximately 900 million tonnes, with almost no increase in consumption, despite its plentiful reserves (approximately 200 billion tonnes, which accounts for 23% of the total proven reserves of coal).

Lignite is relatively young in geological age and is generally deposited near the earth's surface. This decreases the stripping ratio and enables open-pit mining, which is advantageous because the coal can be mined more economically. In addition, most lignite contains low sulfur and low ash. It is attracting increased attention due to its higher environmental suitability compared with bituminous coal and sub-bituminous coal.

In light of these aspects, several countries are eager to develop technologies for upgrading brown coal (lignite) to increase its calorific value and stability so as to exploit it more effectively.

Kobe Steel developed a process for producing

Upgraded Brown Coal (hereinafter referred to as "UBC®" <sup>note</sup>). This process features a dewatering method for efficiently removing the large amount of moisture contained in lignite, thus increasing its calorific value.

The UBC process has many applications; this paper focuses on mine-mouth power generation based on UBC powder.

## 1. Development of UBC process

### 1.1 Development history

Kobe Steel had worked on the development of the liquefaction process for lignite since the 1970s and had cooperated with several other Japanese companies to conduct a pilot project in Victoria, Australia, under a consignment arrangement of the New Energy and Industrial Technology Development Organization (hereinafter NEDO) since 1981. The extensive knowledge on lignite acquired through this project led Kobe Steel to develop the UBC process. After the liquefaction project ended, the company started working on the development of the UBC process and saw its completion in a large-scale demonstration project<sup>1)</sup> conducted in Indonesia from 2006 to 2011.

The following outlines the progress achieved thanks to this project.

### 1.2 Plant construction and operation

In the early 1990s, a bench-scale plant (product-base capacity; 0.1t/d) was built in the Kakogawa Works of Kobe Steel, in which the technical advantage of UBC was confirmed. This was followed by projects involving a pilot plant (product-base capacity; 3t/d) and a demonstration plant (product-base capacity; 600t/d), both constructed in Indonesia, one of the countries producing lignite. These projects have verified the technical effectiveness and economic feasibility of the UBC process. The demonstration test in Indonesia was subsidized by the Japan Coal Energy Center (JCOAL), the Ministry of Economy, Trade and Industry (METI),

<sup>note</sup>) UBC is a registered trademark of Kobe Steel.

under the cooperation of an Indonesian government organization, the Mineral & Coal Technology Research & Development Center (tekMIRA). **Table 1** shows outlines of the pilot plant and demonstration plant. A general view of the demonstration plant is shown in **Fig. 1**.

### 1.3 UBC process outline

**Fig. 2** outlines the flow of the UBC process. Raw material lignite is pulverized into pieces of 5mm or smaller using a mill (Coal Mill). These are mixed and agitated with light oil, used as a heating medium, to form slurry. The slurry is heated in an evaporator so as to evaporate moisture in the lignite. This process enables the efficient dewatering of lignite with high moisture content under relatively mild process

conditions of approximately 140°C to 150°C at 3atm. The moisture steam evaporated from the lignite is separated from the slurry by a gas-liquid separator (Flash Drum). The by-product steam is compressed by a compressor (Recycle Vapor Compressor) into high-temperature steam and is reused as the heat source for the evaporator. Thus the latent heat is effectively exploited and the thermal efficiency is improved. The coal/light-oil slurry separated by the gas-liquid separator is collected in a centrifuge (Decanter) and is separated into light-oil and coal cake. The light oil is reused as the heating-medium oil for slurring. The coal cake is transferred to a dryer (Dryer) where the light oil, still remaining in the coal cakes, is collected further. Circulating gas (Recycle Gas) is supplied inside the dryer to increase the oil collection rate of the dryer and to

**Table 1** Outline of pilot plant and demonstration plant

	Location	Capacity (t/d) (product basis)	Duration (construction~ operation)	Purposes
Pilot plant	Indonesia (Palimanan, Jawa)	3	2001~2004	Confirmation of technical viability
Demonstration plant	Indonesia (Satui, Kalimantan)	600	2006~2011	Collection of data for design, construction and operation of commercial scale plant



**Fig. 1** Outside view of 600t/d demonstration plant

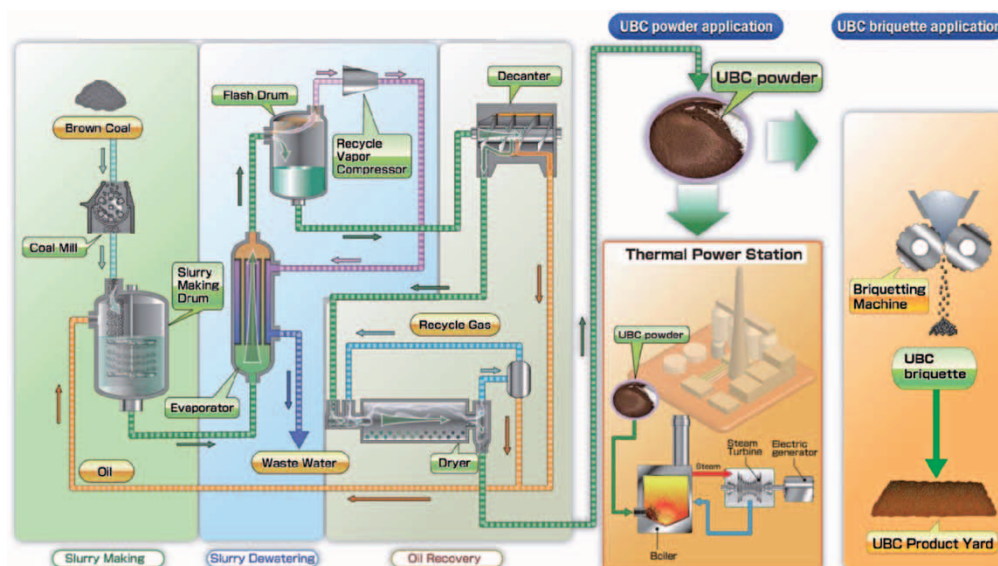


**Fig. 2** Process flow of UBC

promote the drying out of the light oil. Then the circulating gas, containing oil vapor, is cooled and condensed so that the light oil can be collected and reused. This produces UBC powder with its residual oil decreased to 0.5% and its moisture to zero.

As a process for dewatering lignite with high moisture content, the UBC process has the following additional features:

(1) High energy efficiency

Compared with other upgrading processes, the process of dewatering slurry in oil operates under milder conditions of temperature and pressure during dewatering. The process allows the vaporizer to run with a higher heat transfer coefficient. High energy efficiency is achieved as a result of compressing the steam generated from dewatering, reusing it as a heat source and collecting the latent heat of the steam.

(2) Enabling the use of inexpensive apparatuses

The process enables the use of inexpensive, general-purpose apparatuses such as a heat exchanger, centrifugal pump and gas-liquid separator.

(3) Low environmental burden

The high energy efficiency results in lower CO<sub>2</sub> emissions than are achieved with other upgrading processes. Involving no chemical reaction, the UBC process generates no effluent contaminated by noxious organic substances, which reduces the burden on waste water treatment.

There are two ways of using the product. One is briquetting the UBC powder with a compacting machine as it exits the dryer. This method is applied to product that must be carried over a long distance in a stable manner. Another way is to directly charge the UBC powder into an adjacent power plant. This method maximizes the UBC process feature of achieving zero moisture and enables highly efficient power generation. The following focuses on this application.

## 2. Limited application of lignite at present

As described above, there are proven reserve deposits of lignite amounting to approximately 200 billion tonnes. Taken in order by region, from larger to smaller, there are deposits in Europe, Oceania, Asia and North America, while there is nothing to indicate the presence of lignite in Africa, the Middle East, and Central and South America. Currently, lignite is only utilized in very limited regions and countries, and in the least efficient manner.

Transporting lignite to a remote area for

consumption suffers from low efficiency due to its high moisture content. In addition, there is a risk of spontaneous combustion during transportation. Therefore, lignite has so far only been used as-is for lignite-fired power generation at mining places. Lignite-fired power generation requires special boilers that are expensive to build. In addition, the low calorific value of fuel lignite decreases its power generation efficiency. As a result, the generated power is costly.

### 2.1 Lignite-fired power generation systems currently in operation

Lignite-fired power systems have been in operation in lignite producing countries such as Australia, Germany, Poland and India. In general practice, the moisture in lignite is removed by, for example, a flash mill dryer before the coal is burnt in a boiler. A lignite-fired boiler is typically a tower boiler, the flow of which is outlined in Fig. 3. In this system, flue gas at a temperature of approximately 900°C is extracted from the boiler top, where the boiler temperature reaches its maximum, and is introduced into a coal mill. The coal particles pulverized in this mill are transferred into a dryer duct by the flue gas. When passing through the dryer duct, the moisture contained in the lignite is heated and evaporated rapidly within 2 to 10 seconds, producing dry particles of lignite. The flue gas, whose heat is consumed in evaporating the moisture, is cooled rapidly and returned to the boiler along with the moisture evaporated from the coal.

In the end, the water vapor in the flue gas is dissipated into the atmosphere without its latent heat being collected. This significant heat loss causes the power generation efficiency at the sending end

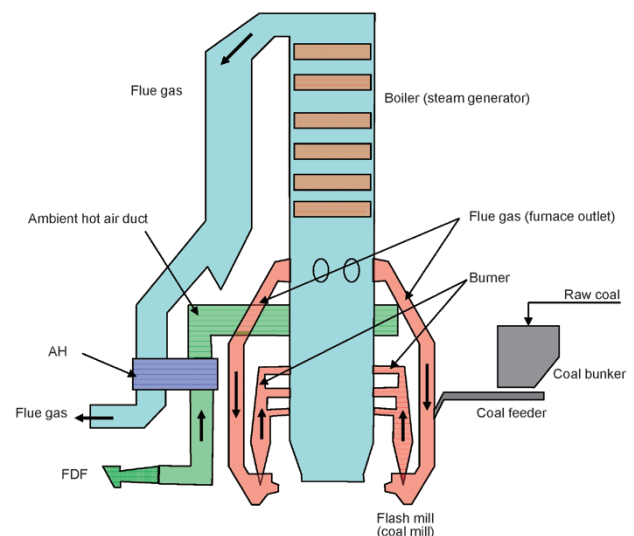


Fig. 3 Schematic flow of lignite-fired boiler (tower boiler)



to be as low as approximately from 20+% to 30%. The high moisture content also decreases the heat density within the boiler. This makes the boiler larger in size and more expensive to build in comparison with the bituminous-coal-fired boiler generally used.

The UBC process developed by Kobe Steel employs a pretreatment based on an efficient dewatering technique, which enables the upgrading of lignite with a high moisture content to coal (UBC powder) with zero moisture content and a high calorific value. This UBC powder is supplied to a high-efficiency power generation system, which significantly decreases the cost of power generation and CO<sub>2</sub> emissions, compared with conventional lignite-fired power generation systems.

Kobe Steel conducted research entitled the "Low CO<sub>2</sub> Emission Type Power Generation Project based on Upgraded Brown Coal (UBC) in India,"<sup>2)</sup> which was commissioned by NEDO's 2012 "High-efficiency Clean Coal Technology". As described in Section 3, this commissioned research has clarified the advantages of mine-mouth power generation based on UBC.

## 2.2 Lignite-fired power generation in India

The Indian lignite used for the NEDO research project has the following characteristics (in average values): moisture 52%, ash 4.5%, volatile matter 25%, fixed carbon 18.6%, and a calorific value of 2,830 kcal/kg (higher heating value: HHV). The lignite-fired power generation plant used as a conventional

reference comprises a sub-critical tower boiler with an output of 210MW and has a sending end efficiency of 29.15% (HHV basis).

This lignite is upgraded by the UBC process, and the product UBC powder is charged into a state-of-the-art high-efficiency power plant with an output of 1,000MW to study the comparative advantage. An overview follows:

## 3. Mine-mouth power generation based on UBC

### 3.1 Production and combustion tests of UBC

The applicability of Indian lignite to the UBC process was studied by laboratory tests performed on samples of the lignite, as well as by production tests conducted at the pilot plant located in Indonesia. Ten tonnes of UBC powder produced by the pilot plant were sent to a boiler manufacturer in Japan where combustion tests were carried out.

The results confirmed that the Indian lignite can be upgraded by the UBC process without any problems and that the UBC powder has sufficiently high combustibility to be applied to an ultra-super critical boiler without causing any problems. Another confirmed advantage was the fact that the ash contains much less unburned matter.

### 3.2 Incorporation of UBC plant into power generation plant

Fig. 4 outlines the flow of a power plant incorporating a UBC plant. The UBC powder

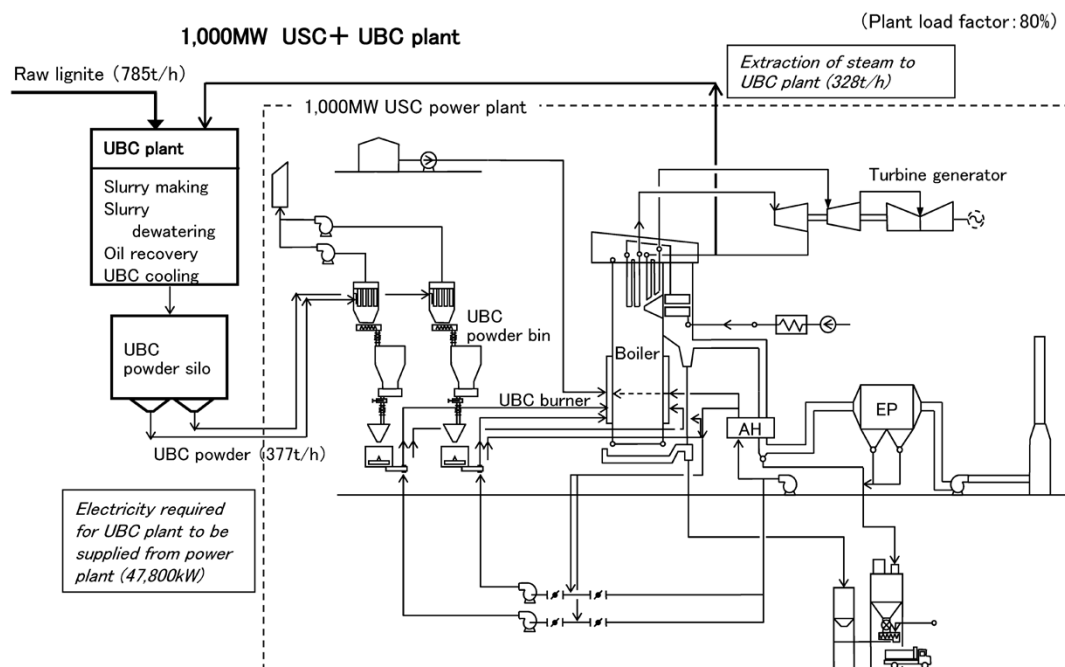


Fig. 4 Schematic flow of UBC based power plant



produced by the UBC plant is cooled to approximately 60°C, stored in silos and, from there, charged as-is into a boiler through UBC powder supply bins. This eliminates the need for a coal pulverizing mill to be installed on the side of the power plant, which would otherwise be required. The UBC plant requires steam and electricity for its energy. The steam is partially extracted from the power generation plant, while electricity is supplied as a part of the auxiliary power. This optimizes the energy efficiency of the integrated system as a whole.

### 3.3 Improvement of power generation efficiency

The 52% moisture contained in the Indian lignite is decreased to zero by the UBC process, which increases the calorific value from 2,830 kcal/kg (HHV) to 5,900kcal/kg (HHV), enabling the introduction of an ultra-super-critical power generation plant.

The power generation efficiency is compared with that of conventional lignite-fired power generation as shown in **Table 2**. In Case 1, where a UBC plant is combined with a sub-critical power generation plant (i.e., a power generating

plant operating under sub-critical conditions, as in the case of a conventional power plant), a power generation efficiency of 32.60% is achieved, with an improvement rate of 11.8% compared with the conventional plant. In Case 2, where a UBC plant is combined with an ultra-super-critical power plant (the major subject of this study), the power generation efficiency reaches 34.45%, with an improvement rate of 18.2%, in comparison with the conventional type. In both Case 1 and Case 2, the steam and power required to run the UBC plant are supplied from the respective power generation plant in the downstream.

In Case 3, which assumes that the UBC product (powder) is charged into an ultra-super-critical power generator and the steam and power required to operate the UBC plant are supplied from other sources, the power generation efficiency becomes 40.63%, with an improvement rate—in comparison with the conventional plant—of 39.4%.

### 3.4 Reduction of lignite consumption and CO<sub>2</sub> emissions

**Table 3** shows the reduction in lignite consumption and CO<sub>2</sub> emissions, assuming 1,000

**Table 2** Effect of improving power generation efficiency

		Power generation efficiency (%) (sending end, HHV basis)	Improvement from conventional (%)	Remarks
<b>Conventional Power Generation</b>				
Lignite-fired Sub-Critical Plant		29.15	NA	Data from operating Plant
<b>UBC based Power Generation</b>				
1	Integrated UBC-fired sub-critical plant	32.60	11.8	Energy used for UBC plant is deducted
2	Integrated UBC-fired ultra super critical plant	34.45 (40.90:LHV basis)	18.2	Energy used for UBC plant is deducted
3	Non Integrated UBC-fired ultra super critical plant	40.63 (42.70:LHV basis)	39.4	Energy used for UBC plant is not deducted

\* Lignite:total moisture 52%, calorific value 2,830kcal/kg (HHV)  
 UBC powder:total moisture 0%, calorific value 5,900kcal/kg (HHV)

**Table 3** Reduction of lignite consumption and CO<sub>2</sub> emissions

	Study results				Remarks
	Power output	UBC production (Mt/y)	Lignite consumption (Mt/y)	CO <sub>2</sub> emission (Mt/y)	
①UBC-fired ultra super critical plant	1,000 MW (generating end) 891 MW (sending end)	2.64	5.50	5.69	
②Conventional lignite-fired sub-critical plant	957 MW (generating end) 891 MW (sending end)	—	6.51	6.73	•Existing facility is 210MW sub-critical. •Sending-end output is adjusted to the above ①.
Reduction of lignite consumption and CO <sub>2</sub> emission	—	—	1.01 (②-①) (approx. 16% reduction)	1.04 (②-①) (approx. 16% reduction)	

<Premises of the study>· Lignite : total moisture 52%, calorific value 2,830kcal/kg (HHV), carbon 28.22%  
 · Plant load factor : 80% (7,008 h/y)

MW power generation. Comparisons are made with a conventional plant. This comparison assumes that both plants have the same output at their respective sending ends. The CO<sub>2</sub> reduction is attributable to the lignite consumption being decreased (for the same amount of power generated) by improved power-generation efficiency. It is expected that the annual consumption of lignite would be reduced by approximately 1 million tonnes, and annual CO<sub>2</sub> emissions would be reduced by 1 million tonnes, compared with conventional-type power generation.

#### **4. Advantages of mine-mouth power generation system based on UBC**

Mine-mouth power generation exploiting the UBC process for pretreatment possesses advantages over lignite-fired power generation. The following is a summary of these advantages:

- (1) Realization of highly-efficient power generation:
  - Use of UBC powder with a high calorific value for the fuel. (The total moisture content of the lignite, which is higher than 50%, is reduced to 0%.)
  - Burning UBC powder with a high calorific value causes no problems in an ultra-super-critical boiler.
- (2) Decreased CO<sub>2</sub> emissions:
  - Thanks to the decreased consumption of lignite.
- (3) Low operating cost:
  - Highly efficient power generation (enabling the introduction of a highly efficient power generating system.)
- (4) Extension of mine life:
- (5) Low capital investment in power generating facilities:
  - No need for a tower boiler that would be large in scale and costly.
  - No need for a coal pulverizing machine (because UBC powder is used for the fuel.)

Other advantages include the following:

- Containing zero moisture, UBC can generate power more efficiently compared with other fuel coals of a similar grade.
- UBC powder, with its advantages of high combustibility and lower amounts of unburned constituents in its ash, can substitute for other fuel coals.

#### **Conclusions**

Despite its plentiful reserves, the use of lignite is limited. The UBC process is a process for exploiting a so-called unused resource.

As the global demand for energy continues to increase, there is a concern that the supply of high-grade coal will become depleted. Under such conditions, the effective use of lignite by the UBC process is important, as it is currently not fully used. The process enables us to improve power generation efficiency, thus reducing CO<sub>2</sub> emissions better than lignite-fired power generation (still used in certain areas), in which lignite is used as-is. This new technology is expected to prevail in countries such as India, where lignite is available in abundance.

The development of the UBC process introduced in this paper was carried out under the aid of JCOAL, METI of Japan, and the cooperation of the Coal and Mineral Technology Research and Development Centre (tekMIRA) of Indonesia. Furthermore, the study on UBC-based mine-mouth power generation was conducted as a project subsidized by NEDO. We wish to express our special gratitude to all.

#### **References**

- 1) S. Kinoshita et al. Kobe Steel Engineering Reports. 2010, Vol.60, No.1, p.71.
- 2) NEDO Progress Report, FY2012. Project Formation Research on High-efficiency Clean Coal Technology. No. 20130000000625.

---

Note) The names of companies and products cited herein may be trademarks or the registered trademarks of their respective owners.

# Energy Saving Air-Separation Plant Based on Exergy Analysis

Masaaki TANIGUCHI \*1, Hitoshi ASAOKA \*1, Toshiyuki AYUHARA \*1

\*1 Shinko Air Water Cryoplant, Ltd.

*Air-separation units (ASUs) are widely used in various industries such as steel, chemistry and electronics. They require a very large amount of energy. Therefore, their energy consumption needs to be reduced further in order to help stop global warming. Shinko Air Water Cryoplant (SAC) has been conducting collaborative research with the University of Tokyo to develop a process that can greatly reduce the power consumption. The concept of "exergy" was introduced in this research as an index for evaluating the energy efficiency of a process. As a result, a new single-column rectification process has been developed and verified as requiring approximately 30% less energy than does the conventional double-column rectification process.*

## Introduction

In 1934, Kobe Steel produced an air-separation unit for the first time in Japan. For approximately 80 years since then, the company has been contributing to the growth of the industry as a manufacturer of air-separation units. Since 2004, Shinko Air Water Cryoplant, Ltd. (hereinafter referred to as "SAC"), a joint venture with Air Water Inc., has been supplying these air-separation units.

Air-separation units are mainly used for producing the oxygen, nitrogen and argon consumed in industries such as steel, chemistry and electronics. Some of these units consume power as high as several tens of megawatts, depending on the plants. Recent concerns over global warming from CO<sub>2</sub>, etc. and soaring energy prices have significantly increased the need for further energy saving. Meanwhile, oxygen-enriched combustion technology is being adopted in the fields of steelmaking and thermal power generation. This combustion technology reduces the amount of heat lost in exhaust gas and improves the efficiency of combustion by burning with oxygen enriched air, and the demand for oxygen is expected to grow further. Thus, there is a need for an air-separation unit that can produce oxygen at low cost.

The performance of air-separation units has been improved considerably by adopting adsorbent for the front-end purification and by applying structured packing to their distilling columns.<sup>1)</sup> These air-separation units, however, can produce oxygen only at a power consumption rate as high as from 360kWh/kNm<sup>3</sup>-O<sub>2</sub> to 500kWh/kNm<sup>3</sup>-O<sub>2</sub>,

versus the theoretical minimum consumption rate of approximately 70kWh/kNm<sup>3</sup>-O<sub>2</sub>, and still leaves much room for further power reduction.<sup>2)</sup>

In an attempt to realize a process that can significantly decrease the power consumption of conventional air-separation units, SAC has conducted collaborative research with the University of Tokyo. This paper introduces a process analysis based on "exergy" as an index for evaluating energy efficiency. Exergy is an index representing the amount of energy that can be extracted as useful work under the standard conditions and is also referred to as effective energy (See Equation (1) further on in this paper).

As a result of the study based on exergy, converting the air-separation process from a double-column rectification process to a single-column rectification process and increasing the amount of thermal circulation enable a 30% power reduction in comparison with the conventional process.

## 1. Double-column rectification process

### 1.1 Conventional air-separation process (double-column rectification process)

Currently, large-scale air-separation units that separate air to produce oxygen and nitrogen adopt a process called a cryogenic separation process, in which air is liquefied, distilled (rectification) and separated into oxygen and nitrogen on the basis of the difference in their boiling points. Cryogenic separation is so called because the liquefaction of air occurs at a temperature from approximately -170°C to -190°C and the separation process is performed in a thermally-insulated cryogenic system. **Fig. 1** depicts the process flow of the cryogenic separation system generally used. Most air-separation units currently adopt a double-column rectification process, involving two rectification columns.

In a double-column rectification process, an air compressor is used to compress atmospheric air to approximately 450kPaG. The compressed air is introduced into a main heat exchanger, where most of the air is cooled to a temperature near the saturation temperature of -170°C. The saturated air is introduced into a high-pressure column (HP column) to be separated into oxygen-rich liquefied air and liquefied nitrogen. Meanwhile,

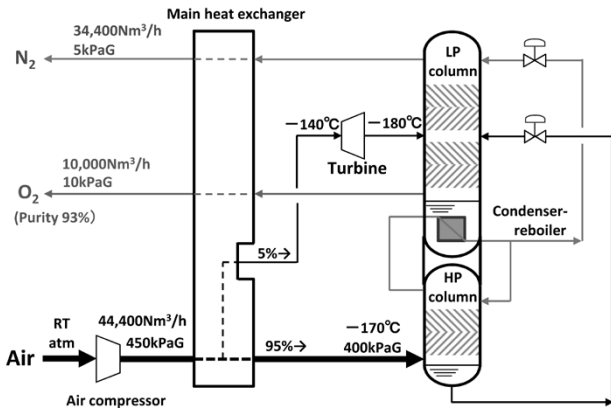


Fig. 1 Process flow for double-column rectification

the raw air partially extracted from the main heat exchanger at around  $-140^{\circ}\text{C}$  is introduced into an expansion turbine and is adiabatically expanded until it reaches a low-temperature, low-pressure condition. This generates the cold energy required to maintain the apparatus at a low temperature. Next, the liquefied air and liquefied nitrogen are supplied into the respective zones of a low pressure column (LP column) as reflux fluids and are separated into highly-pure oxygen and nitrogen. The low pressure column is provided with a heat exchanger (Condenser-reboiler) at its bottom. This heat exchanger works both as a condenser for the HP column and as the reboiler for the LP column. The oxygen and nitrogen thus separated are warmed by the heat exchange with raw material air at the main heat exchanger and collected at room temperature.

## 1.2 Exergy analysis of double-column rectification process

An exergy analysis was conducted to identify which parts in a general double-column rectification process had a large energy loss. A large exergy loss means that energy is wasted. Thus it can be said that the smaller the exergy loss, the more superior the process.

Exergy (E) is defined by Equation (1):

$$E = H - H_0 - T_0(S - S_0) = \Delta Q - T_0 \Delta S \dots\dots\dots (1)$$

$H$ : Enthalpy of the system (kJ)

$H_0$ : Standard enthalpy (kJ)

$S$ : Entropy of the system (kJ/K)

$S_0$ : Standard entropy (kJ/K)

$T_0$ : Standard temperature (K)

In order to calculate the amount of exergy loss in a heat exchanger, the latter half ( $-T_0 \times \Delta S$ ) of Equation (1) is integrated with the whole temperature range of the heat exchanger:

$$\Delta E = \int_{T_0}^T (-T_0 \times \Delta S) dT = -T_0 \int_{T_0}^T (S_{(T)} - S_{0(T)}) dT$$

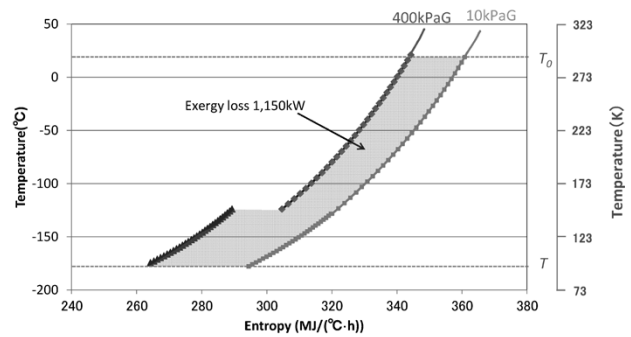


Fig. 2 T-S diagram of main heat exchanger in double-column rectification process

This means that in the T-S diagram shown in Fig. 2, the area encompassed by the plots on the high-temperature side and those on the low-temperature side becomes almost equal to the amount of exergy loss.<sup>3)</sup> More specifically, the exergy analysis was conducted on an imaginary apparatus with the following specifications:

Oxygen flow rate: 10,000Nm<sup>3</sup>/h

Oxygen purity: 93% or higher

Oxygen pressure: 10kPaG

Nitrogen flow rate: 34,400Nm<sup>3</sup>/h

Nitrogen purity: 99% or higher

Nitrogen pressure: 5kPaG

Air flow: 44,400Nm<sup>3</sup>/h (oxygen recovery rate 99.9%)

Air pressure: 450kPaG

Compressor efficiency: 70%

### 1.2.1 Amount of exergy loss for entire air-separation unit

In a double-column rectification process, the only apparatus to which external energy is supplied is the air compressor. The oxygen and nitrogen produced by this process are at a low pressure and at room temperature, conditions under which the exergy is almost equal to zero. Thus, the work applied to the air compressor is equal to the amount of exergy loss for the entire air-separation unit. On the basis of this, the amount of exergy loss for the entire air-separation unit is known to be 2,240kW.

### 1.2.2 Amount of exergy loss for main heat exchanger

The T-S diagram for the main heat exchanger in a double-column rectification process is shown in Fig.2. As described above, the amount of exergy loss for a heat exchanger can be calculated from T-S diagrams, and from the calculations performed using this diagram, it turns out to be 1,150kW.

Judging from the above, the amount of exergy



loss of the main heat exchanger, 1,150kW, accounts for more than half of the exergy loss of the entire air-separation unit, which is 2,240kW. Thus, decreasing the amount of the exergy loss of the main heat exchanger is the most effective way to save energy.

The T-S diagram in Fig. 2 shows that the plots for the high-temperature fluid (air) appear to the left of the plots for the low-temperature fluid (oxygen and nitrogen), indicating that this difference in entropy causes the increased amount of exergy loss. In this heat exchange, all of the raw-material air on the high-temperature side is at a pressure as high as approximately 400kPaG, while all of the fluid on the low-temperature side is as low as approximately 10kPaG. The greater this pressure difference is, the greater the amount of exergy loss for the heat exchanger. Therefore, in order to decrease the amount of exergy loss for the main heat exchanger, the pressure at the air compressor must be decreased so as to shift the plots of the high-temperature side to the right.

### 1.3 Problems of double-column rectification process

As described in 1.2, in order to decrease the amount of exergy loss for the main heat exchanger, the air-compressor pressure must be decreased. In a double-column rectification process, however, the condenser for the HP column is unified with the reboiler for the LP column. This is to allow the latent heat of condensation from the HP column condenser to be thermally recovered as the latent heat of vaporization of the reboiler at the bottom of the LP column, so as to establish rectification without supplying heat into the cryogenic system (Fig. 3). This configuration makes it difficult to significantly decrease the air-compressor pressure.

According to the second law of thermodynamics, in order to transfer heat from the HP column condenser to the LP column reboiler, the temperature at the top of the HP column (condenser) must be kept higher than the temperature at the bottom of the LP column (reboiler.)

In addition, for a given pressure, the boiling point of oxygen is higher than that of nitrogen. For example, the boiling point of oxygen at 30kPaG, the normal operating pressure of the LP column, is -180°C, while the boiling point of nitrogen is -194°C. Therefore, the pressure on the nitrogen side (HP column) must be raised to around 400kPaG, almost quadrupling the pressure on the oxygen side (LP column).

For the reasons described above, it is difficult to significantly decrease the air-compressor pressure,

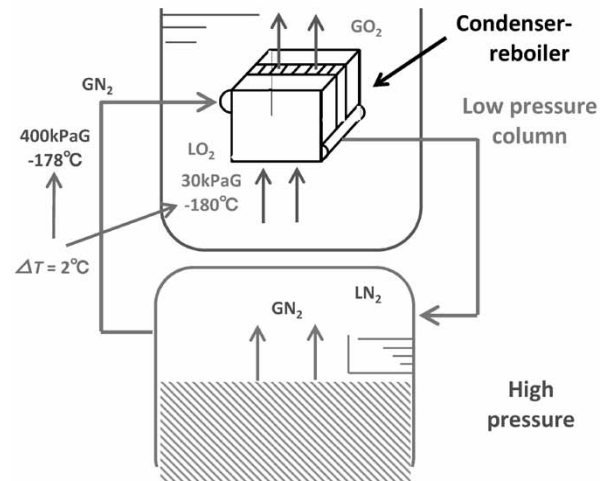


Fig. 3 Condenser-reboiler of double column rectification process

as long as we use a double-column rectification process consisting of two separate rectification columns and a condenser-reboiler coupled between them.

## 2. Single-column rectification process

### 2.1 Establishment of single-column rectification process

As described in 1.2, decreasing the amount of exergy loss in the main heat exchanger requires decreasing the air-compressor pressure. Now, the challenge is to establish a process in which the air-compressor pressure becomes equal solely to the pressure loss in the equipment and piping.

After due consideration, it was found that a single-column rectification process (Fig.4) comprising the following process elements can decrease the air-compressor pressure significantly.

- A single-column rectification is applied. This enables the air-compressor pressure to be equal solely to the pressure loss in the equipment and piping.
- A recycle nitrogen compressor is installed to provide a heat source for the bottom reboiler in the single-column rectification. Nitrogen is taken in at the top of the rectification column, and a part of the nitrogen is pressurized by the recycle nitrogen compressor so as to raise its saturation temperature. The pressurized nitrogen is introduced into the condenser-reboiler at the bottom of the rectification column, which vaporizes the liquefied oxygen at the bottom of the column.
- The latent heat of vaporization from the liquefied oxygen in the condenser-reboiler

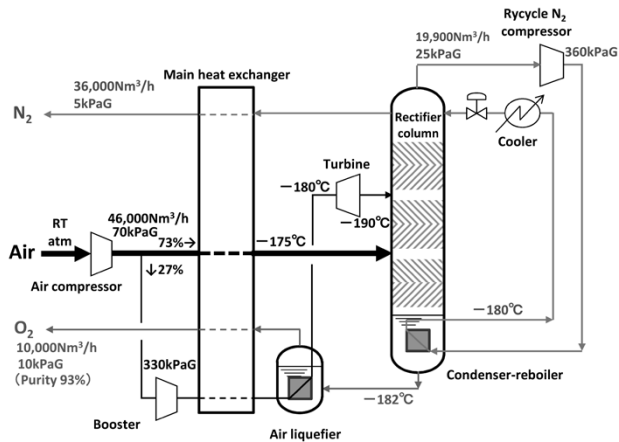


Fig. 4 Single-column rectification process

liquefies the nitrogen pressurized by the recycle nitrogen compressor. The nitrogen thus liquefied is supplied to the top of the rectification column as reflux.

- To liquefy a part of the air fed into the rectification column, that portion of air is pressurized by a booster compressor so as to increase its saturation temperature. This air is heat-exchanged with the liquefied oxygen taken from the bottom of the rectification column by an air condenser (Air Liquefier). This results in liquefying the compressed air and vaporizing the liquefied oxygen.

## 2.2 Exergy evaluation of single-column rectification process

As will be described below, the use of the single-column rectification process enables a significant decrease in the amount of exergy lost.

### 2.2.1 Amount of exergy loss for entire single-column rectification process

A single-column rectification process involves three compressors: namely, an air compressor, a booster for generating feed-liquefied air, and a recycle nitrogen compressor for generating the reflux of liquefied nitrogen. The amount of work applied (i.e., the pressure energy provided from outside) is 1,390kW in total.

The single-column rectification process is provided with a cooler on the secondary side of the condenser-reboiler for liquefying compressed nitrogen. The cooler is supplied with cold heat for the amount of power consumed by the recycle nitrogen compressor. The amount of exergy loss for this cold heat is 190kW.

Consequently, the amount of exergy loss for the single-column rectification process is equal to

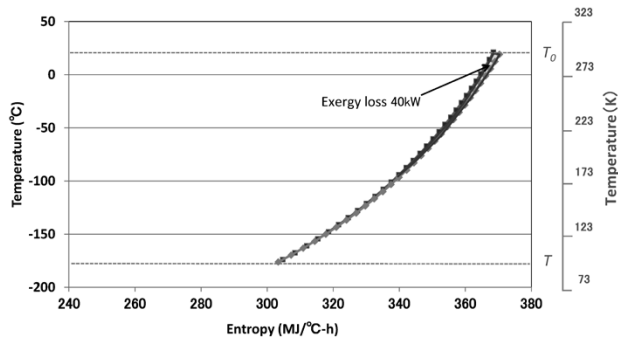


Fig. 5 T-S diagram of main heat exchanger in single column rectification process

1,580kW in total; i.e., the sum of the pressure energy applied and the exergy of the cold heat.

### 2.2.2 Amount of exergy loss for main heat exchanger in single-column rectification process

The T-S diagram of the main heat exchanger in the single-column rectification process is as shown in Fig. 5, which indicates an exergy loss of 40kW. This value is no greater than 5% of the amount of exergy loss for the main heat exchanger in the double-column rectification process. The exergy loss in this part is almost negligible.

As described above, the application of the single-column rectification process has significantly decreased the amount of exergy loss for the main heat exchanger, from 1,150kW to 40kW. The single-column rectification process, however, is additionally provided with a recycle nitrogen compressor and a booster compressor to establish the rectification. Part of the work applied by these compressors is added to the amount of work corresponding to the amount of exergy loss that is considered to occur outside the main heat exchanger in the double-column rectification process. Therefore, the amount of exergy loss outside the main heat exchanger is increased by 450kW, from 1,090kW to 1,540kW.

When the entire process is evaluated by the amount of exergy lost, however, the exergy loss of the single-column rectification process is decreased by 660kW (30%) compared with that of the double-column rectification process. In other words, the single-column rectification process is more efficient with a smaller exergy loss.

## 3. Energy-saving effect of single-column rectification process

A trial calculation was performed to see how much energy can be saved by using a single-column rectification process for an air-separation unit. The

Table 1 Comparison of power consumed by double column and single-column rectification processes

	Double column process	Single column process
Product oxygen (Nm <sup>3</sup> /h)	10,000	10,000
Air compressor		
Air flow (Nm <sup>3</sup> /h)	44,400	46,000
Pressure (kPaG)	450	70
Power (kW)	3,210	1,020
Booster compressor		
Air flow (Nm <sup>3</sup> /h)	-	12,500
Pressure (kPaG)	-	330
Power (kW)	-	610
Recycle N <sub>2</sub> compressor		
Nitrogen flow (Nm <sup>3</sup> /h)	-	19,900
Pressure (kPaG)	-	360
Power (kW)	-	370
Cold potential exergy		
Cold energy (kW)	-	370
Carnot efficiency (-)	-	0.73
Exergy (kW)	-	270
Power consumption (kW)	3,210	2,270

results are shown in **Table 1**.

Here, the power for the double column rectification process is consumed solely by its air compressor. The power for the single-column rectification process, on the other hand, includes the power consumed by the air compressor, booster compressor and recycle nitrogen compressor, taking into account the cold heat added by the cooler.

### 3.1 Power consumption of double-column rectification process

The power for the air compressor is estimated realistically by assuming its total efficiency to be 0.7, including impeller loss, motor power conversion efficiency and mechanical loss. The result gives 3,210kW, which corresponds to the power consumed by a double-column rectification process.

### 3.2 Power consumption of single-column rectification process

As with 3.1, assuming the total efficiency of the air compressor, booster and recycle nitrogen compressor to be 0.7, the total power consumed

by these compressors is estimated to be 2,000kW. Assuming the exergy of the cold heat to be consumed power, the cold heat is evaluated to be 270kW. The total of these values, 2,270kW, gives the power consumed.

From the above, the single-column rectification process consumes 30% less power (smaller by 940kW) compared with the conventional double-column rectification process. Hence the high efficiency of the single-column rectification process has been verified.

## Conclusions

This study indicates that a single-column rectification process with an increased amount of thermal cycling is an energy-saving process that can decrease the power consumption by approximately 30% compared with a conventional double-column rectification process.

The efficiency improvement of an air-separation unit not only results in energy-saving for the unit itself, but also represents technology that can contribute to large-scale energy saving through oxygen-enriched combustion and the like. This is considered to make its technical development even more meaningful.

Kobe Steel intends to use process simulation to resolve the issues involved in implementing this process as an actual plant and to develop highly-efficient air-separation units.

This paper is based on the achievements of the collaborative research conducted with Tsutsumi Laboratory, Collaborative Research Center for Energy Engineering, Institute of Industrial Science, the University of Tokyo. This paper owes much to the advice provided by Project Professor A. Tsutsumi and Project Associate Professor Y. Kansha. Our special thanks are due them.

## References

- 1) F. G. Kerry. Industrial Gas Handbook. Gas Separation and Purification CRC Press. 2006.
- 2) A. Kishimoto. Proceedings of the 9<sup>th</sup> Coproduction Workshop. 2010, p.105-111.
- 3) Y. Kansha et al. Evaluation of a self-heat recuperative thermal process based on thermodynamic irreversibility and exergy. J. Chem. Eng. Jpn. 2013, Vol.46, No.1, p.87-91.

Note) The names of companies and products cited herein may be trademarks or the registered trademarks of their respective owners.

# Fabrication and Properties of Forged Rings made of Modified 9Cr-1Mo-V Steel for High-temperature and High-pressure Reactor

Tomoya SHINOZAKI \*<sup>1</sup>, Tetsuya KOMURA \*<sup>1</sup>, Nobuyuki FUJITSUNA \*<sup>1</sup>, Hiroki NAKASHIMA \*<sup>1</sup>, Masato YAMADA \*<sup>2</sup>, Tomoaki NAKANISHI \*<sup>2</sup>

\*<sup>1</sup> Technical Development Dept., Steel Casting & Forging Div., Iron & Steel Business

\*<sup>2</sup> Takasago Equipment Plant, Energy & Nuclear Equipment Business Unit, Industrial Machinery Div., Machinery Business

*Recently, new processes have been developed for more efficiently cracking extra-heavy oil and liquefying coal. These new processes involve reactors, each operating at a temperature around 500°C. Modified 9Cr-1Mo-V steel, with its excellent high-temperature performance, is thus a candidate material for these reactors. A heavy-wall reactor is composed of a forged shell-ring made from an ingot weighing over 190 tonnes, and its wall thickness at the time of heat treatment becomes 300mm or greater. In the forging of modified 9Cr-1Mo-V steel made from an ingot weighing 30 tonnes, however, internal defects are likely to be formed; and the occurrence of casting defects become more serious as the size of the ingot increases, according to reports. Therefore, when producing forgings exceeding 100 tonnes, the internal quality of the forgings must be checked. An evaluation test was conducted; it verified that the heavy-wall shell ring made of modified 9Cr-1Mo-V steel exhibits no internal defects and has excellent material properties, satisfying the ASME requirements.*

## Introduction

As a result of various issues such as soaring crude-oil prices and shrinking oil resources, considerable interest has been focused on improving the efficiency of oil refining and effectively exploiting extra-heavy oil.<sup>1), 2)</sup> Against this background, new high-temperature processes have been developed for more efficiently cracking extra-heavy oil and liquefying coal, and the practical implementation of these processes is being studied. These new processes require reactors that operate under higher temperatures and higher pressures, and the design temperature for such a reactor is around 500°C. The conventional processes mainly use reactors made of Modified 2 1/4Cr-1Mo-V steel (ASME Gr.F22V)<sup>3)</sup>; however, the ASME boiler and pressure vessel code<sup>4)</sup> (hereinafter referred to as "ASME Section VIII, Division 2") stipulates that the upper limit of its design temperature is 454°C. That precludes the use of this material for reactors that are to be operated at temperatures around 500°C; but modified 9Cr-1Mo-V steel (ASME Gr.F91), for which the ASME Section VIII, Division 2 allows a design stress of around 500°C, becomes a candidate

for such use. A technical report<sup>5)</sup> issued by the American Petroleum Institute (API) also refers to the possibility of using this steel for pressure vessels.

In general, a reactor used for an oil refining plant consists of a pressure vessel that is a vertical hollow cylinder with a wall thickness exceeding 200mm. Some larger vessels can weigh close to 2,000 tonnes.<sup>6)</sup> These reactors are assembled by welding large forged shells. Such a shell for a large reactor is produced from a large ingot that weighs over 100 tonnes. Few products, however, have been made from ingots of modified 9Cr-1Mo-V steel exceeding 30 tonnes.<sup>7)</sup> Therefore, the material properties, associated with segregation and mass effect of large ingots, must be checked when producing a large forged shell. This paper reports the evaluation results for the material properties of a prototype heavy-wall forged shell made from an ingot weighing 190 tonnes.

## 1. Fundamental study

The material requirements for SA-336 Gr. F91, according to ASME Section II, are shown in **Table 1**. The chemical composition, mechanical properties and heat treatment conditions for this material are stipulated by ASME. The modified 9Cr-1Mo-V steel<sup>8)</sup> was initially developed by the Oak Ridge National Laboratory (ORNL) in the U.S. and is widely used as boiler steel for thermal power plants. However, no report has been published regarding its application to heavy-wall forgings produced from a large ingot weighing over 100 tonnes. Therefore, when producing such a forging, the mass effect on its material properties must be fully understood.

It is well known that the modified 9Cr-1Mo-V steel has a good hardenability. A plate of this steel with a thickness of several tens of millimeters exhibits a hardened structure (martensitic structure) even when air cooled after austenitization.<sup>9)</sup> As the thickness increases, however, the cooling rate slows at the center. Thus it is necessary to check whether or not a homogeneously hardened structure can be obtained for forgings with heavy walls thicker than 300mm.

In addition, it is specified that the holding times



**Table 1** Material requirements for SA-336 Gr.F91 (ASME Section II)

Chemical compositions (%)	
C	0.08 - 0.12
Mn	0.30 - 0.60
P	≤ 0.025
S	≤ 0.025
Si	0.20 - 0.50
Ni	≤ 0.40
Cr	8.0 - 9.5
Mo	0.85 - 1.05
V	0.18 - 0.25
Nb	0.06 - 0.10
N	0.03 - 0.07
Al	≤ 0.02
Ti	≤ 0.01
Zr	≤ 0.01
Mechanical properties	
Tensile strength	585-760 (MPa)
0.2% proof stress	≥ 415 (MPa)
Elongation	≥ 20 (%)
Reduction of area	≥ 40 (%)
Heat treatment (°C)	
Austenitizing temperature	1,040 - 1,080
Tempering temperature	730 - 800

both for the tempering after quenching and for the post-welding heat treatment (hereinafter, "PWHT") should be 1 hour per inch of thickness, meaning, for example, that it takes 10 hours or longer for a plate that is 300mm thick. Extended holding at a high temperature, for tempering or for PWHT, promotes the recovery of dislocations in the martensitic structure obtained by quenching, which softens the material. Therefore, it must be confirmed whether or not the mechanical properties specified by ASME can be achieved after tempering for an extended period of time.

In the view described above, an attempt was made to clarify the applicability of the modified 9Cr-1Mo-V steel to heavy-wall forgings. A forged test material weighing 150kg was prepared from an ingot made by vacuum induction furnace (VIF) melting. Using this material, a fundamental study was conducted regarding the mass effect on the material properties of the modified 9Cr-1Mo-V steel.

### 1.1 Effect of cooling rate during quenching

An ingot with a diameter of 210mm and weight of 150kg was forged into a test material with a thickness of 65mm. This test material was used to study the effect of the cooling rate on quenched hardness. The results are shown in **Fig. 1**. A cooling rate slower than 180°C/h results in the precipitation of ferrite/pearlite, which decreases the quenched hardness. This decrease is more pronounced at a

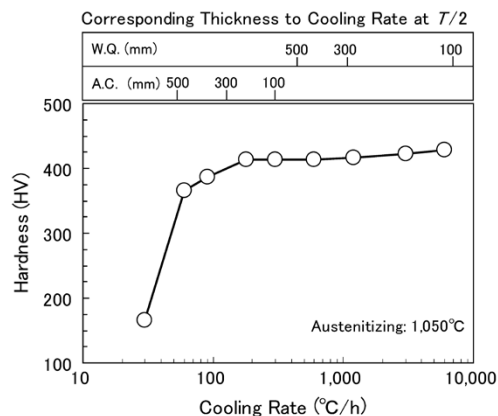


**Fig. 1** Effect of cooling rate on as-quenched hardness of modified 9Cr-1Mo-V steel

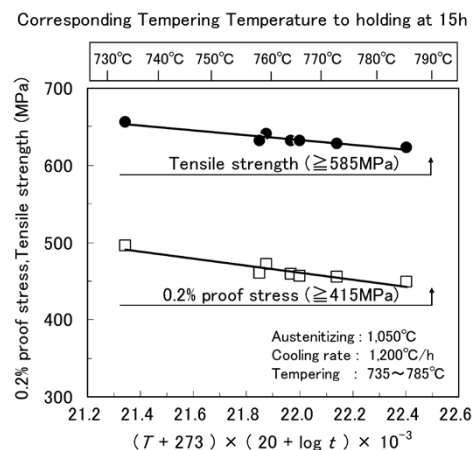


**Fig. 2** Effect of tempering conditions on 0.2% proof stress and tensile strength for modified 9Cr-1Mo-V steel

cooling rate of 60°C/h or slower. A cooling rate of 180°C/h or faster results in a single-phase structure of martensite with an almost constant hardness.

When a steel forging with a thickness of 300mm is air-cooled (A.C.) after austenitization, the cooling rate at the center of the thickness (1/2 T) becomes approximately 100°C/h, which results in a mixed structure of ferrite and pearlite. When this steel is water cooled (W.Q.) after austenitization, on the other hand, the cooling rate at 1/2 T becomes approximately 1,200°C/h, which results in a homogeneous martensitic structure.

Thus, in order to harden the structure deep inside the heavy wall of a steel forging, the cooling rate must be increased—by water cooling, for example.

### 1.2 Effect of tempering conditions on mechanical properties

**Fig. 2** shows the relationship between tempering condition and strength, in which the tempering condition is expressed as; *Tempering parameter* =  $(T + 273) \times (20 + \log t) \times 10^{-3}$ , wherein  $T$  is tempering temperature (°C) and  $t$  is tempering

holding time (h). Both the 0.2% proof stress and tensile strength decrease with an increasing tempering parameter (i.e., higher temperature and/or longer time), however, the mechanical properties still satisfy the ASME specifications even after an extended tempering of 15 hours.

The material properties specified by the ASME standard are therefore considered to be achievable when the modified 9Cr-1Mo-V steel is applied to heavy-wall forgings.

## 2. Trial production of large forged shell-ring

When a steel forging is produced from a large ingot, the segregation inherent to large ingots may affect the material properties. With this in mind, a shell ring in a shape of a hollow cylinder was forged as a trial from a 190 tonne ingot to confirm its material properties. The manufacturing process of the trial shell ring is shown in Fig. 3. The following outlines the steps in this process.

### (1) Melting and ingot making

A 100 tonne electric arc furnace and vacuum holding furnace (VHF) were used to produce a 190 tonne ingot. This step employed a double degassing (tapping-degassing and vacuum casting) to decrease oxygen, hydrogen and oxide inclusions.

### (2) Forging

The ingot was heated and upset-forged. A solid punch was used to bore a hole in the center of the forged ingot, and a mandrel was inserted through it to expand the diameter. A shell ring with an outer diameter of 4,550mm and a wall thickness of 310mm was produced in this way.

### (3) Heat treatment

The forged shell ring was heat treated by

quenching and tempering. The quenching was performed by heating to 1,060°C for homogenizing and by subsequent water cooling. The tempering was performed at 740°C.

### (4) Non-destructive testing

The heat-treated product was machined into a predetermined shape and was subjected to ultrasonic testing and liquid penetrant testing. These non-destructive evaluations revealed no defects at a minimum detectable defect size (MDDS) of  $\phi 0.8\text{mm}$ , verifying the integrity of the forged shell ring.

## 3. Evaluation results for trial shell ring

Welded pressure vessels are subjected to PWHTs so as to reduce the residual stress caused by welding. The mechanical properties required for each material must be satisfied after the PWHT. In order to check the mechanical properties after PWHT, test pieces were cut out, as shown in Fig. 4, from the  $T$ - $T/4$  and  $T$ - $T/2$  positions on both ends of the heat treated shell ring (in which  $T$  represents the wall thickness, 310mm, of the shell ring). These test pieces were subjected to a heat treatment simulating a PWHT at 775°C for 32h, and their material properties were evaluated. The following describes the results.

### 3.1 Chemical compositions

Table 2 shows the chemical composition at several positions of the trial shell ring. No compositional segregation was observed at any of these positions, and homogeneous distribution of the alloying elements was confirmed. In addition, impurities such as P and S were found to be sufficiently low.

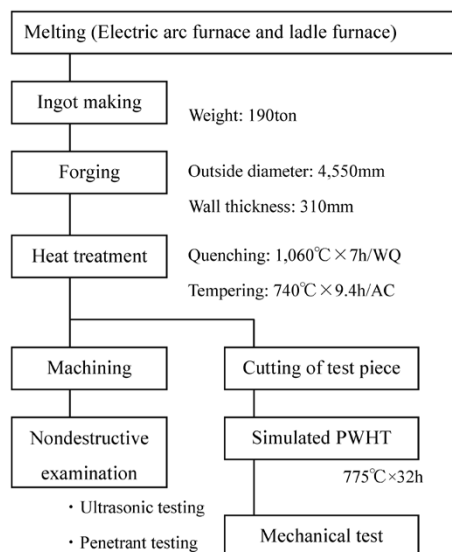


Fig. 3 Manufacturing process of trial shell ring

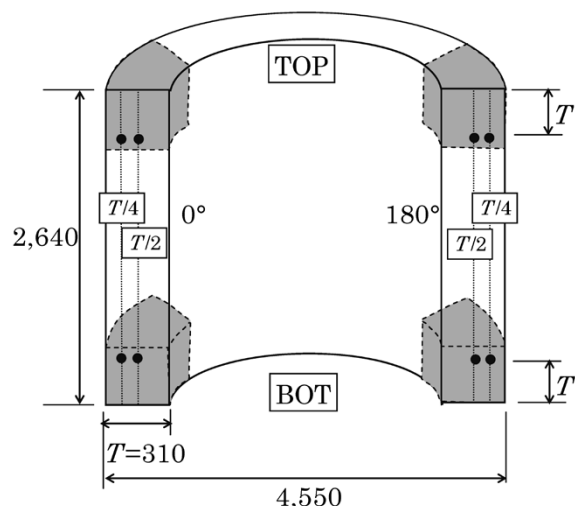
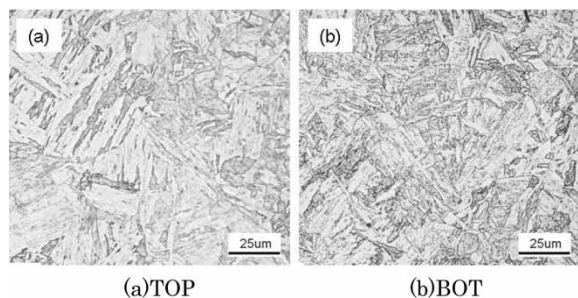


Fig. 4 Shape and dimensions of trial shell ring and sampling position of test specimen

**Table 2** Chemical composition of trial shell ring

Position		(mass%)														
		C	Si	Mn	P	S	Ni	Cr	Mo	V	Nb	N	Al	Ti	Zr	
TOP	T/2	0°	0.11	0.26	0.50	0.010	0.001	0.33	8.87	0.95	0.22	0.07	0.05	0.003	0.002	0.001
		180°	0.10	0.26	0.51	0.010	0.001	0.33	8.88	0.95	0.22	0.07	0.05	0.002	0.002	0.001
	T/4	0°	0.11	0.26	0.50	0.010	0.001	0.33	8.88	0.95	0.22	0.07	0.05	0.003	0.002	0.001
		180°	0.10	0.26	0.51	0.010	0.001	0.33	8.92	0.96	0.22	0.07	0.05	0.003	0.002	0.001
BOT	T/2	0°	0.10	0.26	0.50	0.009	0.001	0.33	8.89	0.94	0.22	0.07	0.05	0.003	0.002	0.001
		180°	0.10	0.26	0.51	0.010	0.001	0.33	8.93	0.96	0.22	0.07	0.05	0.002	0.002	0.001
	T/4	0°	0.11	0.26	0.51	0.010	0.001	0.33	8.92	0.96	0.22	0.07	0.05	0.002	0.002	0.001
		180°	0.10	0.26	0.51	0.010	0.001	0.33	8.92	0.96	0.22	0.07	0.05	0.003	0.002	0.001



**Fig. 5** Optical microstructure at center position of wall thickness

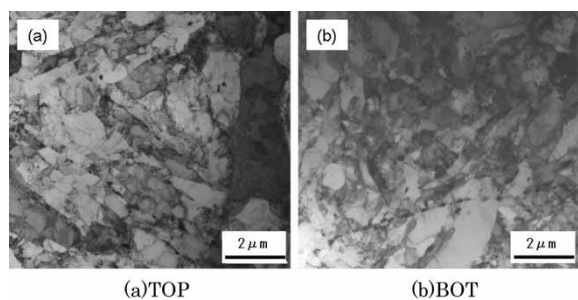


**Fig. 6** TEM micrographs at center position of wall thickness

### 3.2 Microstructure

**Fig. 5** shows optical micrographs taken at the center of the wall thickness. Both of the micrographs show single-phase structures of homogeneously distributed tempered martensite with no indication of the ferrite precipitates that are detrimental to strength and toughness. **Fig. 6** shows the electron micrographs at the center of the wall thickness. The tempering and PWHT has promoted the recovery of dislocations. Both these TEM micrographs exhibit a martensite lath structure.

### 3.3 Mechanical properties

**Fig. 7** summarizes the results of tensile testing and Charpy testing at various positions. Tensile properties with favorable strength and ductility were obtained at each position. There is no indication of positional variation. Furthermore, the specifications of ASME Gr.F91 were satisfied at all these positions. The fracture appearance transition temperature

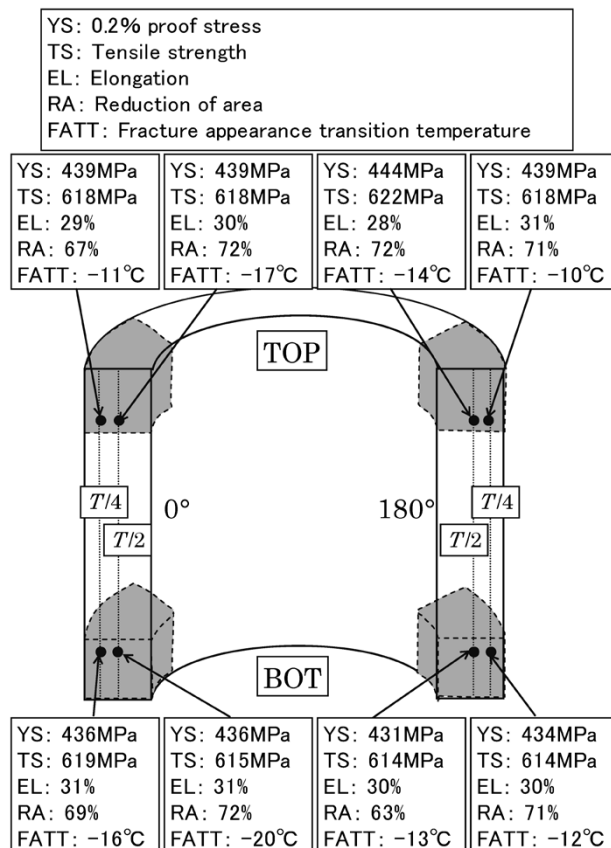


**Fig. 7** Mechanical properties of trial shell ring at each position

(FATT) falls in the vicinity of -15°C for each position, demonstrating favorable low-temperature toughness.

### Conclusions

A forged shell ring of modified 9Cr-1Mo-V steel was produced from a 190 tonne ingot. The material properties of the trial shell ring were introduced in this paper. Ultrasonic testing confirmed that the trial shell ring produced via the process steps of electric-arc-furnace melting, ingot making and forging exhibited no defects. The product was verified to have favorable material properties. Kobe Steel will strive to research and develop technologies for improving production techniques and quality and, thus, to respond to the needs of our customers.

## References

- 1) Mohan S. Rana et al. Fuel. 2007, Vol.86, p.1216-1231.
- 2) Yuandong Liu et al. Recent Patents on Chemical Engineering. 2009, Vol.2, p.22-36.
- 3) Shiro Nose et al. ASME PVP. 1998, Vol.380, p.301-314.
- 4) ASME boiler and pressure vessel code. Sect. VIII, Div. 2, 2007 Edition.
- 5) API Technical Report 938-B. First Edition. 2008.
- 6) M. Yamada et al. Kobe Steel Engineering Reports. 2013, Vol.63, No.2, p.40-43.
- 7) Y. Yamamoto et al. The Proceedings of 15th International Forgemasters Meeting. 2003, p.282-289.
- 8) P. Patriarca. Modified 9Cr-1Mo Steel Technical Program and Data Package for Use in ASME Section I and VIII Design Analyses. ORNL, 1982.
- 9) Y. Tsuchida et al. TETSU-TO-HAGANE. 1994, Vol.80, p.723-728.

---

Note) The names of companies and products cited herein may be trademarks or the registered trademarks of their respective owners.



# Technologies for Process Design of Titanium Alloy Forging for Aircraft Parts

Takashi CHODA\*<sup>1</sup>, Dr. Hideto OYAMA\*<sup>2</sup>, Shogo MURAKAMI\*<sup>3</sup>

\*<sup>1</sup> Titanium Research & Development Section, Titanium Div., Iron & Steel Business

\*<sup>2</sup> Titanium Div., Iron & Steel Business

\*<sup>3</sup> Titanium Plant, Titanium Div., Iron & Steel Business

*Titanium alloys are widely used for aircraft parts, thanks to their high specific strength. It is important, in dealing with titanium alloy forgings, to control the history of temperature and plastic strain in order to obtain desired microstructures and mechanical properties. This paper introduces an example in which a process is designed using finite element method (FEM) analysis for  $\beta$ -processed forgings of a jet engine disk made of Ti-6246 alloy.*

## Introduction

Titanium alloys are superior to other metallic materials in specific strength (=0.2% proof stress / density). More than 50% of titanium alloy forgings used worldwide are for aircraft members requiring weight reduction and strength.<sup>1)</sup>

Supported by increasing passenger demand in recent years, the market for commercial aircraft is growing at a rate of 4 to 5% every year. Including replacement units, the demand for commercial aircraft is expected to more than double in the next 20 years.<sup>2)</sup> In addition, the quantity ratio of titanium alloy used per aircraft has increased lately, and the demand for titanium alloy forgings is on the increase.

On the other hand, titanium alloy is regarded as a difficult-to-forge material, and it is difficult to fill dies with the alloy to obtain the desired shapes. In addition, titanium alloy forgings for aircraft, in particular for rotating parts such as engine disks and shafts, are required to have high reliability. Thus the temperature, strain and strain rate during forging must be so controlled that the specifications for the material properties and quality inspection are satisfied.

Further, compared with other metallic materials, titanium alloys are poor in machinability, resulting in a high machining cost in addition to their high material cost. Hence, in order to expand the demand for them in aircraft and other applications, it is important from the aspect of forging technology to improve the yield through near-net shaping while securing quality.

This paper describes the forging technology of titanium alloy parts for aircraft.

## 1. Titanium alloy forgings used for aircraft

Titanium alloy forgings are used for various parts of airframe structures and engines. In the case of the Boeing 787, for example, titanium alloy accounts for approximately 15% of structural members, more than doubling the amount used for conventional aircraft. The amount (estimated) of titanium alloy used per unit has reached approximately 100 tonnes.<sup>2)</sup> This is because titanium alloy has a high compatibility with carbon fiber reinforced plastic (CFRP), which is used in large amounts in place of aluminum alloy to reduce airframe weight and thus to improve fuel economy. When joined with CFRP members, titanium alloy is less likely to cause galvanic corrosion and inhibits strain due to temperature change, since its coefficient of thermal expansion is similar to that of CFRP.

A titanium alloy commonly used for airframe structure parts is Ti-6Al-4V (acronym; Ti-64), which accounts for 80 to 90% of the titanium alloys generally used for aircraft. Ti-64 is the most widely used  $\alpha$ - $\beta$  alloy, having well balanced characteristics with an abundance of data and application history.

Meanwhile, among the airframe structure parts, aircraft legs, called landing gears, must be made of high-strength, high-toughness material that can support mid to large-sized aircraft, each weighing as much as 200 to 400 tonnes, and tolerate the impact at the time of landing. NiCrMo steel has been mainly used for this purpose; however, new titanium alloys are being adopted. For example, the Boeing 777 and Airbus A380 employ a high-strength titanium alloy, Ti-10V-2Fe-3Al, of near- $\beta$  type (this alloy having a higher concentration of  $\beta$ -stabilizing element than other  $\alpha$ - $\beta$  alloys), and the Boeing 787 has adopted Ti-5Al-5Mo-5V-3Cr.<sup>3)</sup> Although these titanium alloys are more expensive than Ti-64, they are superior in forgeability and can be strengthened by solution and aging treatment after forging.

In aircraft engines, titanium alloys find many applications for fans and compressor parts used at temperatures of 590°C or lower.<sup>2)</sup> Ti-64 alloy is used for fan disks and low-pressure compressor disks. For mid-pressure compressor disks, Ti-6Al-2Sn-4Zr-6Mo (Ti-6246) alloy and Ti-5Al-2Sn-2Zr-4Cr-4Mo (Ti-17) alloy, both near- $\beta$  type, solutioned and aged, are used. For high-pressure compressor

disks, which are exposed to higher temperatures, forgings made of heat-resistant titanium alloys are used. These alloys include Ti-5.8Al-4Sn-3.5Zr-0.7Nb-0.5Mo-0.35Si alloy (IMI834), which is near- $\alpha$  type (an  $\alpha$ - $\beta$  alloy containing a smaller amount of  $\beta$  stabilizing elements). For rotating bodies such as fans, compressor disks, shafts, and blades, various high-level characteristics are required, including ease of defect detection by ultrasonic testing (UT), in addition to static strength, fatigue strength and fracture toughness.<sup>4)</sup>

## 2. Characteristics of titanium alloys in hot forging

As shown in Fig. 1, titanium alloys are roughly classified into three categories depending on the types of additional elements and their amounts: namely,  $\alpha$  alloy,  $\alpha$ - $\beta$  alloy and  $\beta$  alloy.<sup>5)</sup> The  $\alpha$ - $\beta$  alloys are most commonly used. All these alloys are composed of two phases, i.e., an  $\alpha$ -phase with a close-packed hexagonal structure and a  $\beta$ -phase with a body-centered cubic structure. These phases greatly affect the forgeability and mechanical properties of the alloys, depending on their amount, size and morphology. In general, a higher content of  $\beta$  stabilizing elements, such as Mo, V, Cr and Fe, increases the amount of  $\beta$  phase and improves forgeability. An excessively large amount of  $\beta$  stabilizing elements, however, lowers the  $\beta$  transus temperature (i.e., the transition temperature between the  $\alpha$ + $\beta$  dual phase region and  $\beta$  single phase region), raising the flow stress for  $\alpha$ - $\beta$  forging (a method for forging in the  $\alpha$ + $\beta$  dual phase region), increasing the forging load required. Hence, the alloy type and forging method must be

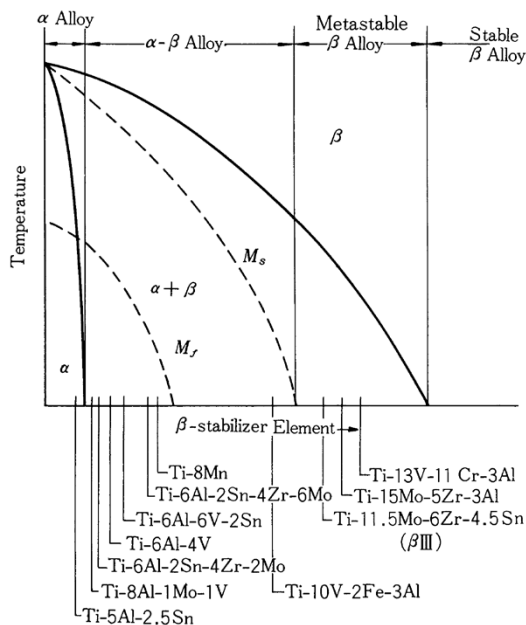
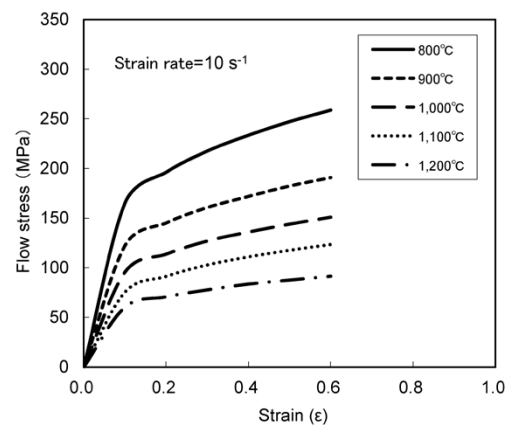


Fig. 1 Phase diagram of titanium alloy<sup>5)</sup>

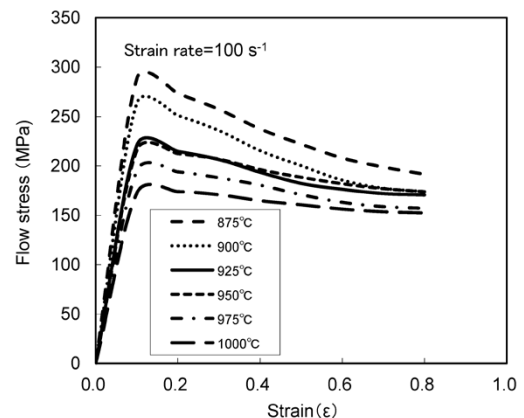
selected and combined appropriately depending on the applications and required characteristics.

Fig. 2 shows, as examples, stress-strain curves obtained during the hot working of the cylinder compression testing of a titanium alloy and commonly used steel. Steel generally exhibits work-hardening behavior, while titanium alloy shows a decline in the flow stress value as the strain increases, especially for deformation at a high strain rate. A material that shows work-softening behavior as described above exhibits a decline in flow stress at the portion where deformation first occurs, and this portion continues to deform preferentially during further processing. This results in inhomogeneous strain distribution inside forgings and, in the case of die forging, makes it more difficult to fill the dies. Furthermore, titanium is a material with relatively low thermal conductivity, which maintains and enhances the temperature distribution due to the inhomogeneity of strain during processing, making the temperature distribution also inhomogeneous, in addition to the strain distribution.

A typical production process for titanium alloy forgings is shown in Fig. 3, in which the post-forging heat treatment is usually conducted at a temperature



(a) Steel S25C at strain rate  $10 \text{ s}^{-1}$



(b) Titanium alloy Ti-6246 at strain rate  $100 \text{ s}^{-1}$

Fig. 2 Schematic illustration of flow stress curves at high temperatures

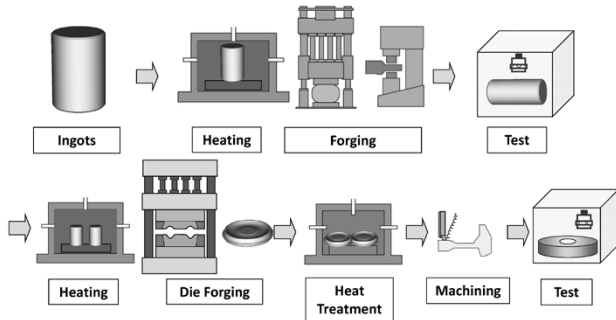


Fig. 3 Schematic illustration of titanium forging process

equal to or lower than the  $\beta$  transus temperature. Therefore, the as-forged conditions of the microstructure greatly influence the microstructural morphology and, consequently, the characteristics of the final product. Therefore, in the case of titanium alloys, it is extremely important, not only to obtain the product shapes, but to control the temperature, strain, and strain rate during forging, and the cooling rate after forging, and thus to achieve the desirable microstructures and characteristics.

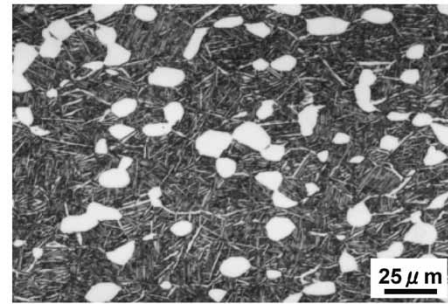
The next section focuses particularly on the influences of temperature and strain during forging and introduces the concept of process design for titanium forgings and the technologies required for the process, giving concrete examples.

### 3. Hot-forging technology for titanium alloys

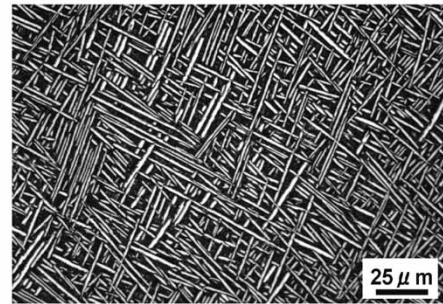
#### 3.1 $\beta$ -processed forging of Ti-6246 alloy disks for aircraft

As described above, titanium alloy, as a light-weight material with high strength, is widely used for the compressors in aircraft jet engines. Above all, high reliability is required for the rotating disks, each with moving blades attached to its circumference, and these are, therefore, made of forgings. The material properties required for these disks include high fatigue strength and excellent toughness. Ti-6246 is one such alloy that is in use.

The method of forging in a temperature region equal to or lower than  $\beta$  transus temperature ( $a + \beta$  region) is called " $a + \beta$  forging". The  $a + \beta$  forging yields a microstructure in which elongated  $a$  grains are segmented and equiaxed by reheating, which results in a dual phase structure of  $a + \beta$  consisting of equiaxial  $a$  grains and a matrix consisting of fine acicular  $a$  (Fig. 4(a)). This microstructure, however, has the problem of low fracture toughness. One production method for alleviating the problem is a forging process involving heating in the  $\beta$  region (hereinafter referred to as " $\beta$ -processed forging") prior to forging. In this process, the  $a$  phase precipitates very little during forging, precipitating



(a)  $\alpha - \beta$  forging



(b)  $\beta$  processed forging

Fig. 4 Microstructure of forged Ti-6246

mainly during the post-forging cooling. This results in an acicular microstructure occupying the entire body as shown in Fig. 4 (b), which achieves high fracture toughness. A conventional disk forged in the  $a + \beta$  region has a fracture toughness around  $30 \text{ MPa m}^{1/2}$  at room temperature.<sup>6),7)</sup> On the other hand, a  $\beta$ -processed forged piece has a fracture toughness of  $50 \text{ MPa m}^{1/2}$  or higher.<sup>8),9)</sup>

Meanwhile, in  $\beta$ -processed forgings, the heating in the  $\beta$  region before forging causes the microstructure to transform, which almost eliminates the influence of the prior processing history. Therefore, the characteristics of forged pieces are affected significantly by the temperature and processing strain during the final forging. Hence, the conditions for  $\beta$ -processed forging must be highly controlled to achieve appropriate material properties.<sup>10)</sup>

#### 3.2 Appropriate conditions for $\beta$ -processed forging: microstructure

The concept of  $\beta$ -processed forging is based on the concept of suppressing continuous grain boundary  $a$ , the phase that decreases ductility and fatigue strength, and promoting acicular  $a$ , the phase that increases fracture toughness. These objectives are achieved by suppressing the preferential precipitation of  $a$  phase at the grain boundaries from work hardened  $\beta$  phase so that the acicular  $a$  phase precipitates throughout the entire body.

Fig. 5 shows the range of process conditions



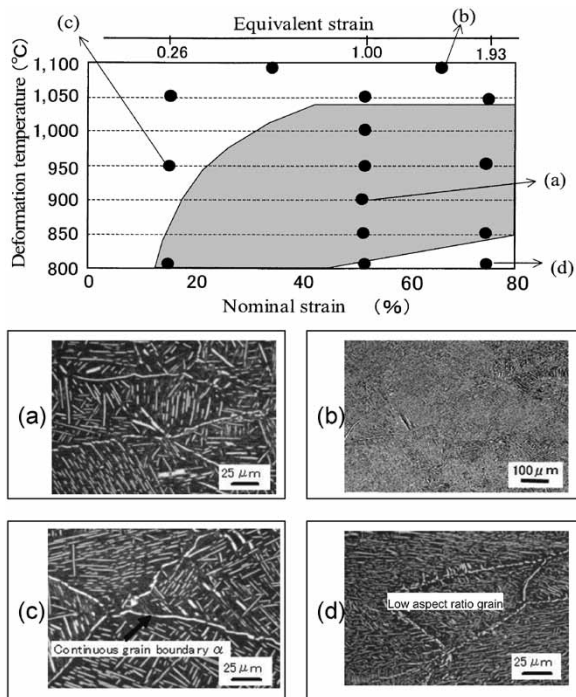


Fig. 5 Influence of temperature and strain on microstructure of Ti-6246,  $\beta$ -processed forging

based on microstructures. In the graph at the top of Fig. 5, the vertical axis represents the processing temperature and the horizontal axis represents the compression ratio. In order to take into account the inhomogeneous strain during the experiment, an upper horizontal axis is provided with equivalent strain of the microstructural area observed (at the thickness center and 1/2 radius), in which the equivalent strain was determined by FEM analysis. Fig. 5, at the bottom, includes microstructures obtained by the typical process conditions of the experiment. Condition (b) at a high temperature results in coarse  $\beta$  grains generated by recrystallization. Condition (c), with a small processing strain despite the relatively low temperature, results in a microstructure in which continuous grain boundary  $\alpha$  remains. Condition (d), at a relatively low temperature with a large processing strain, results in acicular  $\alpha$  that has a small aspect ratio (ratio of length to width) and is more equiaxed. Once the intragranular  $\alpha$  is equiaxed as described above, the resulting microstructure becomes similar to that of a piece forged in the  $\alpha+\beta$  region, which results in low fracture toughness and a high crack-propagation rate.

On the other hand, when processed under a condition in the shaded area of Fig. 5 (top), the grain boundary  $\alpha$  becomes discontinuous, showing an acicular microstructure with a large aspect ratio (i.e., with an elongated shape) inside grains, as represented by microstructure (a) of Fig. 5 (bottom), which improves fatigue characteristics.<sup>10)</sup>

### 3.3 Appropriate conditions for $\beta$ -processed forging: material properties

The influence on the material properties has been studied in addition to the relationship between metallographic structure and the forging conditions described above. First, compression forming was performed under conditions including a heating temperature of 1,000°C, die temperature of 850°C, and reduction ratios of 33% and 67% to prepare the forged pieces, each of which had a solid cylindrical shape with an outer diameter of  $\phi$  230mm and a thickness of 80mm. Their mechanical properties were studied. This paper describes the results of a tensile test and fatigue test whose results were significantly affected by strain. It should be noted that, in the current test range, the fracture toughness value at room temperature was 50 MPa m<sup>1/2</sup> or higher, regardless of the amount of strain.

Tensile specimens were cut out from each forged piece at its thickness center (1/2t), 1/4t and 10mm from the surface layer, such that the tensile axis of each specimen lay in a tangential direction. These specimens were solution treated at 930°C for 1 hr and aged at 595°C for 8 hrs before the test.

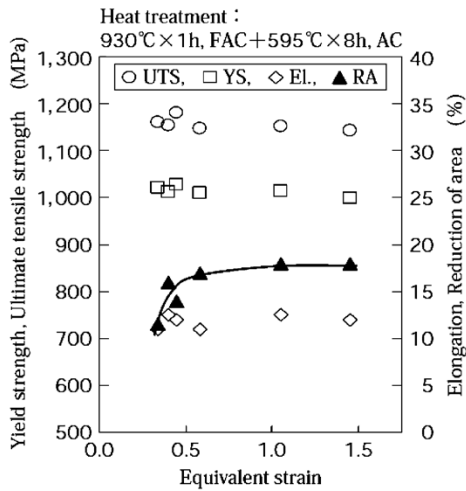
Fig. 6 (a) shows the tensile property at room temperature for each equivalent strain. The equivalent strain was determined by FEM analysis for each specimen position of the forged pieces compressed with ratios of 33% and 67%. The ultimate tensile strength (UTS) and yield strength (YS) show no influence of equivalent strain; however, the reduction of area (RA) is decreased at an equivalent strain of 0.5 or lower. Hence, an equivalent strain of 0.5 or greater must be applied to secure sufficient ductility.

Fig. 6 (b) shows the influence of equivalent strain on the failure life of low cycle fatigue (LCF), an important characteristic for materials used in jet-engine disks. The failure life tends to improve as the equivalent strain increases. Small equivalent strain leads to low ductility. Further, in a microstructure that has continuous grain boundary  $\alpha$  as a result of a small equivalent strain in forging, dislocations caused by applied stress tend to accumulate on grain boundary  $\alpha$ , facilitating the generation of fatigue cracks along grain boundary  $\alpha$ . These are considered to have caused the shortening of the fatigue life.

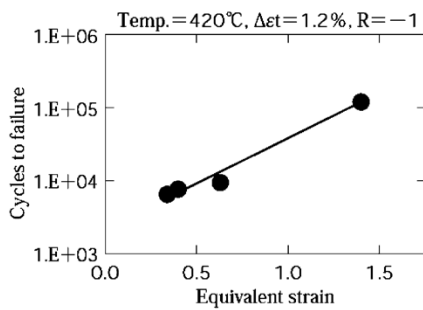
### 3.4 Process design based on analysis technology of $\beta$ -processed forging

As described above, to determine a forging process for obtaining a targeted disk shape while





(a) Tensile properties



(b) Low cycle fatigue life

Fig. 6 Influence of forging strain on tensile properties of Ti-6246,  $\beta$ -processed forging

controlling the temperature and strain in appropriate condition ranges, it is indispensable to predict the temperature and strain using deformation-temperature coupled FEM analysis. One of the important factors in performing this FEM analysis with high accuracy is the processing of flow stress data used in the FEM analysis.

The stress-strain curves of Ti-6246 were prepared on the basis of load-stroke measurement during cylinder compression testing. The results are shown in Fig. 7, which presents work softening, particularly at low temperatures, as described previously. In reality, however, the specimen temperature increases due to the generation of processing heat. Therefore, these results include the influence of the temperature change. In the deformation-temperature coupled analysis by FEM, the generation of processing heat is calculated separately; hence it requires flow stress values under constant temperature (isothermal) conditions, and the following technique was used to remove the influence of temperature rise due to the generation of processing heat.

First, the relationship between the flow stress  $\sigma$  and strain  $\varepsilon$  was assumed to be expressed as Equation (1):

$$\sigma = A(T) \times (1.0 + F \varepsilon^n) \quad \dots \dots \dots (1),$$

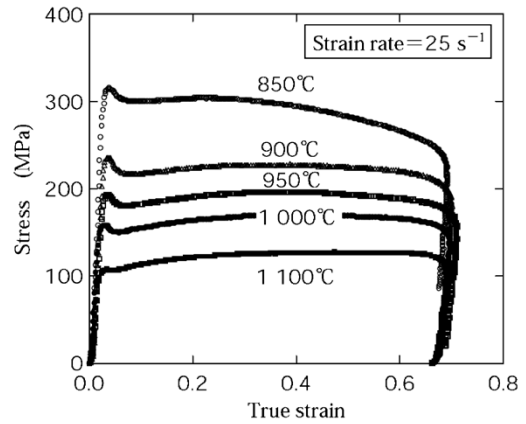


Fig. 7 Stress-strain curves of Ti-6246 as measured

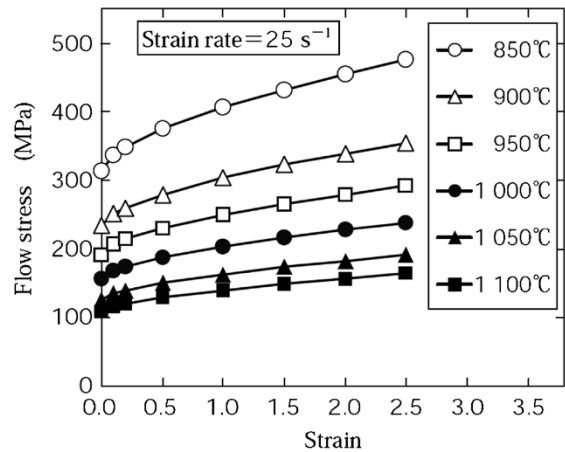


Fig. 8 Isothermal flow stress of Ti-6246

wherein  $A(T)$  is the initial flow stress value (a function of temperature  $T$  and strain rate),  $n$  is the work hardening index, and  $F$  is a coefficient.

In the low strain region, there is little influence from processing heat generation. Therefore, the yield points of the stress-strain curves shown in Fig. 7 were used to establish data for the dependence of flow stress on temperature and strain rate, and thus to determine  $A(T)$  of Equation (1). Next, deformation-temperature coupled analysis was conducted such that the stroke-load curves of the compression test coincide with the analysis results. Thus, the work hardening index  $n$  and coefficient  $F$  were optimized. Equation (1), obtained as above, enables the calculation of the isothermal flow stress in terms of temperature, strain rate and strain, as shown in Fig. 8.

An FEM analysis adopting the isothermal flow stress data was conducted to design the process for forging actual disks with a diameter of approximately 700mm. Fig. 9 shows the analysis results for shape and temperature/equivalent-strain distributions after forging under the conditions determined for  $\beta$ -processed forging, as well as the historic temperature/equivalent-strain during

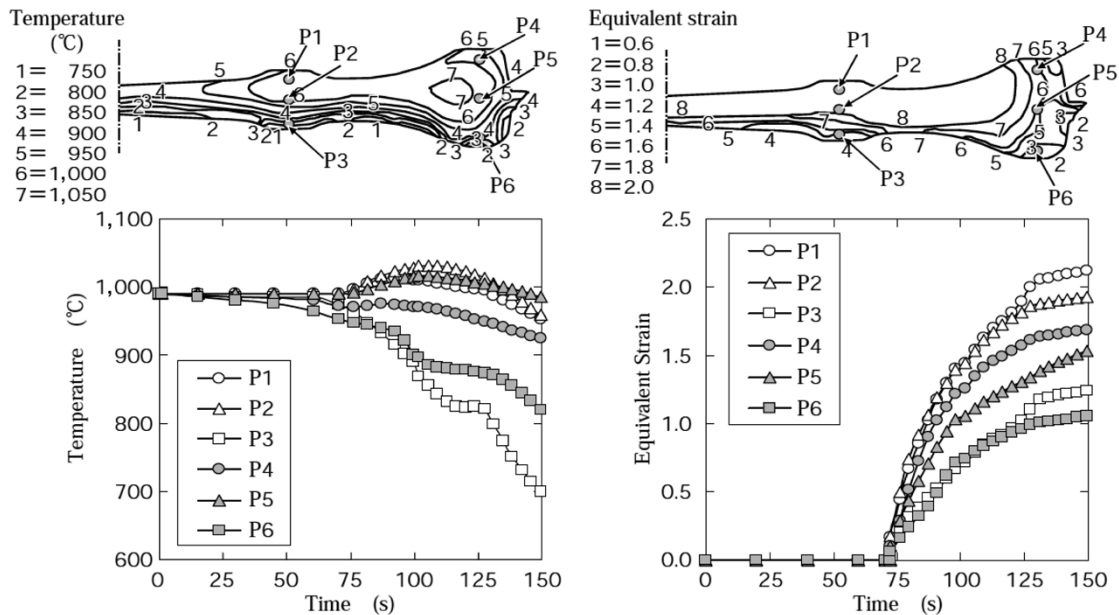


Fig. 9 Calculated results of temperature and strain during disk forging

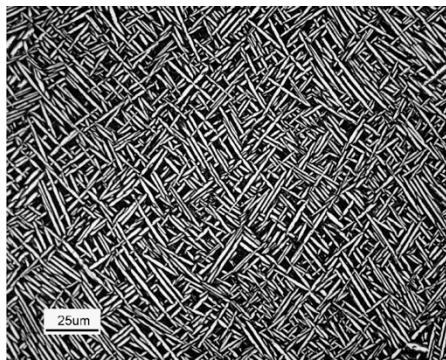


Fig.10 Microstructure of  $\beta$ -processed disk forging

forging at each location in the forgings. At each location, the deformation was completed within a range of appropriate conditions determined from the aspects of microstructures and material properties.

The process design technology, as described above, was adapted for prototype forgings, a typical micrograph of which is shown in Fig.10. The microstructure with acicular  $\alpha$ , as shown, has achieved a high fracture-toughness value exceeding  $50 \text{ MPa m}^{1/2}$  at room temperature.

### Conclusions

This paper has introduced a forging technology featuring titanium alloy forgings, with a focus on the example of disks forged for aircraft engines. Titanium is a material difficult to process, since it requires the precise control of temperature and strain to create the desired microstructures and

material properties. This, on the other hand, means that the material has the potential to make this forging technology stand out from others.

In Japan, a long-awaited giant press with a 50 thousand tonne capacity started to operate in 2013 at Japan AeroForge, Ltd. This press is expected to further increase the production volume of titanium alloy forgings for aircraft in Japan.

To that end, Kobe Steel is striving to establish analysis technologies that enable the highly accurate prediction of not only the shape and temperature, but also microstructures and material properties after forging and to achieve further advances in the forging technology for difficult-to-process materials as typified by titanium.

### References

- 1) S. Araki. *Titanium Japan*. 2008, Vol.57, No.1, pp.3-7.
- 2) Y. Moriguchi. *Material Science & Technology*. 2012, Vol.82, No.3, pp.211-217.
- 3) R. R. Boyer et al. *Ti-2007 Science and Technology*. 2007, Vol.2, pp.1255-1262.
- 4) S. Murakami et al. *Material Science & Technology*. 2013, Vol.83, No.4, p.33.
- 5) T. Hayashi et al. *R&D Kobe Steel Engineering Reports*. 1982, Vol.32, No.1, pp.36-39.
- 6) T. Nishimura et al. *R&D Kobe Steel Engineering Reports*. 1984, Vol.34, No.2, pp.89-92.
- 7) H. Yano et al. *Titanium Science and Technology*. 1984, p.507.
- 8) T. Krull et al. *Ti-2003 Science and Technology*. 2003, Vol. III, p.1871.
- 9) G. Terlinde et al. *Ti-2003 Science and Technology*. 2003, Vol. V, p.2891.
- 10) S. Ishigai et al. *R&D Kobe Steel Engineering Reports*. 2005, Vol.55, No.3, p.52.

# Efficient Inspection for Gas Pipes by Infrared Thermography

Hideki ENDO\*<sup>1</sup>, Takuya KUSAKA\*<sup>1</sup>

\*<sup>1</sup> Research & Development Dept., SHINKO INSPECTION & SERVICE, CO., LTD.

*Gas pipe failure caused by inner corrosion defects is one of the risk factors for the unscheduled shutdown of a plant. The pipes must be inspected to reduce the risk, but this requires a great amount of time and money, since gas pipes are quite long. This research proposes a screening method for the efficient inspection of gas pipes caused by aqueous corrosion. This screening method consists of three stages and includes thermographic and ultrasonic testing. We have developed new thermographic testing to find sludge in a pipe and to measure its wall-thinning distribution. The measuring principle and examples of the application of thermographic testing are introduced in this paper.*

## Introduction

Plants constructed in the 1960s, during the period of rapid economic growth, have already been operating for several decades. Once aged, main facilities generally have a higher probability of failure in their component equipment, increasing the maintenance cost and the risk of losing production opportunities due to facility shutdown. Thus, at manufacturing (MONODZUKURI) sites, it has become increasingly important to make facility maintenance plans and implement them before failure occurs. It is also important to establish an inspection technology for detecting symptoms of failure at the earliest stage possible.

In a steelworks, the major facilities for iron and steel making are repaired or renewed in a planned manner. Meanwhile, in order to secure the soundness of pipes, the wall thickness of each pipe must be measured by ultrasonic thickness gauges, for example, to ensure that sufficient thickness remains. A steelworks, however, has pipes that may extend for several tens of kilometers in total, and these pipes are usually installed in high places. Thus, inspecting the entire pipe surface to evaluate its soundness requires an enormous amount of time and money.

This paper introduces the results of a study on an efficient inspection method for pipes. The method combines infrared thermography with ultrasonic wave thickness measurement: the former allows remote non-contact testing over the surface of inspection objects (i.e., gas pipes), and the latter has a superior quantitative capability, despite its point

measurement nature.

## 1. Approach to problems of pipe inspection

The pipes that are the subject of this paper are metallic gas pipes, each being of a large caliber, with bases on the ground, and extending for several kilometers. The causes of pipe rupture include aqueous corrosion resulting from sludge that mainly consists of water and accumulates inside the pipe over an extended period of time. Observations on an actually ruptured pipe have revealed a case where the corrosion had progressed particularly in the pipe wall near the position of the interface where the sludge and inner gas fluid came in contact. This implies that it is important to grasp the wall thinning occurring near the interface of the sludge. The above knowledge indicates that measuring the presence/absence of the sludge, its interface position and the distribution of wall thinning in its vicinity can be of great help in determining the priority of repairs.

The conventional diagnosis of pipe deterioration includes visual inspection and/or thickness measurement by ultrasonic wave. There are, however, problems: a visual inspection cannot detect corrosion on the inner surface of a pipe, and thickness measurement by ultrasonic wave can only be performed at representative points and can easily miss inner surface corrosion progressing locally near the interface. Furthermore, in cases where the inner fluid pressure is high, a pipe may rupture where its wall has become thin, which restricts inspection. Thus, conventional inspection techniques alone were unable to achieve efficient screening.

In order to solve these problems, it was decided to proceed with the test in the following three stages:

First stage:

Confirming the presence/absence of sludge in a pipe by an infrared thermographic camera using a passive method (a test method based on infrared radiation from a measured subject without providing the subject with any artificial temperature change). If sludge is detected, the test proceeds to the second stage. If no sludge is detected, the test is "suspended."

Second stage:

Detecting the presence/absence of a part with a high rupture risk, a part in which corrosion

has progressed near the sludge interface, and is in the category of "pipe-wall thickness requiring immediate repair," or worse. This detection is conducted using an infrared thermographic camera by an active method (a test method involving heating or cooling of the measured subject to create artificial temperature change). When a thin-walled portion is detected, thickness measurement using ultrasonic wave is omitted due to the risk of rupturing. Otherwise, the test proceeds to the third stage.

Third stage:

If the second stage test detects a thin-walled portion near the sludge interface that falls into the category of "pipe-wall thickness requiring follow-up" or better, the thickness of this part is quantified using an ultrasonic thickness gauge. If no part is detected as being in the category of "pipe-wall thickness requiring follow-up," or better, the test is "suspended."

The criteria for detecting "pipe-wall thickness requiring immediate repair" and "pipe-wall thickness requiring follow-up" are determined in advance using simulation specimens.

The above three-stage test was used for screening the test subject pipes into three categories: i.e., "immediate repair", "follow-up" and "suspended". This concept is based on "triage" in the medical field, a technique for determining the priority of rescue when there are many injured or sick persons.<sup>1), 2)</sup> If appropriate repairs are performed in the order of pipes with higher risk, the risk of plant shutdown is expected to be reduced effectively and significantly. The following describes the method of detecting sludge by an infrared thermographic camera, used to determine the criteria for the categories, and the method for measuring the wall thinning distribution.

## 2. Method for detecting sludge

In a pipe, sludge and gas exist in separate areas. Thus, when a varying thermal load is applied to the pipe, these areas return different thermal responses. This enables to determine the interface positions of sludge by an infrared thermographic camera by measuring the nonsteady temperature distribution appearing on the outer surface of the pipe. The following describes two possible cases of thermal load variation applied to a pipe:

- (a) a case where thermal load applied from inside the pipe varies due to a change in the flow rate and/or temperature of gas flowing through the pipe; and
- (b) another case where thermal load applied from outside the pipe varies due to the change in

external environment, such as variations in solar radiant energy and air temperature.

Here, the latter case, (b), was chosen, as it frequently offers opportunities for actual measurement; heat transfer analysis and basic experiments using a simulated gas pipe were conducted, and the test conditions were studied.

## 2.1 Heat transfer analysis based on finite element method (FEM)

To clarify the qualitative trend for the conditions that enable the measurement of sludge inside a pipe, using the temperature distribution on the outer surface of the pipe, a heat transfer analysis was conducted, based on the finite element method (FEM). A varying thermal flux was applied to the outer surface and to the wall of a pipe to qualitatively study its effect.

### (1) Analysis model and analysis conditions

Under the conditions that maximize the temperature difference caused by the presence/absence of sludge, the possibility of detecting the interface by thermal imaging was confirmed. In order to accomplish this, the temperature distribution appearing on the pipe surface was estimated by two-dimensional steady-state heat conduction analysis based on FEM. The pipe wall was assumed to approximate a flat plate. The analysis model is shown in Fig. 1, while the material constants used are listed in Table 1.

Since the sludge has been confirmed to mainly consist of water, the material constants of water were

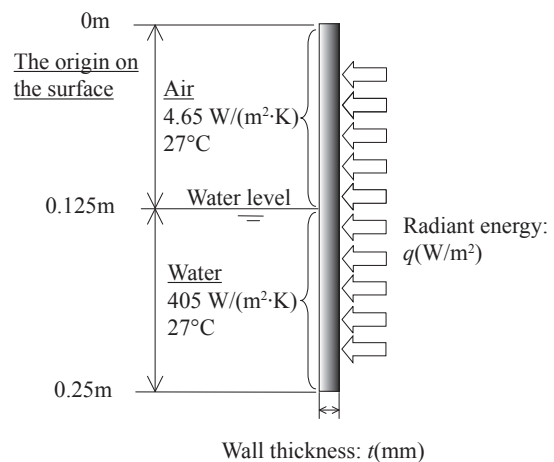


Fig. 1 FEM model

Table 1 Material constants used in the simulation

Mild steel	Density	7860 kg/m <sup>3</sup>
	Specific heat	473 J/(kg·K)
	Thermal conductivity	51.6 W/(m·K)



used. This analysis disregards the increase in the temperature of air and water. The analysis also takes into account the heat transfer between the pipe and air and that between the pipe and water; however, it disregards the heat transfer between the air and water. The wall thicknesses were 6mm and 12mm. The thermal fluxes were assumed to be  $800\text{W/m}^2$ , the value measured under fine weather in July, and  $200\text{W/m}^2$ , under slightly overcast conditions.

(2) Analysis results

First, the effect of thermal flux value was studied. Fig. 2 shows the temperature distributions on the outer surface of a pipe for the thermal fluxes, incident upon the 6mm thick plate, of  $200\text{W/m}^2$  and  $800\text{W/m}^2$ . It is shown that the greater the thermal flux value, the greater the temperature difference between the air and water, making it easier to detect the sludge.

Next, the effect of pipe-wall thickness was studied. Fig. 3 shows the temperature distributions on the outer surface of a pipe for the thermal flux of  $800\text{W/m}^2$  and pipe-wall thicknesses of 6mm and 12mm. It can be seen that the thinner the plate, the greater the temperature difference between the air and water becomes, making detection easier. For each condition analyzed this time, however, a temperature gradient was found at the position of

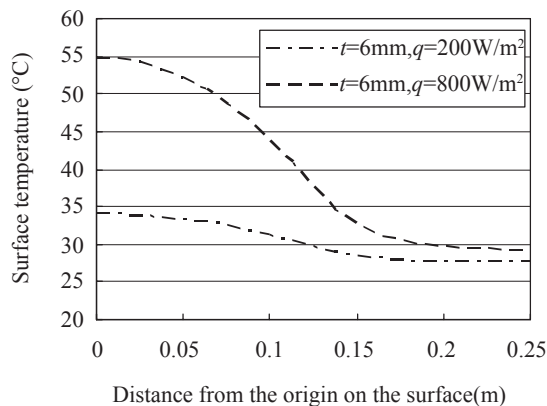


Fig. 2 Relation between radiant energy and temperature difference on the surface

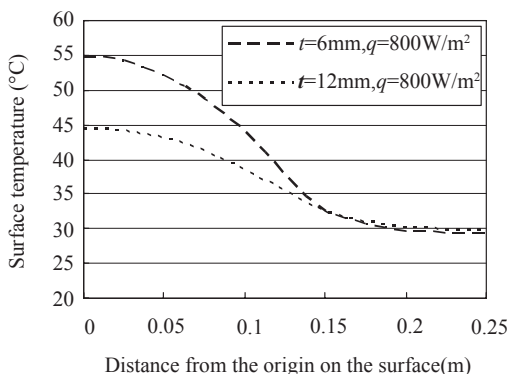


Fig. 3 Relation between wall thickness and temperature difference on the surface

the interface. It was found that this makes it difficult to determine the interface position of the sludge from the surface temperature distribution.

2.2 Estimation of interface position using differential progression

In the past, the level of sludge accumulated on the bottom of a petroleum tank or the like was determined by estimating the interface position of the sludge from thermal images taken at certain moments.<sup>3)</sup> This method, however, relies thoroughly on workers in determining the interface on thermal images. Thus, when no clear boundary is found, the detected interface position may vary depending on the workers. However, in view of this, a convenient method for detecting the interface has been devised in which the first differential progression is calculated for the temperature values along a line drawn on a thermal image so that estimation can be made from the local minimum or maximum point.

(1) Study based on numerical simulation

The surface temperature distribution obtained in Section 2.1, (2) was used to calculate the first differential progression to determine the interface position, and the results are shown in Fig. 4. For all the conditions, the interface position agrees with the position of local minimum point. The differential progression processing has a feature similar to differential processing and yields a minimum or maximum value at the interface where the temperature variation is greatest in the surface temperature distribution. It was found to be possible to detect the interface by obtaining the temperature distribution along a line crossing the interface in the thermal image and by calculating the first differential progression.

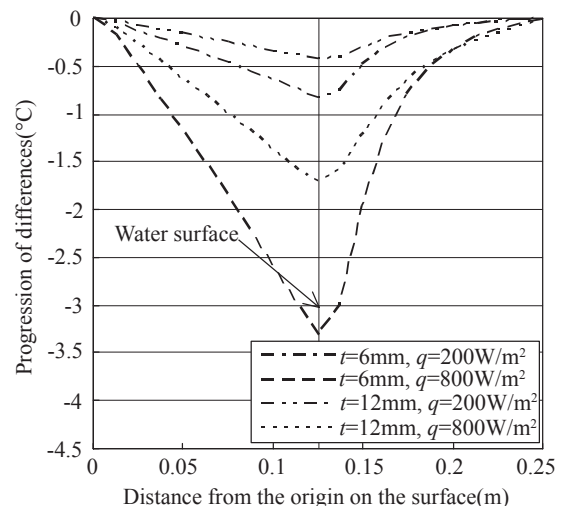


Fig. 4 Relation between local minimum point and water surface

(2) Test using simulated gas pipe

A simulated gas pipe (diameter, 300mm; length, 1,000mm; thickness, 3.2mm) was placed horizontally with water poured into it to a depth of 60mm to simulate sludge. Thermal images were taken every hour from 10 am to 3 pm, from below the pipe at an obliquely upward angle of 45 degrees. Fig. 5 shows a typical example of the measurement. Fig. 5 (b) is the thermal image, and Fig. 5 (c) shows the temperature distribution along the data processing line (shown by a dotted line) in Fig. 5 (b). The differential progression was calculated from Fig. 5 (c), the results being shown in Fig. 5 (d). Fig. 5 (d) demonstrates a good agreement between the local minimum point and the interface of the water. However, since pipe surfaces are curved, the pipe end portion in the image is susceptible to the disturbance of reflection due to the angle dependence of emissivity, which caused another local minimum point to appear also to the left of the true interface. Therefore, when determining the interface, several thermal images must be taken, not only from the oblique angle of 45 degrees, but also from various other angles, for a comprehensive judgment to be made.

(3) Evaluation by testing real pipes

Fig. 6 shows an example of measurement conducted on a gas pipe actually in use. It was confirmed by a radiographic test that sludge existed in a portion extending from the bottom to a position at 250mm of the  $\phi$ 1,200mm pipe. As in the case of the simulated gas pipe, the first differential progression was calculated for the central portion, A, of the area heated by the sun. Then a local minimum point appeared at a position approximately 230mm from the bottom. This agreed closely with the result of the radiographic test. The thermal image showed

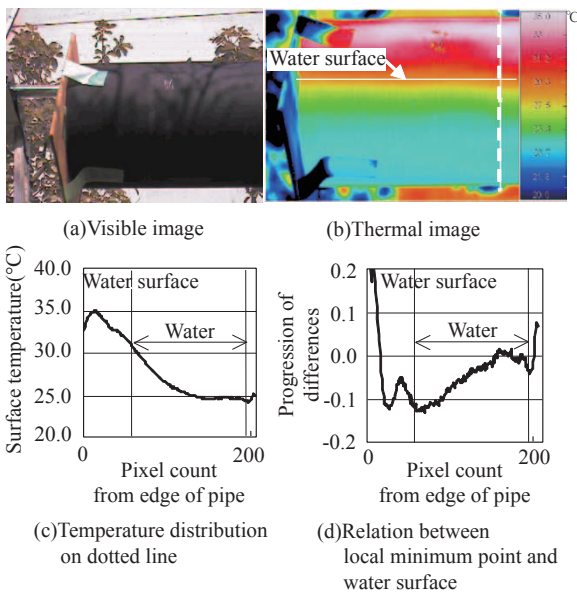


Fig. 5 Example of measurement of simulated gas pipe

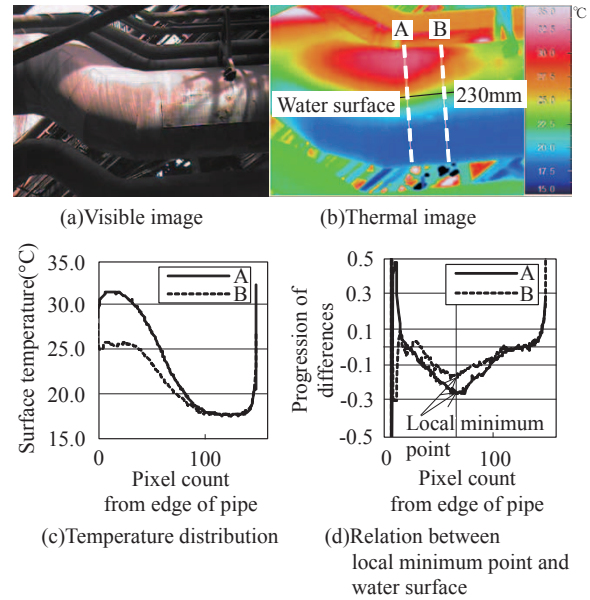


Fig. 6 Example of gas pipe measurement

the interface as if it were oblique. Thus, a new data processing line B was provided to the right of line A for comparison. As shown in Fig. 6 (d), both lines A and B indicated almost the same interface position. This result confirms the validity of the estimation method based on the first differential progression.

3. Method for measuring wall thinning distribution

The recent improvement in the temperature resolution of infrared thermographic cameras has facilitated the estimation of inner defects from several images of nonsteady temperature distribution captured at specific moments. This estimation of defects, however, is made from specific thermal images and is influenced by, for example, reflections from the surroundings, which often makes it difficult to estimate the defects. Against this backdrop, various methods have been studied to estimate defects by the signal processing of thermal images measured chronologically.<sup>4)</sup> Now, a convenient method has been devised for obtaining the wall thinning distribution while reducing the influence of disturbance. The method calculates the correlation coefficient of temperature change among the pixels of thermal images chronologically measured and thereby detects parts with significantly reduced thickness as the distribution of the correlation coefficients.

3.1 Study on validity of measuring wall-thinning distribution based on correlation coefficients

Using a specimen with flat-bottomed hole defects simulating locally thinned areas, a study was conducted on the issues of measuring wall-thinning

distribution. Measures against these issues were also studied. **Fig. 7** shows the details of the specimen used for this study. A 2.3kW halogen heater was placed at a position approximately 0.2m away from the specimen, which then was step-heated for approximately 20 seconds. Thermal images during and after the heating were continuously recorded at a frame rate of 5 frames per second by an infrared thermographic camera. **Fig. 8** shows a thermal image taken 3 seconds after the start of heating. The flat-bottomed hole defect in the middle of the specimen exhibits an area with a temperature higher than the surrounding area, allowing the detection of the wall thinning. Above this area, however, a zone affected by reflection caused by the halogen heater was observed, and this zone caused a higher apparent temperature to be measured. This is due to the fact that the reflected object, or halogen heater, has a much higher temperature than the specimen temperature, making the reflection from the specimen not negligible. The following signal processing was performed to distinguish defects from this disturbance.

The changes in temperature were measured chronologically at points "a" to "e" in the thermal image shown in Fig. 8, and the results are shown in **Fig. 9**. At a defect-free point, the temperature rises stepwise at the beginning of the heating and then increases linearly with a constant slope. Meanwhile, at a point with a flat-bottomed hole defect, the temperature tends to change gradually at

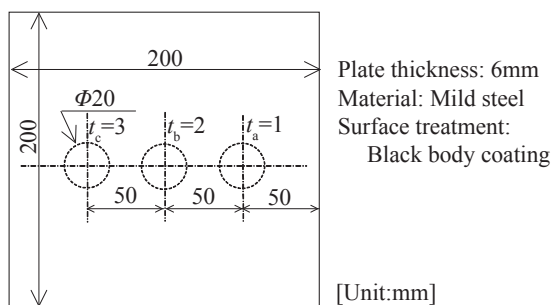


**Fig. 7** Dimension of specimen with flat-bottomed hole defects

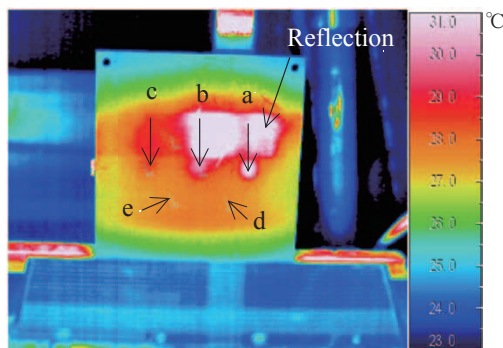


**Fig. 8** Thermal image at 3 sec after starting step heating

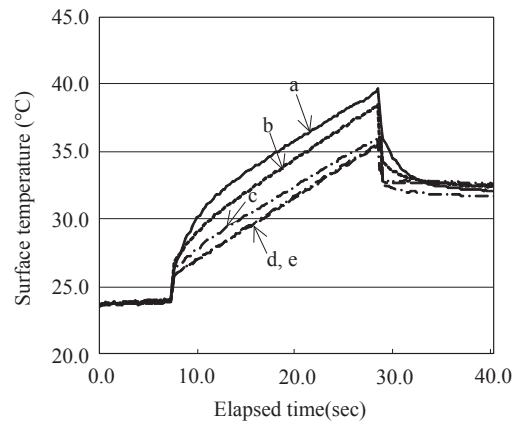


**Fig. 9** Relation between surface temperature and elapsed time

the beginning of the heating and then converge into a certain slope at the end. In addition, the thinner the remaining thickness under the flat-bottomed hole defect, the longer it takes before the convergence results in a certain slope. To digitize this difference in tendency, a defect-free point was selected to determine the correlation coefficient  $r$  with other pixels of chronological temperature change during the heating process. The correlation coefficient  $r$  was calculated by Equation (1):

$$r = \frac{\sum_{i=1}^n (x_i - \bar{x})(y_i - \bar{y})}{\sqrt{\sum_{i=1}^n (x_i - \bar{x})^2} \sqrt{\sum_{i=1}^n (y_i - \bar{y})^2}} \dots\dots\dots (1)$$

wherein  $x_i$  represents the chronological temperature change of the defect-free point, and  $y_i$  represents the chronological temperature change of each pixel. Further,  $\bar{x}$  and  $\bar{y}$  represent the average values of  $x_i$  and  $y_i$ , respectively. The correlation coefficient  $r$  means normalizing  $x_i$  and  $y_i$  so as to make their averages zero and variances 1, to determine the covariance. The influence of reflection is removed by normalizing the temperature change.

Thermal images were taken during 20 seconds of step heating. In the thermal images, the chronological temperature change at point "e" is regarded as that of the defect-free point. From this, a correlation coefficient distribution of each pixel was determined and the result is shown in **Fig.10**. The signal processing ignored the time zones right before the beginning and after the cessation of heating, during which the temperature changed stepwise at the defect-free point, but instead used the gradual temperature change during the step heating. In Fig.10, the three defects with flat bottoms are observed in the middle of the specimen, showing that the thinner the remaining thickness, the smaller the correlation coefficient becomes. Comparing Fig. 8 and Fig.10, the image for correlation coefficient distribution shows a significantly reduced



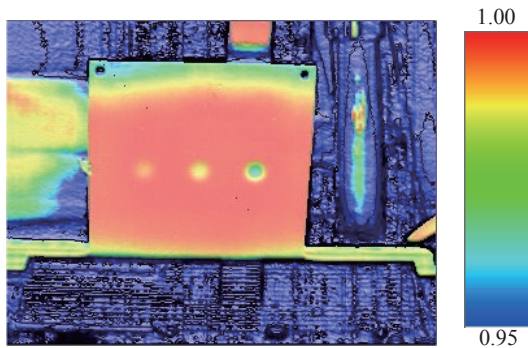


Fig.10 Correlation coefficient distribution on thermal image disturbance due to reflection, providing clear views of the defects.

### 3.2 Application to actual pipes

Fig.11 shows an evaluation example of the wall-thinning distribution of a pipe used in an actual plant. The measured part included wall thinning that had been repaired from the outside. There, however, was a possibility of the repaired area not covering the entire area with a thinned wall. Thus the present technique was used for the evaluation. When taking thermal images, no processing was done on the measurement surface to convert it to a quasi-blackbody, since adhered dust and the like can lead to the same effect as the quasi-blackbody processing. Fig.11 (b) is a thermal image taken by an infrared thermographic camera set up almost directly facing the repaired area. Here, the repaired area exhibits an apparent surface temperature that measured significantly higher than its periphery. This results in a low contrast in the periphery of the repaired area. Also, since a halogen heater was used, uneven thermal flux in the irradiated area resulted in uneven heating. The thermal image includes the influence of these factors as disturbance. Therefore, in Fig.11 (b) alone, it was difficult to detect the minute change of surface temperature caused by wall thinning. Fig.11 (c) shows an image after processing the correlation coefficient, in which a defect-free point indicated by an arrow in Fig.11 (b) was selected from the pixels exhibiting temperature changes greater than  $5^{\circ}\text{C}$  caused by the heating. The processing of the correlation coefficient normalizes the chronological temperature change, reducing the effect of uneven heating caused by the halogen heater. As a result, the area suspected to have undergone wall thinning is clearly shown in the periphery of the repaired area. The wall thickness was measured on a later day by an ultrasonic thickness gauge, which confirmed how wall thinning occurred smoothly towards the repaired area. At that time, the wall thickness at point "a" was

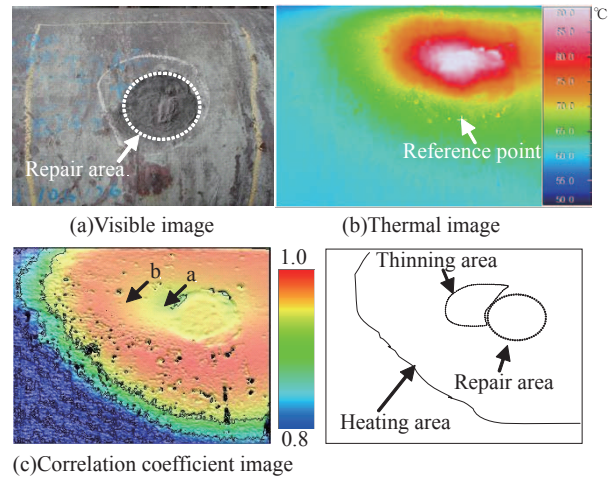


Fig.11 Example of pipe measurement

approximately 13% of the defect-free point, while the wall thickness at point "b", neighboring point "a", was approximately 45% of the defect-free point. This result confirms that determining the correlation coefficient distribution allows the detection of the part with significant wall thinning. The future plan includes a study on the effect of sludge inside a pipe, the pipe surface and the like, on the surface temperature, so as to expand the applicability of this detection method.

### Conclusions

A screening method was proposed in order to efficiently confirm the soundness of gas pipes used in steelmaking plants. This method is based on triage techniques employed in the medical field and uses the test results obtained by an infrared thermographic camera and ultrasonic thickness gauge as determination criteria. Aiming at evaluating the wall thinning caused by aqueous corrosion due to sludge in pipes, an infrared thermographic camera was used to conduct studies to find a method for detecting sludge inside a pipe and a method for measuring the distribution of wall thinning. Testing conditions, signal processing, etc., were developed and adapted for actual pipes, and their validity was confirmed.

### References

- 1) T. Sakagami. *Petrotech*. 2009, Vol.32, No.3, p.153.
- 2) Saga EMS conference, Disaster task force, Disaster medical manual workgroup, *Disaster Medical Response Manual, Saga prefecture*. 2003, pp.29-42.
- 3) T. Sakagami et al. *Proceedings of the 15th JSME design and systems division conference*. 2005, pp.480-481.
- 4) JSNDI Ad Hoc Research and Technical Committee on Thermography. *Handbook of nondestructive testing*. 2004, pp.169-175.



# Machining Technology for Large Impellers of Centrifugal Compressors

Toru KAINO \*1

\*1 Takasago Machining & Instrumentation Assembly Dept., Machinery Center, Machinery Business

*The impellers of centrifugal compressors are becoming larger, requiring machining efficiency to be improved in accordance with the characteristics of 5-axis machining centers and work shapes. Now, the machining time has been reduced by using contour machining, a cutting-resistance-leveling system and a method for predicting chatter vibrations. This paper describes the recent measures taken to improve the machining of large impellers.*

## Introduction

Recently, the centrifugal compressors used for air-separation units, for example, have been increasing in size and the demand for them is growing. Accordingly, their impellers, the major components, are becoming larger, requiring a long machining time. Hence, the reduction of machining time is an urgent issue in preventing extended delivery times and avoiding a high milling cost.

The impellers of centrifugal compressors rotate at high speeds and must be both highly accurate and strong. Hence, they are mainly shaped by machining. An impeller has blades, each twisted three-dimensionally into a complex shape extending over an adjacent blade in order to achieve a high pressure ratio and high efficiency. These impellers are difficult to machine with the simultaneous 3-axis/4-axis control machining centers generally used for die machining and require machining by simultaneous 5-axis control machining centers.

In an attempt to select a machining method that matches the characteristics of simultaneous 5-axis control machining centers and the work shapes, thus developing a highly efficient method for machining larger impellers, Kobe Steel has adopted simulation technology, which has grown remarkably in recent years. The following is an outline of the machining technology worked on recently.

## 1. Machining of impeller blades

The shapes of impeller blades are determined optimally after repeating fluid performance analysis, strength/vibration analysis, etc., so as to satisfy all the required specifications from the aspects of performance, strength, vibration and structure. A solid model with typical impeller shape and the names of impeller parts are shown in Fig. 1.

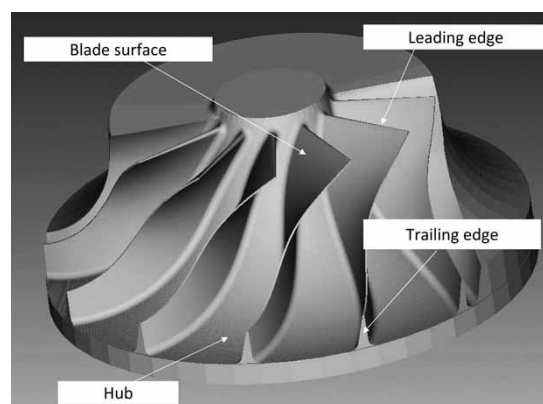


Fig. 1 Solid model of impeller

Free-form surfaces, such as those of impellers, are machined by simultaneous 5-axis machining centers. Simultaneous 5-axis machining centers feature three linear axes and two rotary axes, which are simultaneously controlled in order to adjust the tool attitude as needed to enable the machining of parts with complex 3-dimensional shapes. On the other hand, the 3-dimensional interference between a tool (principal axis) and work/jig must be taken into account, and tool loci must be determined so as to avoid machining at the dead point of each ball end mill, the point at which the circumferential speed of the cutting edge at the tip becomes zero. This makes the preparation of NC programs especially difficult.

Impeller materials include stainless steel that is mainly selected for its strength and corrosion resistance. For example, a titanium alloy with a high specific strength is used for impellers that run at high circumferential speeds. Stainless steel and titanium alloy have poor machinability and are generally referred to as difficult-to-cut materials. In addition, they have thermal conductivities lower than those of other steels, which leads to cutting heat accumulating on the cutting tips, accelerating the deterioration of the tool tips and shortening the tool life. This also adversely affects the finish accuracy of the work piece.

The following summarizes the problems with impeller blade machining:

- i) Machining a 3-dimensional shape involves a constantly changing cutting depth and varying cutting resistance.
- ii) Structurally, simultaneous 5-axis machining centers have low machine stiffness around their rotary axes and are generally not suitable for

heavy cutting.

- iii) Each work piece has a thin shape and, in addition, long tools are used, which promotes chatter vibration, making it difficult to increase the machining speed.

The following measures were taken to solve these problems and to improve the machining efficiency. They are, respectively, i) adopting a technique for leveling cutting resistance, ii) adopting contour machining, and iii) using a tool with variable pitch and variable lead angle and adopting a prediction technique for chatter vibration. The following is an outline of what has been done.

## 2. Measures for improving rough-machining efficiency of impeller blades

### 2.1 Technique for leveling cutting resistance

Conventionally, a tapered ball end mill made of high-speed steel as shown in Fig. 2 was used for the rough machining of impeller blades. As impellers have become larger, the tools for rough machining have increased in size, accompanying an increased cutting depth and, consequently, increased cutting resistance. This has made machines more likely to stop due to overloading and caused tools to break during machining. As a result, machining conditions such as the cutting depth and feed rate must be eased, making it difficult to improve machining efficiency by simply using larger tools.

A possible cause of tool breakage, other than increased cutting depth and the associated increase in cutting resistance, is the increased tool length, adapted in order to avoid interference between a work piece and the machine during the machining of impeller blades. Such a tool is more likely to deflect. In addition, the machining of complex 3-dimensional shapes such as impellers involves a cutting depth and tool attitude that change constantly, along with a constant change in cutting resistance. To prevent tools from breaking, machining must be performed under cutting conditions that are eased to maintain the resistance as low as possible, which poses the problem of increased machining time.

Hence, in order to reduce the variation in cutting resistance, a technique for leveling cutting resistance has been adopted. A system adapting this technique is shown in Fig. 3. This system employs a cutting-resistance model in accordance with the materials, tool-shape data, a material shape model and an NC program (tool loci) to geometrically calculate the amount of contact between the material and tool. This enables the calculation of cutting resistance in chronological order.

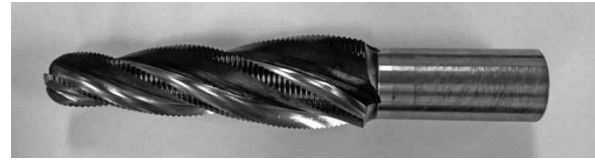


Fig. 2 Tapered ball end mill made of high-speed steel for roughening

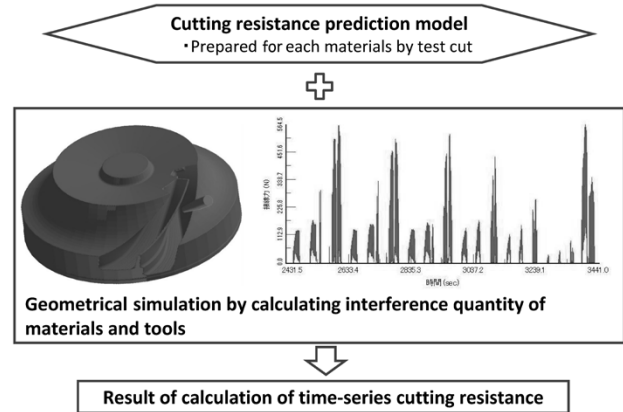


Fig. 3 Conceptual diagram of cutting-resistance-leveling system

In addition, inputting the threshold for maximum cutting resistance and executing recalculation enable the leveling of cutting resistance. This makes it possible to reduce the feed rate for portions with high cutting resistance in order to decrease the cutting resistance and to raise the feed rate for portions with low cutting resistance, which increases the cutting resistance. As a result, the variation in cutting resistance can now be suppressed without changing tool loci. An example of cutting-resistance leveling is shown in Fig. 4. It should be noted that the thresholds for cutting resistance have been compiled in a database after test machining in accordance with material, tool size and cutting depth.

This cutting-resistance leveling has stabilized the machining. As a result, the feed rate has been improved by approximately 60%, and the cutting depth has been increased by 25% in the radial direction and by approximately 30% in the axial direction. In addition, the stabilized variation in cutting resistance has decreased the risk of biting due to tool deflection and tool breakage, enabling the reduction of the allowance for finish machining from the conventional 2mm to 1mm. Hence, the finish machining time has also been reduced significantly.

### 2.2 Contour machining

Contour machining is used mainly for complex shapes such as dies. The machining is conducted

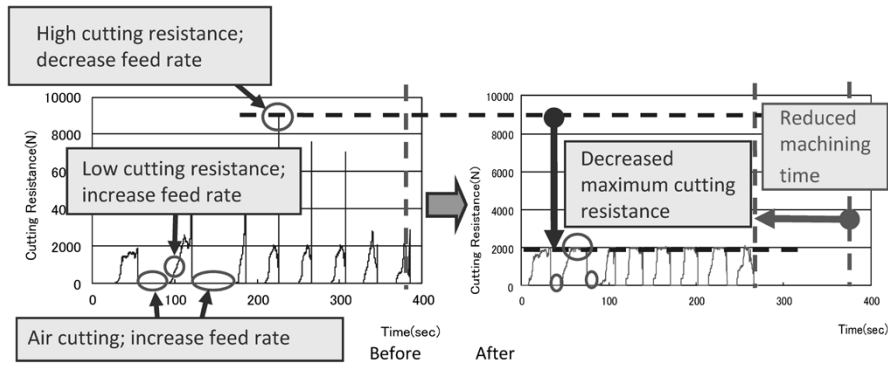


Fig. 4 Example of cutting-resistance leveling

while keeping a constant cutting depth in the axial direction and is thus accomplished with a small cutting depth and high feed rate, which enables highly efficient rough machining even for complex shapes. In such machining with a small cutting depth and high feed rate, more cutting resistance is imposed in the axial direction, or the direction of the principal axis of the machine, while decreasing the cutting resistance imposed in the radial direction. Therefore, even when tools with long protrusion are used, as in the machining of impeller blades, roughness failure due to the lack of tool rigidity can be avoided, as well as the deterioration of tool life; the result is highly efficient machining. In addition, 5-axis machines can run while fixing the rotary axes with low rigidity, which is expected to enable tools with long protrusion to be used with sufficient rigidity to ensure stable machining.

Although contour machining is expected to realize highly efficient machining, its application to impellers requires 3-dimensional determinations of machining ranges and optimum tool attitudes to prevent undercut while avoiding interference between complex-shaped blades and tools. In conventional computer aided machining (CAM), the angles of tool attitudes are roughly designated to prepare the passes for contour machining, and the adequacy of the machining range must be verified repeatedly, which makes it difficult to use conventional methods for preparing NC programs for contour machining. Fig. 5 shows an example of how a geometrical cutting surface is designed to determine the tool attitude.

On the other hand, the recent development of 3D-CAD/CAM has enabled the machining range and optimum tool attitude to be designated visually on 3D models, permitting the preparation and verification of optimum machining passes in a short period of time. This, as a result, has realized efficient machining with a small cutting depth and high feed rate along the surface shapes of blades for the maximum machining range.

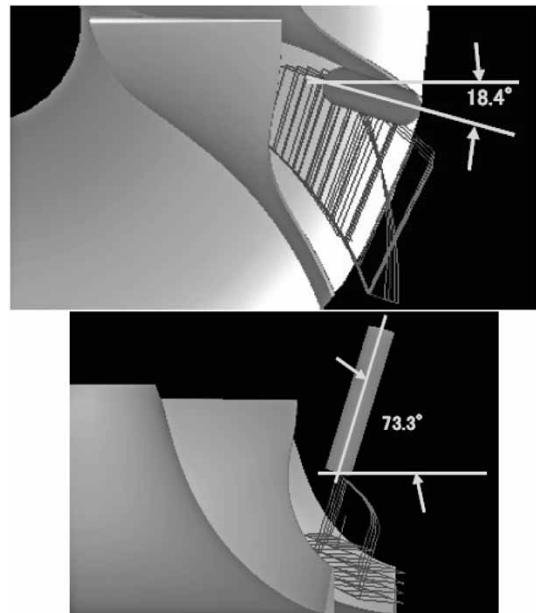


Fig. 5 Example of tool attitude

Compared with the conventional rough machining using a tapered ball end mill made of high-speed steel, machining with a small cutting depth and high feed rate results in a small cutting depth; however, the use of ultra-hard material for the cutting tip can increase the feed rate by a factor of 20 with an expected increase in the amount of chips discharged. On the other hand, due to the small cutting depth, the machining must be conducted with a tool with a rather large diameter. Therefore, a decision was made to adopt this method for the rough machining on the side of trailing edges, which have ample interspaces in between the blades.

Further, a radius cutter with a cutting tip made of ultra-hard material can now be used in place of the tapered ball end mill of high-speed steel used for conventional rough machining, which has shortened the machining time by 17% on average.

### 3. Measures for improving finish machining efficiency of impeller blades

#### 3.1 Tool with variable pitch and variable lead angle

Fig. 6 schematically shows the machining methods used on leading edges. Cutting with the lateral face of a tool (i.e., flank milling) reduces the number of passes and thus shortens the machining time; however, the lateral face of the tool comes in contact with each leading edge throughout its entire length all at the same time, which results in large cutting resistance. In addition, the work is thin-walled and possesses low rigidity, which causes chatter vibration around the leading edge; this poses a problem in obtaining favorable surface roughness. Therefore, thrust machining using the round chamfer at the tool tip (i.e., point milling) has been adapted to reduce the cutting resistance; this has increased the number of passes and decreased the machining efficiency.

To achieve highly efficient machining, a tool was developed for preventing chatter vibration during flank milling. There are two types of chatter vibration: namely, forced chatter vibration and self-excited chatter vibration. The large vibration that occurs during machining is mostly attributable to regenerative chatter vibration, a type of self-excited chatter vibration.

Fig. 7 shows the generation mechanism of chatter vibration during cutting. During cutting, the relative motion of the work piece and tool generates a slight unevenness on the cutting surface. In addition, the phase difference between the previously machined wavy surface and currently machined wavy surface causes the cutting thickness (i.e., amount of cutting: the interspace between the solid line and dashed line in the figure) to change periodically (Fig. 7a). This turns into a periodical variation in cutting resistance. Once this vibration exceeds a certain level, it begins to grow, leading to regenerative chatter vibration.

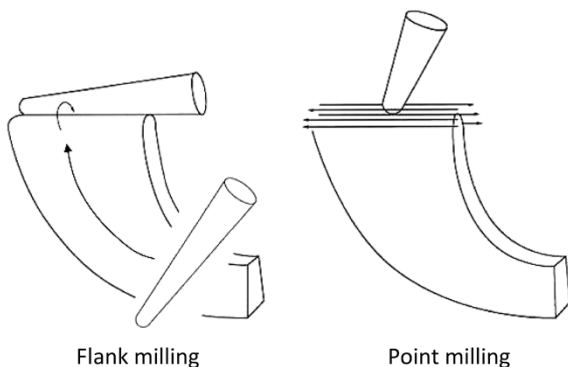


Fig. 6 Flank milling and point milling

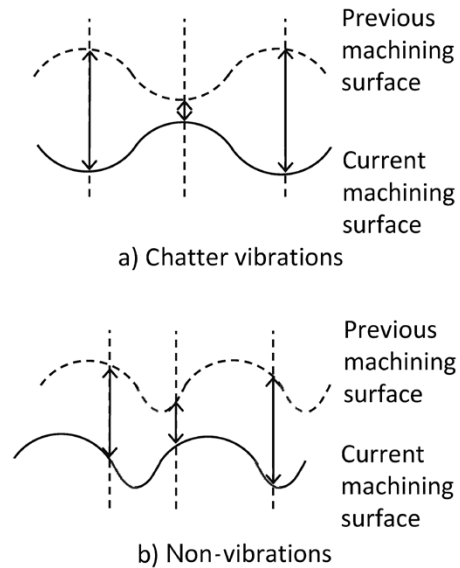


Fig. 7 Mechanism of chatter vibrations in cutting<sup>1)</sup>

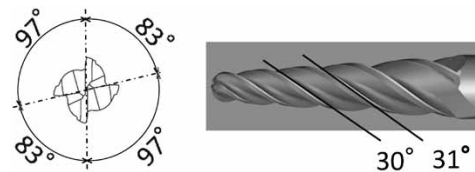


Fig. 8 Milling cutter with variable pitch and variable lead angle

In order to suppress this, it is effective to change the periodicity and/or the regularity of the cutting thickness by, for example, varying the cutting-edge intervals (Fig. 7b). This theory has been introduced into the development of a tool with variable pitch and variable lead angle for machining impeller blades. As a result, chatter vibration during the flank milling of the leading edges can now be prevented while yielding satisfactory surface roughness. Fig. 8 shows the tool with variable pitch and variable lead angle.

#### 3.2 Technique for predicting chatter vibration

Hub surfaces are machined using tools with long protrusion. Thus, an attempt to increase machining speed and/or cutting depth causes chatter vibration to occur, posing a problem in satisfying the surface roughness required. Hence, a study was conducted to adopt a technique for predicting chatter vibration in order to pursue optimum machining conditions for preventing chatter vibration and improving machining efficiency.

This technique predicts the theoretical limit of machining conditions that cause chatter vibration. For the material properties of the work piece, a preliminary 2-dimensional cutting experiment is conducted to determine the relationships among



the rake angle, tool tilt angle and cutting resistance value. Next, a cutting force model taking into account the geometrical relationship between the tool (cutting edge) and work piece is used to calculate the value of the cutting resistance. Meanwhile, in order to determine the dynamic characteristics of the tool and machine, the spring constant and viscosity coefficient of the system are determined by conducting excitation experiment of the end mill on the machine. The cutting force and the dynamic characteristics with a tool attached are used to predict the theoretical limit of machining conditions that cause chatter vibration.

In general, the tools used for machining impeller blades come in all different lengths, since they are repolished each time after use. On the other hand, the lengths of the tools used for hub surface machining remain unchanged, since they are of a shrink-fit type whose ball end mill at the tip can be changed, which means that a change of work piece does not affect the dynamic characteristics of the tool. Hence, this prediction technique has been adopted. **Fig. 9** shows a predicted curve for chatter vibration based on this technique. Adopting the technique for the prediction of chatter vibration has enabled an increase in the cutting depth in the axial direction from 0.4mm to 1mm and in the tool revolution from 1,280rpm to 3,200rpm to achieve machining without chattering.

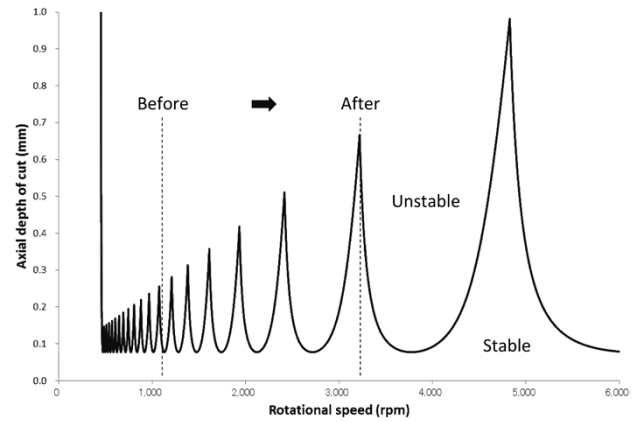


**Fig. 9** Improvement of cutting conditions by predicting chatter vibrations

## Conclusions

This paper has introduced the problems encountered during the machining of large impellers made by Kobe Steel. It has been demonstrated that these problems can be resolved by optimizing the tools, machining method and machining conditions for large impellers, thereby significantly shortening the machining time. Impellers are likely to become larger, and their machining is expected to become more challenging. Kobe Steel will strive to adopt state-of-the-art machining technologies while maintaining quality and shortening the machining time.

## References

- 1) A. Shibata. *NACHI TECHNICAL REPORT*. 2012, Vol.25, B2.

# Automatic Welding System for Crawler Crane Top and Bottom Booms

Akira OKAMOTO\*1, Masatoshi HIDA\*1, Tsutomu OONE\*1, Takemasa YAMASAKI\*1, Tatsuro ASANO\*2, Toshifumi KOBAYASHI\*2

\*1 Production Systems Research Laboratory, Technical Development Group

\*2 KOBELCO CRANES CO., LTD.

*An automatic welding system for upper and lower booms was developed at KOBELCO CRANES CO., LTD., aiming at stabilizing production capacity, achieving consistently high quality and increasing flexibility for varying work volumes. A technology was developed for reducing the man-hours spent in teaching tasks having to do with the weld lines of lattice pipes. Also developed was a sensor technology that enables copy welding by reliably detecting welding lines even during large-current welding, which generates large amounts of fume and spatter, and during welding on a specular reflection surface. This paper introduces these technologies.*

## Introduction

As the crane manufacturing business continues to globalize, our factory in Japan is required to function as a mother in pursuing world-class productivity (e.g., personnel saving) and quality, as well as to respond flexibly to varying work volumes. Our overseas factories, on the other hand, need, for example, to ensure welding quality as high as that achieved by the mother factory without relying on skilled welding experts.

In response to these requirements, Kobe Steel has worked to automate the process of welding lattice booms (i.e., insert booms, top booms and bottom booms), a process which has relied on the advanced skills of welding experts. Among these booms, the welding of the insert booms has been automated and implemented.<sup>1)-4)</sup> The top and bottom booms, however, have a greater number of joints than the insert booms and have many problems of their own, such as increased robot-teaching time.

Now, Kobe Steel has overcome these problems and automated the welding of top and bottom booms. This paper gives an outline of that achievement.

### 1. Problems in automating welding process for lattice-booms

The booms of crawler cranes have structures as shown in **Fig. 1**, in which pipes are arranged in lattices. (Such booms are hereinafter referred to as "lattice booms.") A crawler-crane boom generally consists of component booms that are roughly classified into 3 types: namely a top boom,

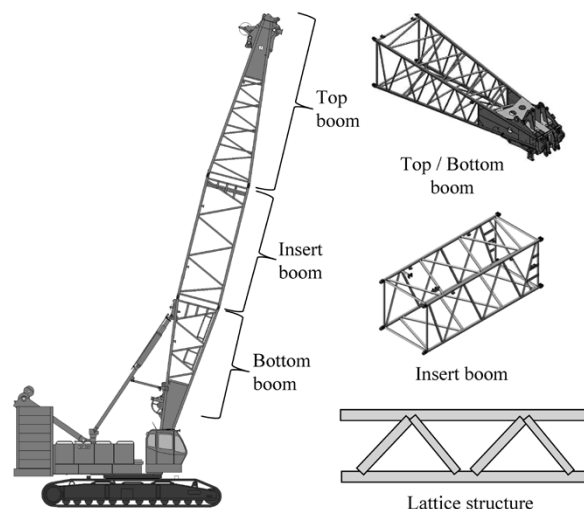


Fig. 1 Construction of booms for crawler crane

bottom boom and insert boom. The welding of a component consisting of pipes arranged in lattice structures involves welding joints, each of which consists of pipes with different wall thicknesses and has a saddle-shaped welding line whose direction continuously fluctuates between upward and downward. Therefore, the torch posture and electrode manipulation during welding must be controlled such that these saddle-shaped lines are copied, which requires high-level skills.

During the automatic welding of these lattice booms, long booms are subjected to thermal strain, and assembly errors occur. This renders indispensable a copy welding in which the groove positions of welded portions are continuously detected. A pipe-to-pipe joint with a complex saddle shape causes its contour to change continuously, which makes it difficult to use the conventional function of arc copying. As for insert booms, Kobe Steel has developed a unique logic for detecting the weld lines in lattice pipe joints to realize the copying function. As shown in **Fig. 2** (right), this logic has been combined with commercially available hardware having a welding range sensor to realize automatic welding. This automatic welding has been implemented in real machines. An insert boom of interest has a parallel structure in which a joint shape with the same crossing angle is repeated. All of its joints are pipe-to-pipe joints. Therefore, as shown in **Fig. 2** (left), the total number of objects for

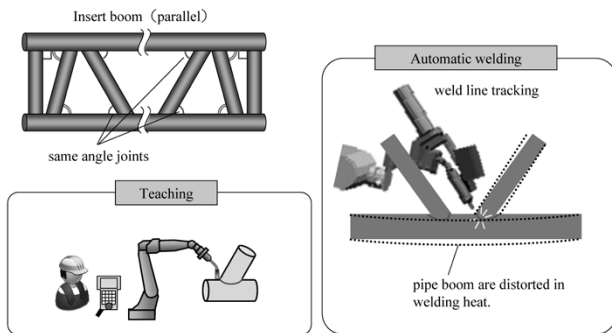
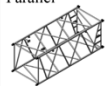




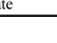


Fig. 2 Current status of automating process of insert boom

Table 1 Differences among booms (top, insert and bottom)

	Boom shape	Welded joint	Welding current	Number of booms	Number of joints
Insert boom	Parallel 	Pipe+Pipe  10joints/boom	180A	7	7×10=70
Top boom	Taper 	Pipe+Pipe  20joints/boom	180A	44	44×20=880
Bottom Boom		Pipe+Plate  Plate+Plate 	250A		

a robot-teaching task is relatively small, 70 joints (i.e., 7 types × 10 joints/type), making individual teaching possible.

On the other hand, there are more types of designs for the top and bottom booms, which caused the following problems (Table 1).

Problem I: An increased number of joint shapes increases the man-hours spent in teaching:

Each boom has a tapered structure, and the crossing angles of the pipes are all different. Moreover, each type of boom has 20 pipe-to-pipe joints on average. Therefore, there are as many as 880 joints (44 types × 20 joints/types) that require individual teaching. As a result, the man-hours spent in teaching have significantly increased compared with the time spent on insert booms, which has hindered automation.

Problem II: Difficulty in detecting weld lines:

In addition to pipe-to-pipe joints, top and bottom booms inherently have pipe-to-plate and plate-to-plate joints. The grooves for the welded portions of plates are often machined to a specular finish. These specular surfaces reflect the laser beam emitted from commercially available welding range sensors, making it difficult in many cases to detect weld lines in a stable manner. Further, since high-current welding is performed with weaving, welding positions must be detected stably even during weaving in environments

with spatter and fume.

## 2. Technology for supporting preparation of teaching data for lattice booms

Top and bottom booms have tapered structures and there are as many as 880 types of joints to be taught. The task of teaching this many joints requires advanced know-how of welding and is not a task that can be done by just anyone. Even a skilled operator must spend one hour per joint and would have to spend several months to complete the teaching task in order to cover all the types of booms. It was against this background that Kobe Steel developed a method for preparing teaching data by calculating saddle-shaped curves on the basis of their geometrical information, while reflecting operators' know-how. In addition, in order to enable the execution of the teaching data prepared by a computer without correction in real machines, a method was devised for efficiently correcting for the equipment differences among the robots.

### 2.1 Method for preparing teaching data reflecting operators' know-how

The insert booms, for which automation has been implemented, have 70 joints in total and the teaching data prepared for these joints have been put into a database. For a joint with established teaching data, the position is parallel-shifted to be reutilized. For new types of joints, on the other hand, a method has been established which comprises extracting (or copying) the approximating data while considering the ease of correction tasks for real machines, and preparing provisional teaching points, each located slightly away from the welding line, so as to avoid the interference of the wire tip with the pipe, thereby supporting the task of editing the teaching data.

In the case of insert booms, the combinations of pipe diameters and the allowable range of crossing angles, for example, are limited; hence the convenient methods described above will work. In the cases of top and bottom booms, however, there are so many combinations of geometrical information determining the shapes of the pipe joints (e.g., main-pipe diameters, lattice-pipe diameters and crossing angles) that most data must be newly prepared. Therefore, it was known that the method used for insert booms, including correcting the approximating data, would result in several months of teaching.

During pipe welding, the torch tip must aim at a position that is shifted a predetermined amount away from the saddle-shaped curve that

is to become a pipe-to-pipe joint. Moreover, the ever-changing groove angle and welding direction (upward/downward) during welding require timely and appropriate changes in torch-aiming angle, electric current/voltage, welding speed and electrode manipulation, calling for highly advanced skills.

Hence, the newly developed method for teaching-data preparation calculates the saddle-shaped curves, which are to become weld lines, on the basis of geometrical information on the pipe joints. To appropriately aim at a welding position along the curve, the aim position is made shiftable outward along the main pipes in the radial direction. In order to control the beads in overlap positions as shown in Fig. 3 (left), the amount and range of this shift are made specifiable, as shown in Fig. 3 (right), such that operators can adjust them for each joint.

As for the welding work know-how (e.g., the aiming angle, electric current, voltage and welding speed) of skilled welding experts, "appropriate teaching data" are first extracted from the database of collected teaching data, as shown in Fig. 4. Next,

the welding work know-how, including aiming angle, electric current/voltage and welding speed of the extracted teaching data, is applied to the aim position that reflects the amount of shift away from the saddle-shaped curve calculated in advance. The method for extracting "appropriate teaching data" includes applying a spatial filter to all the geometrical data, e.g., pipe diameter ratios (lattice-pipe diameter/main-pipe diameter) and crossing angles, to avoid interference between the robot and pipes and selecting teaching data in numerical distances based on the geometrical information for the pipes.

As the teaching task proceeds as a whole, the accumulated amount of teaching data increases. This enhances the precision of the teaching data extracted, gradually decreasing the amount of correction work for welding. The above technique has been developed with the aim of reducing the time spent on teaching tasks. However, with a sufficient amount of accumulated teaching data, the welding tasks can now be accomplished with simple test operation with minor correction; as a secondary effect, this enables unskilled operators to perform the teaching tasks. Instead of formulating rules by extracting teaching know-how per se, the present technique allows teaching data, containing know-how, to be used for actual teaching as soon as the data is registered in the database. This is an advantage of the present technique. In the future, this technique can be used without any problems even when the method of welding is greatly changed due to technological innovation, for example.

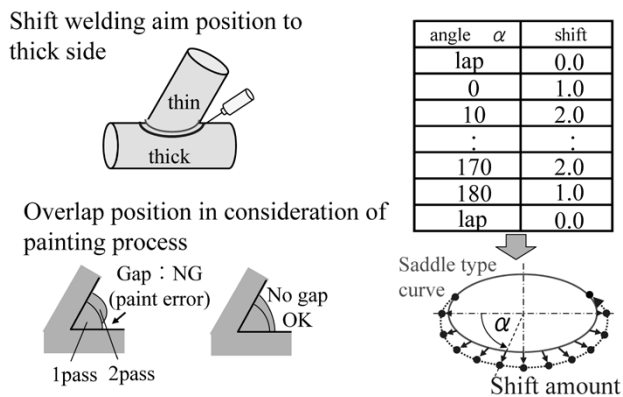


Fig. 3 Utilization of welding know-how (example)

## 2.2 Efficient method of correcting for equipment differences among robots

The method described in the previous section allows the preparation of teaching data reflecting welding work know-how, however, the data cannot be executed as-is in the real robots. This is because there is an equipment difference (error) between the virtual robot in a computer and real robots. The "gap" must be corrected. Executing the teaching program generated in a computer on a real robot may result in a gap of several millimeters. This is mainly attributable to errors from the design values of, for example, the parallelisms, perpendicularities, positions of robot joints, and the length of robot links (Fig. 5 (left)). The copying accuracy aimed at for weld lines is  $\pm 0.5\text{mm}$  or better. Considering the errors that occur during operation, including the resolution and accuracy of the welding range sensor, the correction of errors caused by the equipment differences among robots must aim at  $\pm 0.2\text{mm}$  or

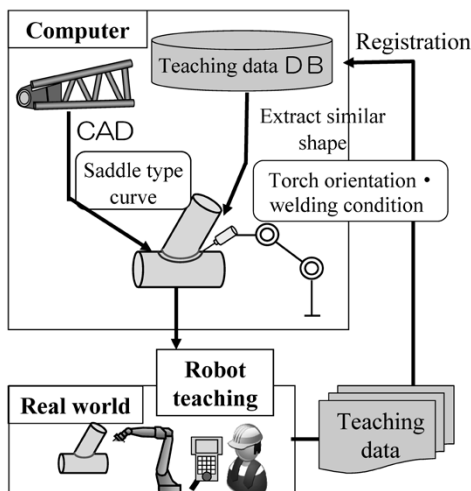


Fig. 4 Data-generation support for teaching robot welding pipe booms



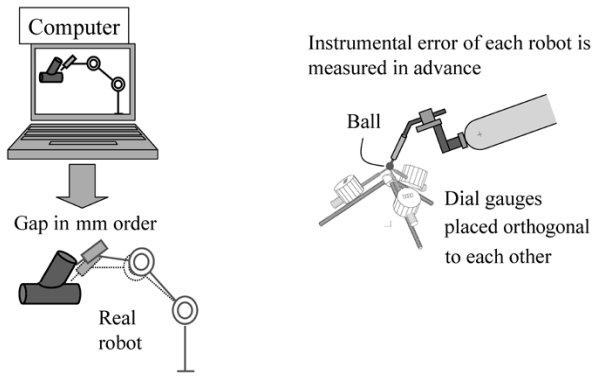


Fig. 5 Measuring equipment difference of robot

better.

One of the methods for correcting for the equipment differences among robots includes deriving link parameters, i.e., an error factor of robot joints as described above. However, since there are other error factors (e.g., deflection of the link due to gravity and gear backlash) that cannot be accounted for by the link parameters, it is difficult to reduce the robot tip error to 1mm or smaller while the position and posture are being changed in the space range of robot motion. Accordingly, in order to achieve an accuracy of  $\pm 0.2\text{mm}$ , it is more realistic to use a method of correction by directly measuring the error for each position and posture.

It is not realistic to measure errors for the motion space of a robot with 6 degrees of freedom. Hence, the equipment was reviewed, from its planning and designing stage, so that the welded part of each pipe always stays in the same position when viewed from the robot. The motion range of the robot during pipe welding was thereby restricted. The rotation angle around the welding torch is a posture angle that does not affect the welding operation. Therefore, this rotation angle was set at a predetermined value to decrease the degrees of freedom for the posture angles whose errors are to be measured. Accordingly, the errors were measured in a space that restricts the range of positions and postures that can be taken during pipe welding. The measurement method includes setting up three dial gauges arranged in directions orthogonal to each other, as shown in Fig. 5 (right), and attaching a spherical measurement probe to the tip of the robot, thereby measuring the size of the gap at the tip due to the change of posture in the 2 degrees of freedom (i.e., the angle of incidence and horizontal angle in a polar coordinate system with the pole at the probe tip). This measurement was conducted at the 8 corners of a cuboidal space (front to back;  $50\text{mm} \times$  left to right;  $100\text{mm} \times$  top to bottom;  $30\text{mm}$ ) that can roughly enclose the saddle-shaped curve of

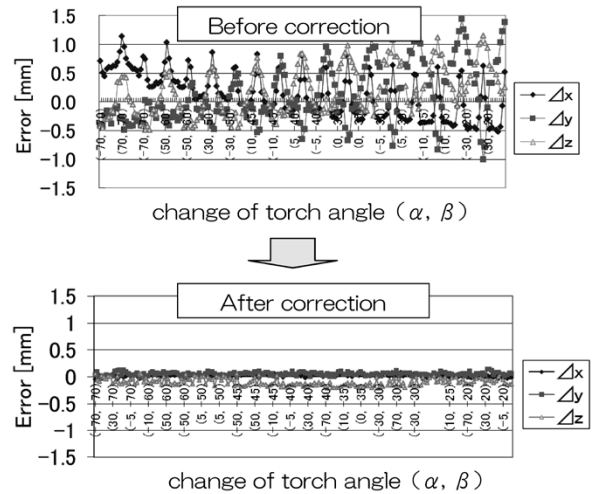


Fig. 6 Measuring change of torch angle before and after error correction

a maximum-sized pipe (Fig. 6). The errors measured in this space were used to correct the tip position. The results are shown in Fig. 6 (bottom). The results indicate that the errors can be corrected to  $0.2\text{mm}$  or better in all the x, y, z directions, as originally aimed at.

The teaching data, prepared in accordance with the above method, were thus corrected to achieve the target correction accuracy. This, as a result, eliminated the need for correcting for errors in the prepared teaching data, the errors that were due to differences among the machines. Moreover, the operation orbit of a robot can now be verified by a simple operation check. Thus, the time for correcting teaching data for real machines has been successfully and significantly reduced.

### 3. Technology for detecting welding positions compatible with mirror-surfaced works and weaving

Top and bottom booms are unique in that they have pipe-to-plate and plate-to-plate joints. This poses a problem: Irradiating a laser beam from a range sensor onto mirror-finished groove surfaces causes multiple reflections, which destabilize the detection of the welding position. An optical arrangement was specified to enable a separation between the normal light-section line and multi-reflected lights, which was reflected in the design of a sensor. Meanwhile, an image processing technique was developed for extracting the normal light-section line while taking into account its continuity. This has led to the development of a technology for detecting welding positions, which allows stable measurement of the groove shape.

### 3.1 Range sensor compatible with multiple reflection of laser beam

Fig. 7 depicts a range sensor for V-groove welding. The sensor includes a CCD camera and laser unit, both attached to the tip of the arm of the welding robot. A light is irradiated onto a groove joint for light sectioning. The photo images taken by the camera are used for measuring the distance from the groove joint and for determining the joint shape, on the basis of the triangulation principle. The sensor recognizes the weld line, and copy welding is performed while making corrections to the pre-taught positions. As shown in Fig. 8 (1), no multiple reflection occurs on diffusing surfaces, or on surfaces that cause diffused reflection, e.g., rust and paint; so only the clear image of the regular light-section line is left. On the other hand, as shown in Fig. 8 (2), a mirror surface, which, due to machining or for some other reason, causes specular reflection of light, causes multiple reflection of the laser beam, making it difficult to separate the regular light-section lines.

As described, the plate-plate joints, found in top and bottom booms, cause mixing of the regular light-section lines to be detected with multiple reflection components, making it difficult to stably detect the

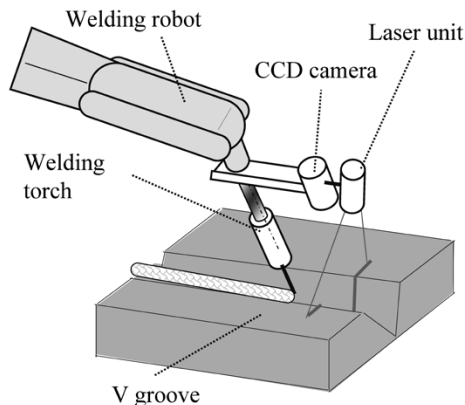
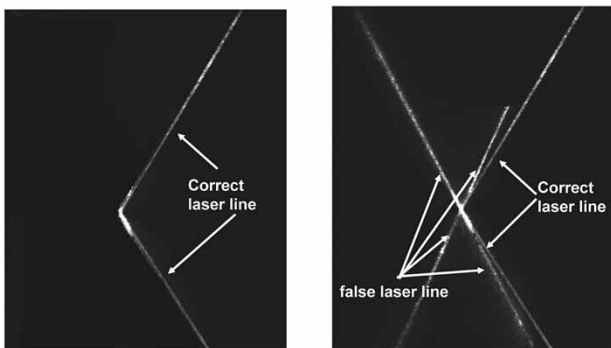


Fig. 7 Welding robot with range sensor



(1) Scattering surface on v-groove (2) Reflection surface on v-groove

Fig. 8 Light-section images (examples)

positions of weld lines. A typical range sensor that is commercially available for welding extracts a regular light-section line by devising its optical filters and image processing, but its detection capability is limited. It is against this background that Kobe Steel developed a welding range sensor incorporating a unique technique for detecting the positions of weld lines.

#### 3.1.1 Image simulation of light-section line

Fig. 9 shows the configuration of a welding range sensor. As shown in this figure, a camera and a laser unit are disposed on a plane determined by two lines, i.e., a bisector line of the groove angle  $\theta$  ( $\theta = 90$  degrees for fillet weld joint) and the weld line. A laser slit beam is irradiated perpendicularly to the weld line. Here, the laser projection angle is designated as  $\alpha$ , and the camera angle as  $\beta$ .

When both welded members have diffusing surfaces, there is no multiple reflection of the laser slit beam. As a result, the image taken by the camera is as shown in Fig.10 (1).

When one welded member has a diffusing surface and the other has a specular reflection surface, two laser slits appear, as shown in Fig.10 (2), due to multiple reflection (secondary reflection). One of the two is a laser slit beam A', which is the reflection of the laser slit beam A on the specular surface of the welded member B. Since this laser slit beam A' is an image of the laser slit beam A reflected from the mirror surface, the position of laser slit beam A' depends on the position from which it is viewed, or on the position of the camera. The other is laser slit beam B'', which is caused by laser slit beam B specularly reflected on the mirror surface of the welded member B and is irradiated onto a diffusing surface of welded member A. Since this laser slit beam B'' is diffusely reflected by the welded member

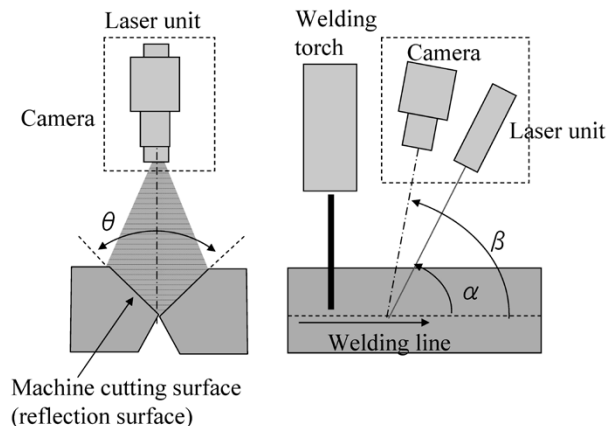


Fig. 9 Configuration of range sensor for welding

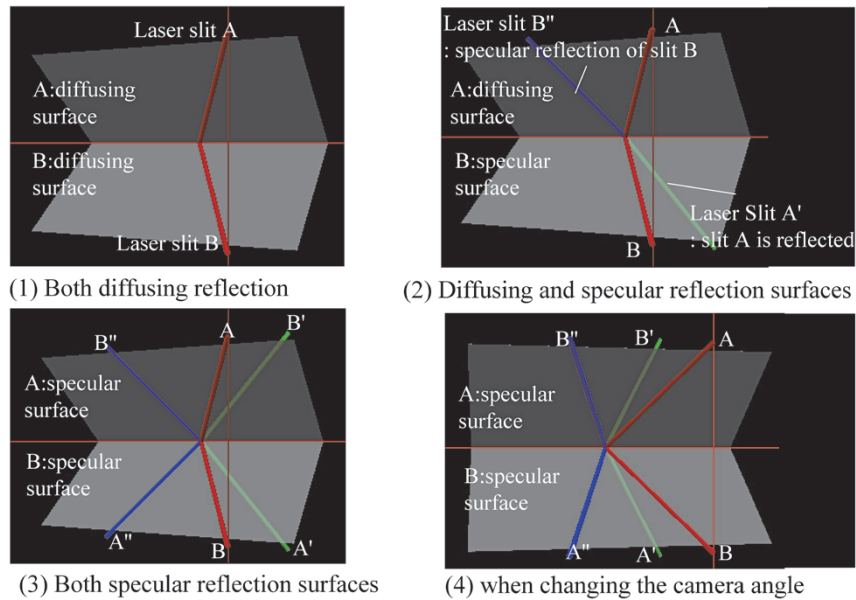


Fig.10 Appearance of secondary reflection image

A, its visual position does not change, regardless of the camera position.

Next, when both welded members have mirror surfaces, four laser slit beams appear as a result of secondary reflection, as shown in Fig.10 (3). These are, namely, laser slit beams A' and B', reflected on the mirror surfaces of welded members, and laser slit beams A'' and B'', specularly reflected on the mirror surfaces.

The photos (1), (2) and (3) of Fig.10 show the view from a camera angle  $\beta$ . Increasing the camera angle  $\beta$  reverses the positions of "slit beam A and slit beam B" and "slit beam A' and slit B'." Fig.10 (4) shows a view of the reversed positions.

As described, when a welding range sensor is disposed with a laser projection angle  $\alpha$  and camera angle  $\beta$  against a welded joint with a groove angle  $\theta$ , light-section lines captured by a camera, the lines including secondary reflection, can be calculated by simulation. Assuming  $\theta$  to be 50 degrees and  $\alpha$  to be 60 degrees, the relationship between the camera angle  $\beta$  and apparent angle  $\gamma$  from the center of the image is graphed in Fig.11 (top). Separating the true light-section line, plotted in red in the graph, from the reflection of multiple-reflection components shown in green and blue, which are inseparable, is difficult for a camera disposed at an angle of, say,  $\beta = 70$  degrees. Moreover, the camera angle  $\beta$  cannot be made smaller, due to the downsizing of the casing and the restrictions imposed by equipment such as the welding torch. In other words, the optimum camera angle  $\beta$ , for ease in separating the true light-section line and for downsizing the range sensor, is found to be 80 degrees. Kobe Steel has limited the groove angle  $\theta$  of interest to approximately 50

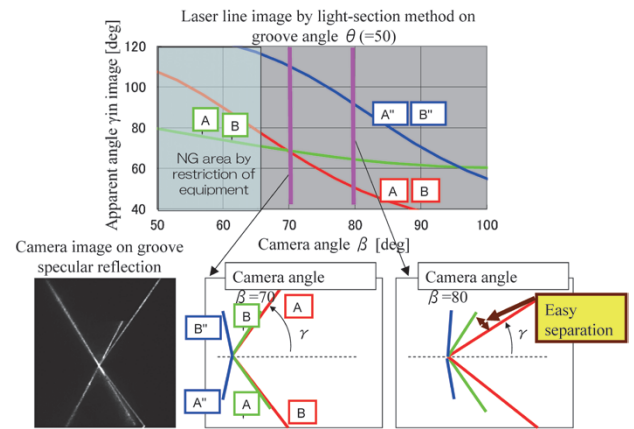


Fig.11 Appearance change of image in light-section method

degrees and thereby found an arrangement that facilitates the separation between the true light-section line and multiple reflection components in an image. That is, limiting the joints of interest enables us to determine the position of the sensor in which laser multiple reflection is unlikely to occur. This arrangement was used for designing a welding range sensor that enabled the stable detection of weld-line positions even on mirror surfaces.

### 3.2 Measures against contamination of protective window for sensors

High-current welding generates a large amount of spatter (metal spattered during welding) and fume (metal vapor). This contaminates the sensor-protecting windows through which the laser beam is irradiated and received. Thus the windows must be replaced periodically. Frequent replacement of

the protective windows imposes a significant burden on field workers. Since the level of contamination depends on the material of the protective windows, quartz glass, acrylic plate and polycarbonate were used here for the materials of a protective window, so as to compare the level of contamination. Welding was performed for 50 min with a welding current of 250A. The resulting levels of contamination on the protective windows are shown in Fig.12 (1). Polycarbonate was found to result in relatively small amount of adhered contamination. In addition, the light shielding plate was extended such that neither welding-arc light nor spatter directly hit the protective window. The light-shielding plate was also designed to prevent it from interfering with the pipes in narrow spaces. Fig.12 (2) shows the improved design. As shown in (2), the protective window results in almost no contamination.

### 3.3 Technique compatible with weaving for detecting light-section line

When the camera in a range sensor takes the image of welding that generates spatters (Fig.13 (1)), the spatters, with their high brightness, also appear in the image along with the light-section line of the laser beam. This makes the separation of the light-section line from spatter difficult, posing a problem in stable shape measurement (Fig.13 (2)). In captured images, the spatters move faster than the light-

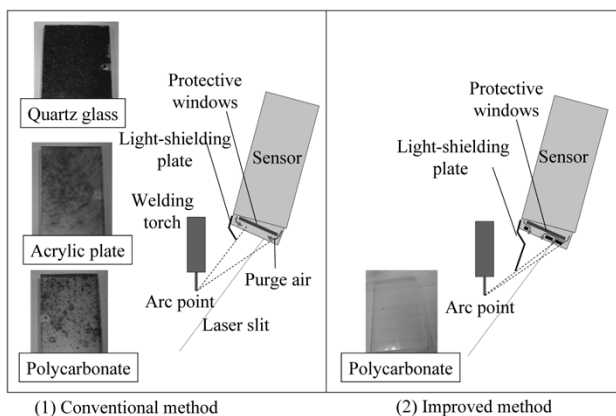


Fig.12 Dirt protection by protective window

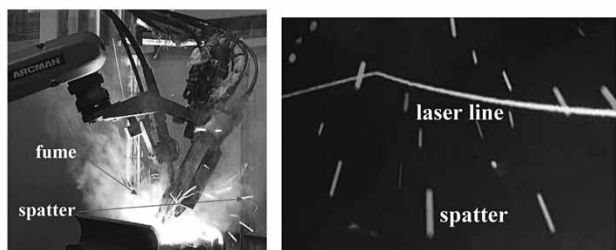


Fig.13 Spatter and fume during welding

section lines. Therefore, in a method for reducing erroneous detection caused by spatter, the focus was placed on the change in brightness in chronological images.

When there are  $K$  pieces of continuous images chronologically captured by a camera, the brightness of the images is designated as  $Image_1(i, j), \dots, Image_k(i, j)$ . Here,  $i$  and  $j$  represent the coordinates of the image (size:  $M \times N$  pixels). The average brightness,  $Image_0(i, j)$ , of the  $K$  pieces of images is given by Equation (1).

$$Image_0(i, j) = (Image_1(i, j) + \dots + Image_k(i, j)) / K \dots (1)$$

Averaging the brightness of the chronological images decreases the brightness of the spatter that moves faster. On the other hand, assuming that the shape of the welded joint does not change significantly, the brightness of the light-section line irradiated remains the same even after the averaging. Thus a decision was made to extract the light-section line using  $Image_0(i, j)$  generated. Fig.14 schematically illustrates a case where  $K = 3$ .

When averaging the brightness of images, however, the swinging motion of the sensor, as in weaving, causes the image of the light-section line to blur, causing a problem in stable detection; so focus was placed on the fact that the direction of flying spatters crosses the weaving direction orthogonally. Captured images that swing between left and right during weaving welding were compared in the weaving direction. This resulted in the development of a technique for detecting welding position that allows a more stable measurement of groove shape.

The image comparison was based on the sum of absolute difference (SAD), which represents the degree of similarity among the images. Taking  $Image_1(i, j)$  as a reference, the SADs of the chronological images,  $Image_2(i, j), \dots, Image_k(i, j)$ , are expressed as follows.

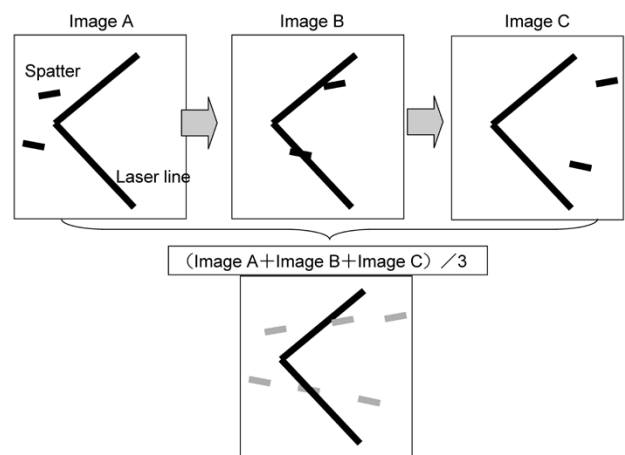


Fig.14 Welding-position-detection logic in spatter environment



$$\left. \begin{aligned} SAD_2 &= \sum_{j=0}^{M-1} \sum_{i=0}^{N-1} |Image_2(i, j - s_2) - Image_1(i, j)| \\ SAD_3 &= \sum_{j=0}^{M-1} \sum_{i=0}^{N-1} |Image_3(i, j - s_3) - Image_1(i, j)| \\ &\dots \\ SAD_K &= \sum_{j=0}^{M-1} \sum_{i=0}^{N-1} |Image_K(i, j - s_K) - Image_1(i, j)| \end{aligned} \right\} \dots (2)$$

Since the direction of weaving is fixed in most cases, the direction of image shift for image comparison can be restricted. This is expressed by  $S_2, \dots, S_K$  in Equation (2). The values for  $S_2, \dots, S_K$  that minimize the SAD are searched. Each image is shifted so as to roughly match the light-sectioning positions of  $Image_1(i, j), \dots, Image_K(i, j)$  with that of  $Image_1(i, j)$ . This enables the calculation of  $Image_0(i, j)$  according to Equation (1). The above logic is schematically illustrated in Fig.15 for  $K=3$ .

It should be noted, however, that calculating SADs for all the pixels slows down the processing. Hence, the light-section line was extracted here so as to calculate SAD only for the region of the light-section line. Thus the calculation region was restricted, shortening the calculation time and realizing copy welding in real time.

An example of the experimental results is shown in Fig.16. The joint of interest is a horizontal fillet, and the welding conditions include an

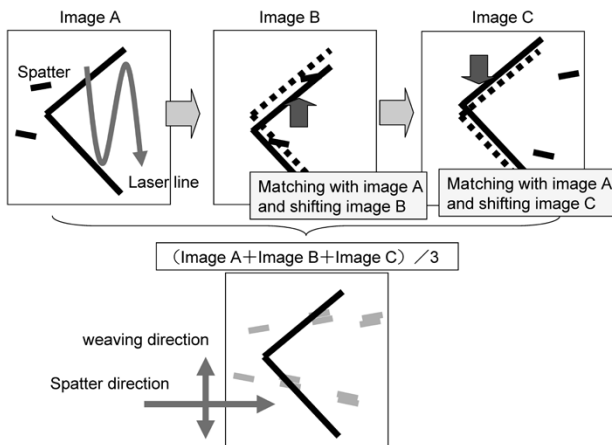


Fig.15 Logic for detecting welding position during weaving

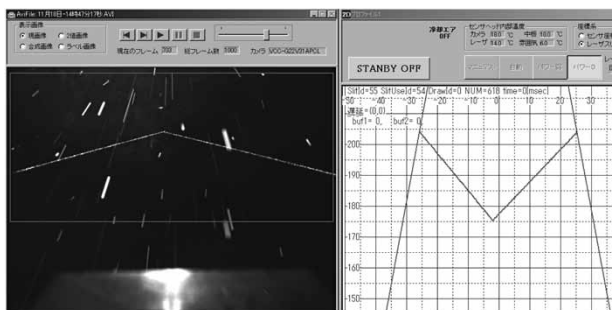


Fig.16 Example of sensor copying

electric current of 250A, voltage of 96% and speed of 40cm/min. A 100% rate of shape detection was accomplished even during weaving.

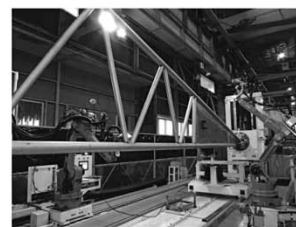
#### 4. Results of automatic welding

KOBELCO CRANES CO., LTD., and Kobe Steel have collaborated in establishing an automatic welding system for top and bottom booms. The system includes a welding robot, positioner, slider and copying sensor, and was installed in a factory for KOBELCO CRANES (Fig.17 (1)).

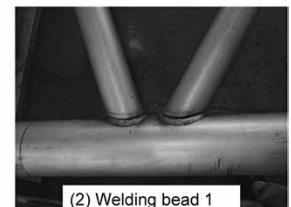
The establishment of this system has enabled the preparation of teaching data, with a high degree of completion, reflecting the know-how of skilled welding experts. Correcting for the differences among robots, i.e., the equipment error occurring in real machines, halved the time spent in teaching tasks at the machine side. In addition, even unskilled welders can now prepare teaching data with quality as high as that achieved by skilled welding experts. This has facilitated staffing and thus has shortened the teaching time during model changes.

Top and bottom booms have unique weld lines that are difficult to detect. However, the newly established technique for detecting welding positions has been made compatible with mirror surfaces and with weaving in adverse environments involving spatter and fume, which has enabled copy welding.

Moreover, a new technique has been developed for detecting the displacement of work during plate welding, a technique indispensable for top and bottom booms. The copying for multi-layer welding has also been contemplated. Thus automation has been achieved to enable welding with stability and high quality. A copying accuracy of 0.5mm or better has been accomplished at the tip, ensuring the stability of welding. Figs.17 (2) and (3) show the appearance of welds actually prepared using this system.



(1) Automatic welding robot system



(2) Welding bead 1



(3) Welding bead 2

Fig.17 Automatic welding system and welding beads

## Conclusions

Automation has been achieved for welding top and bottom booms, which will reduce the man-hours spent in teaching even when a model change is needed for pipe booms in the future. It also has enabled a vertical ramp-up of production lines. Further, in our overseas factories, the future increase in production volumes can be processed by automatic welding, rather than by skilled welding experts, by providing the core technology for welding automation in a black box. This technology will contribute to the establishment of a production

system that can respond quickly and appropriately to overseas demand, while contributing to the quality improvement of welding.

## References

- 1) M. Hida et al. *R&D Kobe Steel Engineering Reports*. 2007, Vol.57, No.1, pp.86-89.
- 2) M. Hida et al. *Proceedings for the 22nd annual conference of the robotics society of Japan*. The Robotics Society of Japan, 2004, p.227.
- 3) M. Hida et al. *Welding Technology*, September 2009. Sanpo Publication.
- 4) T. Yamashita et al. *R&D Kobe Steel Engineering Reports*. 2012, Vol.62, No.1, pp.87-90.

# Global e-learning System for Technical Support Engineers

Youichirou Sou\*<sup>1</sup>, Masashi YAMAKOSHI\*<sup>2</sup>, Yoshihiro MURAKAMI\*<sup>2</sup>

\*<sup>1</sup> Production Systems Research Laboratory, Technical Development Group

\*<sup>2</sup> KOBELCO CONSTRUCTION MACHINERY CO., LTD.

*With the increasing globalization of business, Japanese manufacturers are trying to strengthen the system for managing after-sales service activities at overseas branches so as to make themselves stand out from competitors. For this purpose, securing and training engineers for technical support is one of the most important issues. KOBELCO CONSTRUCTION MACHINERY CO., LTD. (KCM), one of the most globalized companies in the Kobelco group, has deployed an e-learning service for training support engineers since 2009. Having released the e-learning service for Japanese engineers first, KCM has extended it to the overseas branches since 2011, and at the end of 2013, in approximately 20 countries, the e-learning service was effectively being used as a common platform for educating engineers. Through those experiences, this paper discusses the possibilities and challenges in the use of IT for grooming after-sales service technical support engineers in the overseas branches.*

## Introduction

With the rapid progress of globalization, manufacturers in Japan have moved their production bases overseas, and products made at home and abroad are being sold and used all over the world. Accordingly, in addition to establishing a system for local production (MONODZUKURI) and supply, establishing a structure for local after-sales service and support has become a key factor for the manufacturers in making them stand out from others to survive in the globalized market of the future.

KOBELCO CONSTRUCTION MACHINERY CO., LTD. (hereinafter referred to as "KCM") is the most globalized company in the Kobelco group. This paper introduces a system for training engineers to engage in global after-sales service based on information technology (IT), called e-learning (an education tool based on computers and networks). Referring to actual cases, it discusses the issues in training human resources for after-sales service at overseas branches, also taking up the possibility of further exploiting IT.

## 1. KCM's system for global after-sales service

KCM has a Customer Support Center, Sales

and Marketing Division that serves as a central base in Japan, and has established an after-sales support system for eight separate areas of the world. Worldwide, there are approximately 4,000 after-sales service engineers engaged in support work so that customers can use the high-performance, high-quality construction machinery produced by KCM comfortably on a daily basis. The training of these service engineers is conducted in dedicated training facilities and is based on special education curriculums. In 2009, the facilities in Japan started introducing e-learning in some parts of the curriculums. This method of instruction has also been disseminated to overseas branches since 2011. As of the end of 2013, an e-learning system is being provided to after-sales service engineers in about 20 different countries as a universal education tool. **Fig. 1** shows screen-shot examples of a multilingual e-learning system.

## 2. Examples of introducing e-learning at KCM

### 2.1 Method of introducing e-learning

In general, e-learning has been used for remote learning and correspondence education services that are based on digital learning materials provided by, for example, education companies; it has also been used as a tool for educating and training students and employees at colleges and companies, etc. The former use could be referred to as a "content-providing type" and the latter as an "educational/training-tool type." The e-learning used by KCM must have the functions and characteristics of both types.

Specifically, the Sales and Marketing Division of the Customer Support Center in Japan serves as the mother base for after-sales service around the world. It uses e-learning worldwide as a tool for simultaneously sending and providing information on common basic technologies and the most up-to-date maintenance technologies required for the maintenance checkups and servicing of the product (construction machinery).

Next, the local trainers who are actually in charge of educating and training local service engineers at local after-sales service branches use the training contents provided in the system by the mother base.

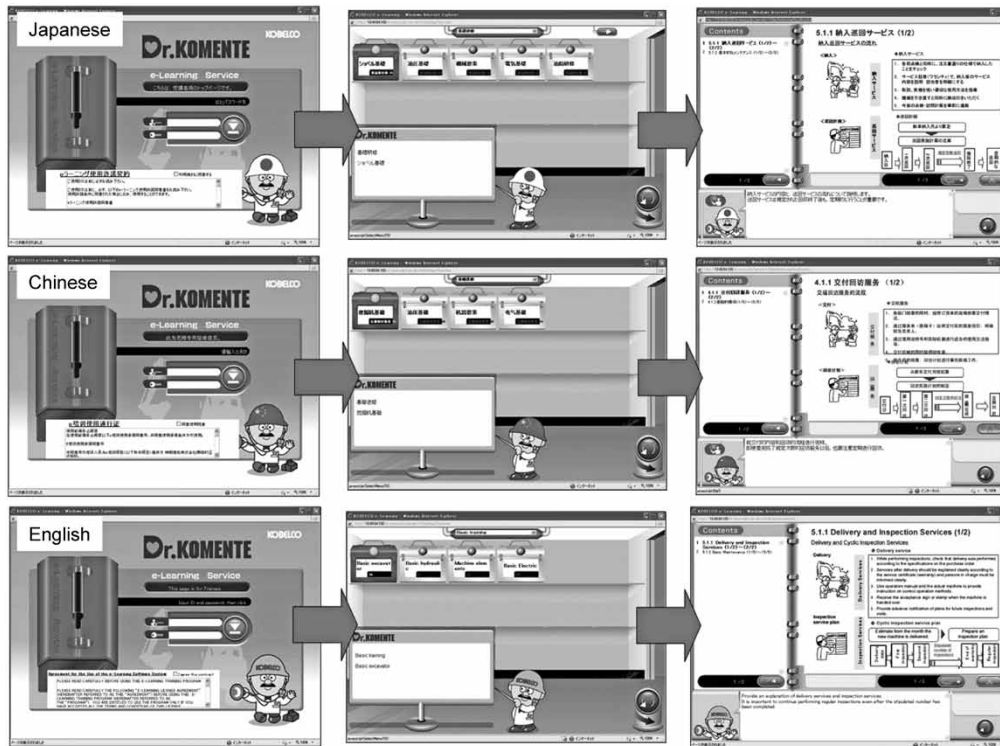


Fig. 1 Screen-shot examples of a universal e-learning system for technical support engineers

The system is thus exploited as a tool for educating local service engineers and training them effectively and efficiently.

## 2.2 Ways of introducing e-learning

### 2.2.1 Adoption of private cloud method

In order to use e-learning to provide content, as well as for education and training, KCM established an e-learning environment with a multilingual system based on a private cloud system using the internet. This has provided trainers at each branch with an e-learning environment dedicated to their branch so that they can use the education/training tool at their discretion.

### 2.2.2 Unitization with training program

This provision is not limited to use as an education/training tool, but extends to "universal" e-learning materials from the Customer Support Center at the mother base. A set of learning materials has been combined and compiled in a package in Japan and is provided as a suite of training programs. Local trainers can select necessary items from the suite in accordance with the actual situation at their branches. The programs can be followed in order, or else repeated.

### 2.2.3 Evaluation based on universal learning materials and index

As of the end of 2013, five types of universal learning materials had been prepared, comprising approximately fifty training programs. The training programs cover the "common basic technologies (1. Basic hydraulics, 2. Machine elements, 3. Basic electricity, and 4. Basic excavator)" required for maintenance checkups and servicing and "5. Product model training" (Table 1). The learning items in each training program are followed by a set of completion tests at the end, and it is so set up that all the questions must be answered correctly to complete each session of the training program. The system allows the trainers at each branch to confirm the results of the completion tests and attendance records. These can be used in a variety of ways, as determined by the branch. At a branch in China, for example, e-learning is treated as an education item that must be completed prior to group training at their local training facility: that is, the completion of e-learning is required for a trainee to participate in the group training. The trainers, on the other hand, check the results of the completion tests so that they can devise teaching methods for the group training.

Meanwhile, the system allows the Customer Support Center at the mother base in Japan to check on how many service engineers in each branch are participating in sessions using the learning



Table 1 Example of e-learning training programs

	Category	Title of e-learning training program (example)
Common basic technical field	①Basic hydraulic	(1)Construction machinery hydraulics: mechanism (2)Basic information on hydraulics (3)Pump overview/ Hydraulic pump input and output variability (4)Misc. (total 14 programs)
	②Machine elements	(1)Machine element and metallic material (2)Metalworking (3)Welding, flame cutting, penetrant test (4)Misc. (total 12 programs)
	③Basic electricity	(1)Electricity and electronics (2)General knowledge of electricity and electronics (3)General knowledge of electric and electronic parts (4)Misc. (total 9 programs)
	④Basic excavator	(1)Excavator outline (2)Hydraulic system (3)Construction machinery with Mechatronics (4)Misc. (total 17 programs)
	⑤Product model training	Special technical information about new product models

materials and suite of training programs provided from Japan, and to confirm how much they have understood. The universal learning materials and common evaluation index are used for confirming and evaluating the skills and knowledge levels of service engineers in each area.

### 3. The place and role of e-learning and its importance

#### 3.1 Issues in human resource development and the place of e-learning

In contrast to Japan, overseas branches for after-sales service are experiencing a higher rate of people leaving their jobs. This has created a human resource issue. Hence, overseas branches have a strategy of training as many novice service engineers as possible in a short period of time and selecting qualified persons from among them for further instruction. In Japan, the developing of human resources is usually accomplished through training for a certain period of time in a training facility. Meanwhile, for the instruction of service engineers at overseas branches, it is considered, at present, to be more cost effective to use IT to impart as much of the required knowledge as possible in a short period of time and to train and strengthen service personnel through field practice.

Our group companies, including KCM, have put e-learning into practice as a tool for assisting skill transfer at the manufacturing sites in Japan. In Japan, however, there is a custom of apprentice-style education and, in many cases, e-learning is regarded only as a supplementary tool for that education. In developing nations, on the other hand, there is a strong inclination toward obtaining skills and careers. Hence e-learning is likely to be used more

proactively there than in Japan and is functioning as an effective educational tool.

#### 3.2 Future possibilities of using IT and technical subjects

KCM plans to proceed further with globalization and needs, more than ever, to quickly start up an after-sales service system at newly established overseas branches, as well as to maintain and improve the technical quality of after-sales service on a global scale. In the meantime, the position and role of e-learning is continuing to change. Specifically, exploiting the characteristics of the education tool to achieve immediate and simultaneous effectivity, e-learning is changing its function from that of a supplementary tool for conventional group training to that of a major training tool.

On the other hand, there are several technical challenges that must be resolved before e-learning can truly work as an educational/training tool. One is to address the information leaks in differentiation technologies (i.e., the technologies making the company stand out from others) through education concerning its products and technical details, as provided by KCM. The current system takes this into account in its mechanism; however, further modification will be required to expand the system on a global scale. It is also important to make the learning materials and contents compatible with the language of each overseas area, as well as to further expand the contents to meet local needs. KCM currently uses learning materials in three different languages: English, Chinese and Japanese. However, for grooming novice engineers in developing nations, the company recognizes an increasing

need to provide learning materials in their mother languages. The strengthening of the translation system will remain a technical challenge in the future providing of technical information globally. It may also be necessary to enrich the method of conveying technology and spirit by nonlinguistic measures such as games.

Finally, in establishing e-learning as the major training tool, the most important issues include strengthening conformity and cooperation with corporate schemes for developing human resources and the policies governing personnel affairs. Conventionally, it has been difficult to quantitatively confirm and evaluate the effect of education policy and the developing of human resources, which has mostly been evaluated only qualitatively. However, with the recent prevalence of IT and the improvement in its performance, as represented by smart devices, the time is coming when information on the training of human resources can be tied together with information on job performance to

allow the comprehensive processing and use of such information. Hence, for the developing of human resources at overseas branches in the future, e-learning will be conducted in close cooperation with the corporate scheme for developing human resources and the policies governing personnel. Thus e-learning is expected to evolve into an educational tool that is more effective and more directly linked with job performance than ever.

## **Conclusions**

In order to establish a global after-sales service system, KCM has introduced and is expanding e-learning as a tool for universal education. KCM will strive to adapt its knowledge and methodology to the after-sales services of other group companies engaged in the machinery business, so that customers all over the world will be satisfied with the performance of KOBELCO group products and with the service they receive after purchasing.

# Evaluation System for Thin-Film Oxide Semiconductor Using $\mu$ -PCD - Effectivity of Measuring Technique -

Yuki NONOMURA\*<sup>1</sup>, Keizo YAMASHITA\*<sup>1</sup>, Futoshi OJIMA\*<sup>1</sup>, Dr. Tomoya KISHI\*<sup>1</sup>, Kazumasa TOKUDA\*<sup>1</sup>, Dr. Toshihiro KUGIMIYA\*<sup>2</sup>

\*<sup>1</sup> Kobelco Research Institute, Inc.

\*<sup>2</sup> Electronics Research Laboratory, Technical Development Group

*A novel system has been developed for evaluating thin-film oxide semiconductors using a  $\mu$ -PCD (Microwave Photo Conductivity Decay) method. Variations of the mobility and  $V_{th}$  shift are issues in the manufacturing process of oxide semiconductors. To resolve these issues, an evaluation technique has been established. In addition, the mura (unevenness) of film quality on substrate has become another issue as the substrate size increases. It has been demonstrated that mapping measurement is effective in resolving this issue.*

## Introduction

With the prevalence of smartphones and tablets, flat panel displays (FPD) are required to have higher definition, increased display frequency and lower power consumption. Thin-film transistors (TFTs) using oxide semiconductors, as typified by In-Ga-Zn-O (IGZO)<sup>1</sup>, have mobilities higher than those of conventionally used amorphous Si (a-Si), making higher definition possible. Additionally, the FPD manufacturing lines for IGZO also allow lines for a-Si to be used with almost no alteration. Therefore, there are an increasing number of compact panels using oxide semiconductors. Their demand for such panels for large-sized television sets is also expected to increase in the future.

However, there still are issues: i.e., nonuniformity of the field-effect mobility (mobility) of TFTs in a whole substrate caused by film quality, and threshold voltage ( $V_{th}$ ) shift after stress test including light negative bias and temperature stress (LNBTs). For these issues, an in-line evaluation is more important.<sup>2</sup> In recent years, the substrate sizes have been increasing rapidly to improve the yield. This has raised the issue of *mura* in the film quality within each substrate.

Kobelco Research Institute, Inc. has established a technique using the microwave photo conductivity decay ( $\mu$ -PCD) method for evaluating the defect states of Si wafers and the film quality of low-temperature poly silicon (LTPS).<sup>3</sup> This technique was adapted in developing a new system for evaluating the film quality of oxide semiconductor thin films. This system has enabled the evaluation of the deterioration of mobility and  $V_{th}$  shift of oxide

semiconductors. In addition, it was found that mapping measurement allows the evaluation of *mura* in the film quality within substrates.

This paper reports the results of evaluation of the mobility and  $V_{th}$  shift of an oxide semiconductor TFT using the  $\mu$ -PCD method.

## 1. Outline of systems for evaluating oxide semiconductor thin film

**Fig. 1** shows an example of the systems developed: the  $\mu$ -PCD measurement system (LTA-2850SPHIIB) for generation-8.5 LCD (G8.5: substrate size, 2,200 × 2,500mm). This system has a depth of 5,880mm, width of 2,860mm and height of 2,550mm. The current lineup covers the range from research and development application (substrate size : 200 × 200mm) to the G8.5 substrate size.

With the substrate size increased, if the conventional system is used, the measurement time will increase. Therefore, the systems for G5.5 or larger sizes use a dual-head method involving two measurement heads. **Fig. 2** shows the configurations of a conventional single head and newly designed dual head. In each configuration, the stage moves in the X-axis direction, while the head is/head is moving in the Y-axis direction. The dual-head configuration halves the amount of movement in the Y-axis direction, shortening the measurement time for a G8.5 substrate, from the approximate 40 minutes it used to take, to 20 minutes or less.



**Fig. 1** Evaluation system for oxide semiconductor thin films (LTA-2850SPHIIB: substrate size G8.5)

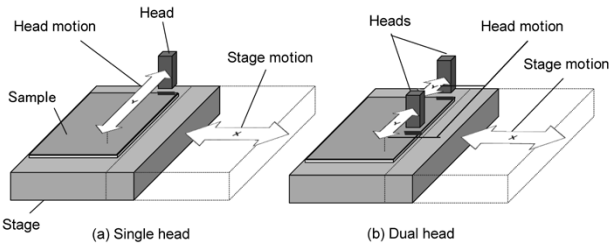


Fig. 2 Configurations of conventional single head and new dual head

## 2. Measurement principle of $\mu$ -PCD

When an oxide semiconductor thin film is irradiated with laser energy exceeding the energy bandgap, electron-hole pairs are generated and excess carriers are produced. These excess carriers are annihilated by recombination, and the time it takes to annihilate them (lifetime) depends on the physical properties of the samples. The excess carriers generated by laser irradiation increase the conductivity of the sample, changing the microwave reflectivity (Fig. 3). The  $\mu$ -PCD is a method of measuring lifetime from the temporal change in the microwave reflectivity.

When evaluating Si bulks and wafers, sufficiently strong signals can be obtained. For thin films, however, the signals are weak. Hence, a differential  $\mu$ -PCD method is used for the microwave detection unit of the oxide semiconductor thin-film evaluation system. This enables an S/N ratio 500 times greater than that achieved by the conventional detection method.<sup>3)</sup>

Fig. 4 depicts the measurement principle of a detection unit with the differential  $\mu$ -PCD method. The oscillated microwave is split into a signal

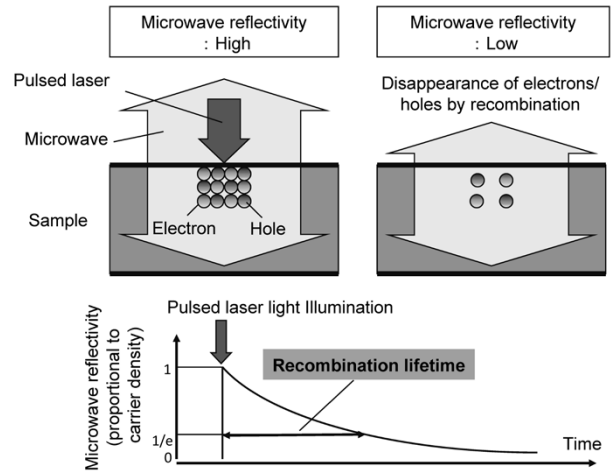


Fig. 3 Measurement principle of  $\mu$ -PCD method

waveguide and a reference waveguide. The carriers in the sample area under the signal waveguide are excited by the laser. Then the detection unit measures the reflectance change caused by excess carriers. The signal from the signal waveguide ("A" in the figure) contains a noise component in addition to the signal of the reflectivity change caused by excess carriers. On the other hand, the signal from the reference waveguide ("B" in the figure) consists only of the noise component. The difference between these two signals ("A - B" in the figure) is calculated to cancel the noise component, which enables signals to be detected with a high degree of sensitivity.

## 3. Method for evaluating oxide semiconductor thin film using $\mu$ -PCD

Fig. 5 illustrates a decay curve for the microwave reflectance of an oxide semiconductor. In an oxide

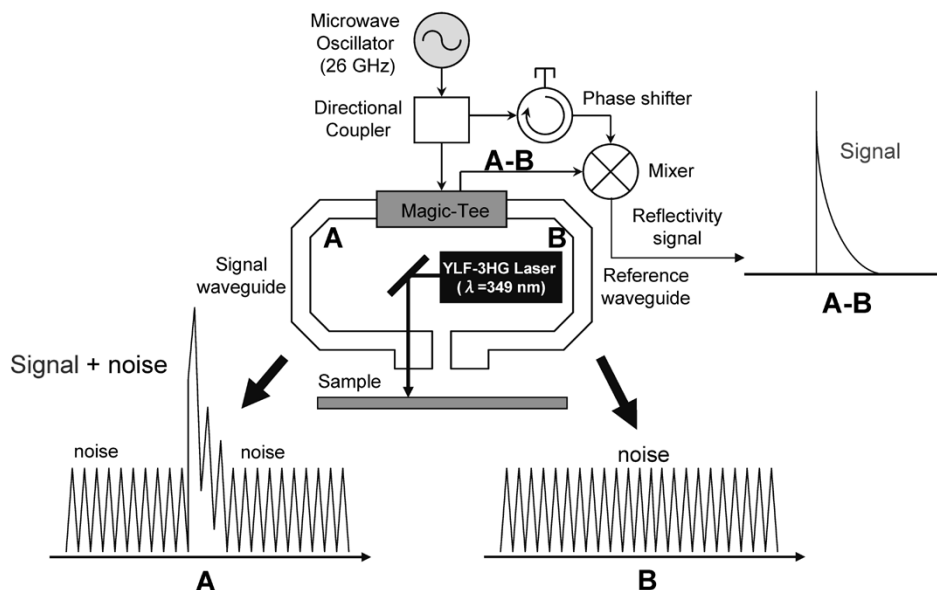


Fig. 4 Principle of differential  $\mu$ -PCD for oxide semiconductor evaluation system (A: signal + noise wave, B: noise wave)



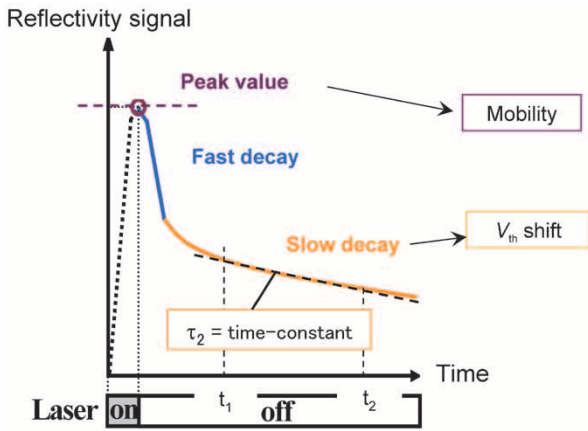


Fig. 5 Decay curve of microwave reflectance for oxide semiconductors

semiconductor thin film, the decay does not occur in accordance with a simple exponential behavior as predicted by Shockley-Read-Hall (SRH) theory<sup>4)</sup> of recombination via trapping. Rather, a gradual decay occurs half way. In other words, the decay consists of two components: namely, a fast decay component and a slow decay component with tailing. The slow decay component can be formulated in several ways. In this paper, for ease of understanding, it is expressed by the linear combination of exponential functions as shown below:

$$n = n_1 \exp\left(-\frac{t}{\tau_1}\right) + n_2 \exp\left(-\frac{t}{\tau_2}\right) \dots\dots\dots (1)$$

where  $n_1$  and  $n_2$  are the carrier densities for the fast decay and slow decay after laser irradiation, respectively, and  $\tau_1$  and  $\tau_2$  are the time constants for the fast decay and slow decay, respectively.

The fast decay is attributable to the deep localized states in an oxide semiconductor thin film, and these localized states affect the mobility of the TFT.<sup>5)</sup> The slow decay, on the other hand, is attributable to the shallow localized states in an oxide semiconductor thin film, and these states are known to affect the  $V_{th}$  shift of TFTs.<sup>6)</sup>

However, the lifetime of the fast decay is extremely short, as in the case of LTPS, making its direct observation difficult. When the pulse width of the pump laser is sufficient with respect to the lifetime, the peak value becomes proportional to the lifetime.<sup>3)</sup> Therefore, for the evaluation of mobility, rather than using the lifetime value of the fast decay, the present system uses the peak value, which can be easily and accurately measured.

Fig. 6 shows the relationship between the field-effect mobility of a TFT and the peak values measured by  $\mu$ -PCD. The mobility represents the saturation mobility calculated from the values of switching characteristics ( $I_d$ - $V_g$  characteristics) measured for the TFT. The measurement was

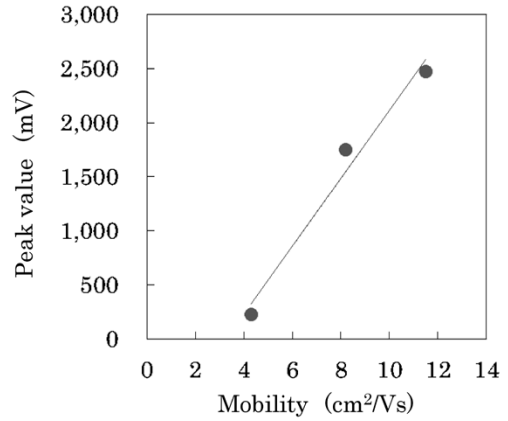


Fig. 6 Relationship between field-effect mobility of TFT and peak value measured by  $\mu$ -PCD

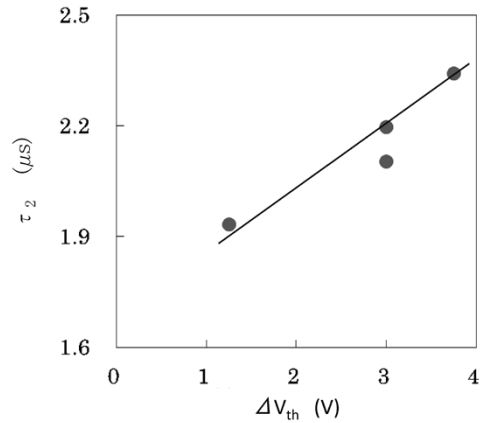


Fig. 7 Relationship between  $V_{th}$  shift of TFT under LNBTS and  $\tau_2$  measured by  $\mu$ -PCD

performed for a gate voltage ( $V_g$ ) of -30 to 30V and a drain voltage ( $V_d$ ) of 10V. There is a proportional relationship and correlation between the mobility and peak values.<sup>7)</sup>

Fig. 7 shows the relationship between  $V_{th}$  shift of a TFT under the LNBTS and  $\tau_2$  measured by  $\mu$ -PCD. The conditions of the LNBTS include  $V_g = -20V$ ,  $V_d = 10V$ , a substrate temperature of 60°C, light source of white LED (strength 25,000 Nit) and stress applied for 2 hours. Again, there is a proportional relationship and correlation between the  $V_{th}$  shift and  $\tau_2$ .

As described above, the use of the two parameters (peak value and  $\tau_2$ ) is found to enable the evaluation of the mobility and  $V_{th}$  shift of LNBTS in oxide semiconductor thin films before the fabrication of TFTs.

#### 4. Effectivity of mapping measurement

With increasing substrate size, one of the problems encountered in mass production lines is the *mura* of film quality in a whole substrate. Mapping measurement is effective because the *mura*

can be easily evaluated in a whole substrate.

As shown in Fig. 8, a glass substrate was placed right above a target material. After the film deposition, the peak value was measured in a whole substrate. Here, two types of target materials were used to confirm the difference: namely, a divided target and a non-divided target without seam. The results are shown in Fig. 9. Both the maps show a tendency for the circumferential portions to be lower. The divided target, (a) in the figure, shows lower peak values in the portions corresponding to the joints of the target. This tendency is particularly noticeable in the central portion, where the peak value is approximately 300mV lower than that of the same portion of the non-divided target, (b) in the figure. For this portion, the saturation mobility was calculated from the  $I_d$ - $V_g$  characteristics of the TFT (Fig.10). The results indicate that the divided target with lower peak values also has a mobility lower than that of the non-divided target.

The sputtering targets of  $Ga_2O_3$ ,  $In_2O_3$  and ZnO were placed as shown in Fig.11 to perform co-sputtering of multi-elements. Using this arrangement, an experiment was conducted to evaluate the difference in film quality due to the composition of the oxide semiconductor thin film. The peak values obtained by the mapping measurement and the mobilities measured for the TFT are shown in the figure. There are agreements between the high and low portions of the peak value and mobility, indicating strong correlations.<sup>5)</sup> Thus, the peak value mapping permits convenient checking of the *mura* in transistor characteristics (mobility).

Fig.12 shows an example of the peak value mapping of an oxide semiconductor thin film (substrate size: 370×470mm) before and after annealing. The mean peak value changes before and after annealing. This indicates that film quality is changed by annealing. Regarding film quality distribution, both of the results show a tendency for

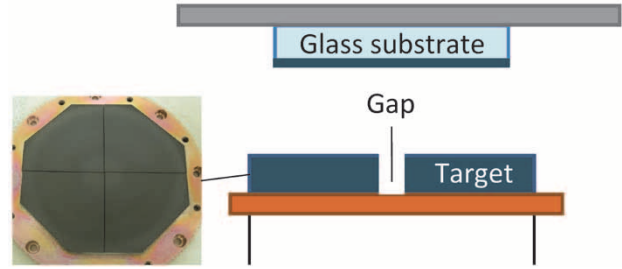


Fig. 8 Arrangement of target and glass substrate

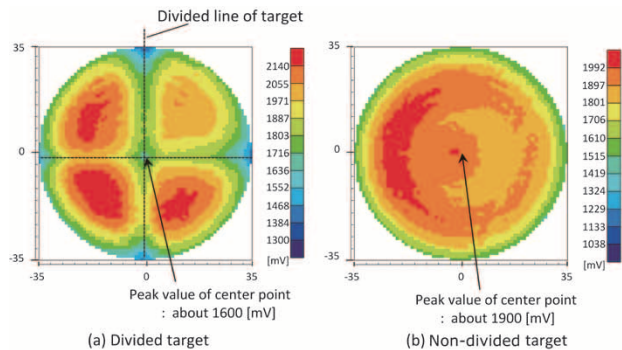


Fig. 9 Peak value mapping measured by  $\mu$ -PCD (a) divided target, (b) non-divided target

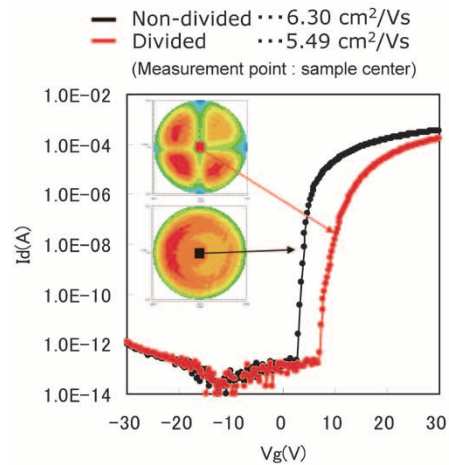


Fig.10  $I_d$ - $V_g$  characteristic of samples deposited using divided and non-divided target

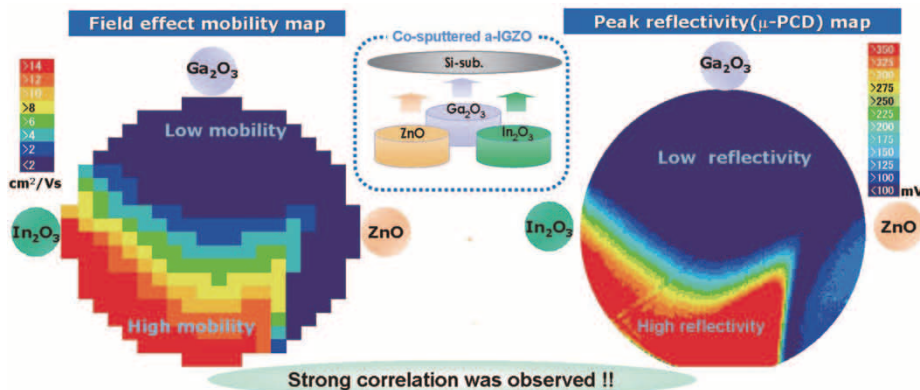


Fig.11 Relationship between field-effect mobility and peak value using  $\mu$ -PCD

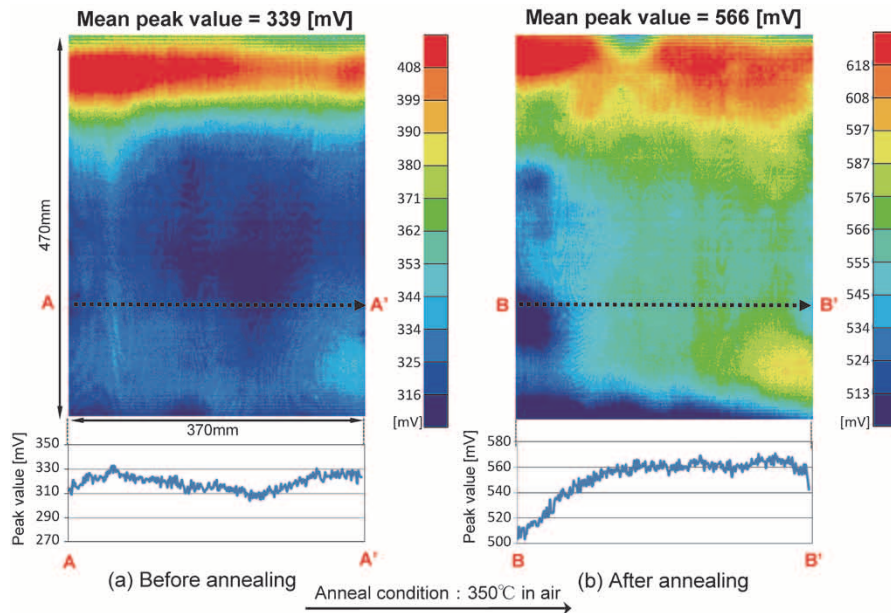


Fig.12 Peak value mapping for IGZO film before and after annealing

the upper portion of the sample to exhibit higher values; however, they show different distributions as indicated in the left lower portion. The values along A-A' and B-B' are plotted in the corresponding graphs below the maps. For both of the graphs, one division represents 20mV. These graphs for before and after annealing are compared; the comparison shows an improvement of *mura* in film quality in the center-to-right region; however, there is a precipitous decrease in the peak value on the left side. As shown, peak value mapping allows a convenient evaluation of *mura* in film quality in a whole substrate of the sample; and mapping measurement is effective in process optimization and anomaly detection when adapted for in-line evaluation.

## Conclusions

This paper has introduced a technique for evaluating oxide semiconductor thin films and described the effectivity of mapping. The use of the present system enables the evaluation of the mobility and  $V_{th}$  shift of oxide semiconductor thin films before the fabrication of TFTs. In addition, the system allows mapping measurement in a non-contact, non-destructive manner, permitting

the evaluation of *mura* in film quality within each substrate. These advantages of the system can be exploited in optimizing the process conditions for manufacturing oxide-semiconductor TFTs and in improving the yield of mass production lines. The future plan includes obtaining the results for mapping measurements of peak values and  $\tau_2$ , and acquiring the correlation data with TFT characteristics from films deposited under various conditions: for example, oxygen concentrations and annealing temperatures during the film deposition.

Finally Kobelco Research Institute, Inc. will strive to exploit these techniques for the present system so as to contribute to the development of the FPD market.

## References

- 1) K. Nomura et al. *Nature*. 2004, Vol.488, p.432.
- 2) Y. Nonomura. *Cobernics*. 2014, Vol.23, No.41, p.10.
- 3) S. Sumie et al. *R&D Kobe Steel Engineering Report*. 2007, Vol.57, No.1, p.8.
- 4) N. Matsuo. *Semiconductor device - based on operating principle -* Corona Publishing, 2000, p.76.
- 5) S. Yasuno et al. *Appl. Phys. Lett.* Vol.98. 2011, No.102107, p.2.
- 6) H. Goto et al. *IEICE. TRANS. ELECTRON.* 2014, Vol.E97-C, p.1055.
- 7) S. Yasuno et al. *IEICE TRANS. ELECTRON.* 2012, Vol. E95-C, No.11, p.1724.